2019

A Hybrid-Powered Wireless System for Multiple Biopotential Monitoring

Shawn Li
Michigan Technological University, xian@mtu.edu

A HYBRID-POWERED WIRELESS SYSTEM FOR MULTIPLE BIOPOTENTIAL MONITORING

By

Xian Li

A DISSERTATION

Submitted in partial fulfillment of the requirements for the degree of

DOCTOR OF PHILOSOPHY

In Mechanical Engineering-Engineering Mechanics

MICHIGAN TECHNOLOGICAL UNIVERSITY

2019

This dissertation has been approved in partial fulfillment of the requirements for the Degree of DOCTOR OF PHILOSOPHY in Mechanical Engineering-Engineering Mechanics.

Department of Mechanical Engineering-Engineering Mechanics

Dissertation Advisor: *Dr. Ye Sun*

Committee Member: *Dr. Bo Chen*

Committee Member: *Dr. Zhen Liu*

Committee Member: *Dr. Mo Rastgaar*

Department Chair: *Dr. William W. Predebon*

Contents

List of Figures

List of Tables

Preface

This dissertation is original, published, independent work by the author, Xian Li.

Acknowledgments

I would like to express my deepest gratitude to my advisor, Dr. Ye (Sarah) Sun, for her understanding, guidance, and support during my Ph.D. study at Michigan Technological University. It is my honor to be her *first* Ph.D. student. She gives me an opportunity to learn from her and provides me with inspiration and financial support to complete this study. I also extend my great appreciation to Dr. Bo Chen, Dr. Zhen Liu, and Dr. Mo Rastgaar for serving on my committee and reviewing my work.

I would like to acknowledge suggestions and help from the faculty, staff, and students in Department of Mechanical Engineering-Engineering Mechanics, especially thanks to Dr. James DeClerck, Dr. Charles D. Van Karsen, and Dr. Aneet Narendranath.

Thanks to all my friends, Hui Huang, Si Liu, John Hoffman, Wenping Deng, Ran Duan, Judy, Jinzhao Xiang, Zhihong Wang, Jinsen Chen, Emma Liu, Lin Liu, Chenlong Zhang, Lijun Liu, Zhuo Xu, Lewis, Chandan, Abhisek, Upendra, Sharath, Suki Li, Zhongtian Zhang, Ying Wen, and He Meng, especially thanks to Robert G. Nuranen and Ronald G. Gedda for their encouragement and help.

Finally, I sincerely appreciate my parents and all they have done for me, endless love, strong support, and great encouragement.

List of Abbreviations

AC	Alternative current
AFE	Analog front end
BCG	Ballistocardiography
BLE	Bluetooth low energy
CVD	Cardiovascular disease
CR	Compression rate
DC	Direct current
ECG	Electrocardiogram
EEG	Electroencephalogram
EMD	Empirical mode decomposition
EMG	Electromyography
EOG	Electrooculography
ETI	Electrode-tissue impedance
HPF	High pass filter
IMF	Intrinsic mode function
IOT	Internet-of-Things
JFT	Joint frequency time
LED	Light-emitting diode

LPF	Low pass filter
ORP	Out of range percentage
ORT	Out of range time
PE	Polyethylene
PMIC	Power management integrated circuit
RC	Resistor and capacitor
RMSE	Root mean square error
RT	Recovering Time
SC	Stratum corneum
SNR	Signal to noise ratio
SSHI	Synchronized switching harvesting on inductor
TEH	Triboelectric energy harvester
TENG	Triboelectric nanogenerator

Abstract

Chronic diseases are the top cause of human death in the United States and worldwide. A huge amount of healthcare costs is spent on chronic diseases every year. The high medical cost on these chronic diseases facilitates the transformation from in-hospital to out-of-hospital healthcare. The out-of-hospital scenarios require comfortability and mobility along with quality healthcare. Wearable electronics for well-being management provide good solutions for out-of-hospital healthcare. Long-term health monitoring is a practical and effective way in healthcare to prevent and diagnose chronic diseases. Wearable devices for long-term biopotential monitoring are impressive trends for out-of-hospital health monitoring. The biopotential signals in long-term monitoring provide essential information for various human physiological conditions and are usually used for chronic diseases diagnosis.

This study aims to develop a hybrid-powered wireless wearable system for long-term monitoring of multiple biopotentials. For the biopotential monitoring, the non-contact electrodes are deployed in the wireless wearable system to provide high-level comfortability and flexibility for daily use. For providing the hybrid power, an alternative mechanism to harvest human motion energy, triboelectric energy harvesting, has been applied along with the battery to supply energy for long-term monitoring.

For power management, an SSHI rectifying strategy associated with triboelectric energy harvester design has been proposed to provide a new perspective on designing TEHs by considering their capacitance concurrently. Multiple biopotentials, including ECG, EMG, and EEG, have been monitored to validate the performance of the wireless wearable system. With the investigations and studies in this project, the wearable system for biopotential monitoring will be more practical and can be applied in the real-life scenarios to increase the economic benefits for the health-related wearable devices.

Chapter 1

Introduction

1.1 Motivation and Objective

Cardiovascular disease (CVD) is the primary cause of human death in worldwide [1][2]. World Health Organization (WHO) estimates that 32% of all global deaths, which is estimated to be 17.9 million, were due to CVD in 2015 [1]. Data from the American Heart Association (AHA) indicates that by 2035, over 130 million adults in the US population (45.1%) are projected to have some form of CVD [2]. CVD is a class of diseases that involve the heart or blood vessels [3], including heart diseases and strokes. Statistics indicate that an estimated 7.4 million people died from coronary heart disease and 6.7 million died from a stroke in 2015 [1]. Especially, in the United

States, heart disease is the principal cause of deaths and responsible for over 23% of the total deaths in 2015 [4]. A huge amount of healthcare costs is spent on CVD every year. The total direct and indirect costs of cardiovascular diseases in 2010 were estimated to be $315.4 billion [5]. Among the total costs, the biggest portion ($98.0 billion) was directly used for in-hospital inpatient stays, which is much higher than the cost of direct out-patient healthcare ($32.8 billion). The high medical cost of prolonged in-hospital healthcare on the CVD facilitates the transformation from in-hospital to out-of-hospital healthcare.

The out-of-hospital scenarios require comfortability and mobility along with quality healthcare. Wearable electronics for well-being management meet these requirements and provide good solutions for out-of-hospital healthcare [6]. Moreover, as recommended by WHO [1], the prevention and early controls of CVD can prolong patients living possibility and improve life quality. Therefore, long-term health monitoring is a practical and effective way to prevent and diagnose CVD.

Wearable devices for long-term biopotential monitoring are impressive trends for out-of-hospital health monitoring. The biopotential signals in long-term monitoring will provide essential information for various human physiological conditions and are usually used for CVD diagnosis. The most common biopotential signals include electrocardiogram (ECG), electromyography (EMG), and electroencephalogram (EEG). ECG is a good indicator of heart diseases, as well as EMG for muscle relevant diseases

and EEG for brain relevant disorders.

For long-term monitoring, the long lifetime of the medical devices with lightweight and autonomic energy is highly desired [7]. Due to its function of human monitoring in daily use, safety and functional stability are always necessary for wearable electronics. High energy density and power capacity are favorable characteristics of energy resources for wearable electronics, enabling a longer lifetime of the power supply. In addition, flexibility and wearability are also highly desired for wearable electronics with the consideration of lightweight, small size, and flexible substrates.

In order to ensure the comfortability of patients and enhance the flexibility of usage scenarios, the electrodes of wearable systems for long-term biopotential monitoring need to be earnestly considered. The traditional electrodes that most widely used in the hospital are wet contact electrodes, which require physical contact with the skin via conductive gel (i.e. Ag/AgCl gel). Another type of electrodes, dry contact electrodes, can detect the biopotential signals without conductive gel but by directly contacting with the human skin. The long-time contact of the skin with the gel or the electrodes will possibly cause potential skin allergy and irritation, which cause that wet/dry contact electrodes are not suitable for adopting in the long-term biopotential monitoring. A new type of electrodes needs to be designed for use in long-term biopotential monitoring without causing problems induced by long-time contact.

Due to the limitation of the battery size and the power storage, the battery-powered

wearable electronics come with the power source challenges for long-term monitoring. New technologies such as energy harvesting have the capability to effectively power electronic instruments [8]. For energy harvesting, human motion is one of the most significant energy resources that can be harvested to power wearable electronics, enabling self-sustainability [9][10]. Three mechanisms are commonly adopted to convert this mechanical energy to electricity: piezoelectricity based on piezo materials [11], electromagnetics based on Lenzs Law [12], and electrostatics based on variable capacitance [13]. However, scavenging motion is still challenging due to its nature of random and low frequency (<5 Hz) [14]. New designs based on new mechanism are needed to meet the requirements for harvesting energy from human motions. In our preliminary study, triboelectric energy harvesters (TEHs) based on Triboelectricity have potentials to scavenge μW level power from human motion (e.g. hand clapping and sliding movements). Though this amount of power is not enough for the self-powered wireless system, it is suitable for a more practical power supply, the hybrid power, of the long-term wireless wearable system.

Energy efficiency of the wireless system is critical for long-term monitoring. Due to the limited power supply, energy efficiency imposes a stringent constraint in the wireless systems, where long life is highly demanded in long-term biopotential monitoring. In order to maintain a long lifetime, the system needs to obtain high energy efficiency, which can be achieved by two methods. The first way is increasing the harvested energy from the energy source, which, in this case, requires a power management

strategy of triboelectric energy harvesting. The second method to increase the energy efficiency of the system is lowering the power consumption. The most significant power consumption of a wireless system usually happens on wireless transmission. Therefore, strategies are required to develop to lower the power consumption on wireless transmission.

The main goal of this project is to build a hybrid-powered wireless wearable system for long-term monitoring of multiple biopotential signals. To develop such a system, the main challenges include designing the electrodes suitable for long-term monitoring; building the system prototype for biopotential monitoring; developing an energy harvester to continuously power the system; proposing a power management strategy for the energy harvester and optimizing the power consumption of the system. In order to address these key challenges, the research of this project is performed in four major aspects. 1) Design and validate the non-contact electrodes for long-term biopotential monitoring; 2) Developing the TEH for harvesting energy from human motion; 3) Proposing an SSHI rectifying strategy to enhance the power efficiency for TEHs; 4) Building the wireless wearable system for monitoring multiple biopotentials with considering optimizing the power consumption on wireless transmission.

1.2 Background

Biopotentials are produced as a result of electrochemical activities occurring within the body by a certain type of cells that are known as excitable cells [15]. Excitable cells can be found in the nervous, muscular and glandular systems in the body. During the physiological processes in the body, an excitable cell is stimulated and it generates an action potential, which is the essential source of biopotentials. Different biopotentials come from individual bioelectric sources. The typical biopotentials of the human body, such as electrocardiogram (ECG), electromyogram (EMG), and electroencephalogram (EEG), correspond to the cardiac muscle, skeletal muscle, and the brain, respectively. These three typical biopotentials are most commonly used as diagnostic information in both in-hospital and out-hospital scenarios. The biopotentials in long-term monitoring will provide essential information for various human physiological conditions and are usually used for CVD diagnosis.

The biopotentials can be recorded by conducting the electrodes on the body. Different from the needle-like electrodes that need to be inserted in the muscle, the electrodes that placed on the surface of the skin are convenient to attach without physical damage to the skin and muscle. The convenience makes the surface electrodes popular in biopotential monitoring. Different surface electrodes have been developed to detect biopotentials. The electrodes that most widely used in the hospital are wet contact

electrodes, which are also known as the standard electrodes because of the popularity. The wet contact electrodes require physical contact with the skin via conductive gel (e.g. Ag/AgCl gel, which is the most common type). Another type of electrodes, known as dry contact electrodes, is designed to detect biopotential signals without explicit electrolytes. Both wet and dry contact electrodes require the physical contacting with the skin. One of the disadvantages of using wet or dry contact electrodes is that they can be used only on the normal healthy skins. For those extremely sensitive skins, for example, burn skins, neither wet nor dry contact electrodes are the proper choices. In this perspective, a new type of electrodes, non-contact electrodes, is designed for use without directly contacting the human skin.

The typical surface biopotentials detected by the surface electrodes are usually at low voltages (e.g. 1 mV or less). Such low voltages need specific analog circuits to amplify then can be detected by the monitoring devices. The biopotential monitoring devices can be as big as those medical-care types that are of equipment that placed aside of the patients' therapeutic beds, or as small as the wearable devices that patients carry with them on the body. The former lacks the convenience and mobility, which may be the critical features required for long-term monitoring. As mentioned in Section 1.1, wearable devices for long-term biopotential monitoring are impressive trends for out-of-hospital health monitoring. As a more advanced type, wireless wearable devices for biopotential monitoring offer higher-level flexibility and wearability for daily use.

Nowadays, more portable electronics are commonly used in our daily life than ever. From the mobile phones to smartwatches, the need for mobile electrical power resources is increasing. The power sources for operating these portable devices are typically built-in batteries. Due to the limitation of the size and charge density of the batteries, the power demand of recharging is growing. Energy harvesting provides rechargeable power sources for portable devices and expands their lifetimes. Different types of energy harvesting techniques based the renewable energy, including solar, thermal, photostatic, bioenergy, hydro, tidal, wind, wave, and geothermal, have been developed for decades [16].

Human motion, as a biomechanical-energy resource, has been a standout that opens the way for the development of energy harvesting technologies for wearable devices. The idea of harvesting energy from human motion is based on the fact that an average person's energy expenditure, which is the amount of energy used by the body, is 1.07×10^7 J per day [17]. This energy amount is equivalent to approximately 2000 Ah in batteries. The mechanical efficiency of the human body is estimated to approximate 15 - 30 % [18]. Human motion happens naturally in our daily life. It provides a considerable amount of energy to power wearable electronics without introducing any extra load.

The major energy sources of human motion come from the upper and lower limbs movements. The potential energy sources of human motion are heel strikes, shoulder

and elbow joint motion during arm swings, and leg motions, i.e., ankle, knee, and hip motions [17]. In this study, due to the physical structure of the energy harvesters, we focus on the hand's motion during hand-clapping and the heel strikes during walking.

In current literature, human motions can be generally harvested by harvesters that convert the mechanical energy into electricity, including TEHs we built in this study. TEHs also namely triboelectric nanogenerators (TENGs) have been studied extensively in recent years since firstly introduced in 2012 [19]. The energy conversion in TEHs is based on the mechanism of triboelectricity or contact electricity by which surface charge is generated from contact and separation or sliding between two materials. The generated charge fluctuates periodically with the input vibration, which thus can convert mechanical energy to electrical energy. For triboelectric charge generation, material and contact have been identified as the two major contributing factors. Significant efforts have been put on enhancing material and contact of TEHs for improving power generation and efficiency.

A typical TEH or TENG consists of three major components: two triboelectric material layers for charge generation, two electrode layers, and a substrate for motion conversion. Most materials can act as triboelectric materials as the triboelectric series [20]. Sometimes, for a simplified TEH, one conductive material can be used as both triboelectric material and electrode. In the working process of TENGs, the periodic relative motion between the two triboelectric material layers results in the generation

and distribution of electrical charges. The two common modes of triboelectric energy harvesting are related to the two different motions: contact-separation and sliding [21].

Applying TEHs to harvest energy from human motions have, at least, the following advantages. TEHs don't require to work on the high-frequency range, which makes TEHs suitable for scavenging energy human motions that are usually at low-frequency (< 5 Hz); TEHs can fit for human motions' nature of irregularity; TEHs can have a high voltage output that required for powering wearable electronics.

The background in this chapter has introduced empirical foundations of this dissertation, including the biopotentials, electrodes, wearable devices, energy harvesting, human motions, and TEHs. The detailed literature review will be represented in Chapter 2.

1.3 Organization of Dissertation

This dissertation has developed a hybrid-powered wireless wearable system for long-term biopotential monitoring. A triboelectric energy harvester has been designed to harvest energy from the human motion, including hand-clapping and walking, to partially power the wearable system. An SSHI interface was developed for the

first time to increase the power efficiency of triboelectric energy harvesting at the ac-dc stage. The harvested energy was stored and managed with the battery power by the power management module, to prolong the lifetime of the wearable system. The energy consumption was decreased by introducing the signal compression into the signal transmission. The triboelectricity-induced motion artifacts have been also studied in this project.

This dissertation is organized as follows: Chapter 1 provides a general introduction to this study. Chapter 2 reviews the state-of-the-art researches and techniques related to this study, including the electrodes for biopotential monitoring, human motion energy harvesting, power management for triboelectric energy harvesters, and the wireless wearable systems for biopotential monitoring. Chapter 3 describes our design of the wireless biopotential monitoring system in terms of the active non-contact electrodes, critical analog-front-end circuit, implementation, and performance validation. Chapter 4 presents the design and validation of triboelectric energy harvester. The human motion energy harvesting from the hand-clapping and walking has also been validated in this chapter. Chapter 5 illustrates the power management, mainly our proposed SSHI interface for improving energy efficiency for TEHs. A new theoretical model is developed for electricity generation from triboelectric energy harvesting considering the introduced pairing capacitance and the impact force in practical condition. An SSHI rectifying strategy associated with TEH design has been reported and it provides a new perspective of designing TEHs or TENGs by considering their capacitance

concurrently. Chapter 6 presents the validation experiments that show the capability of the proposed wearable system to detect multiple biopotentials including ECG, EMG, and EEG, and the stability in long-term monitoring. The power optimization with a data compression technique has also been introduced. Chapter 7 concludes the dissertation and provides recommendations for future work.

Chapter 2

Literature Review

This project involves four major tasks to achieve the wearable system for biopotential monitoring, including 1) reviewing the up-to-date electrodes built for biopotential monitoring; 2) surveying the energy harvesting techniques, especially triboelectric energy harvesting, for harvesting power from human motion; 3) introducing the present power management strategies, i.e. rectifying methods, for triboelectric energy harvesters; 4) reviewing the latest wireless wearable systems developed in recent 5 years for biopotential monitoring.

In this chapter, the state-of-the-art of the filed is extensively reviewed for these four tasks. Especially, this chapter includes: 1) electrodes for biopotential monitoring; 2) human motion energy harvesting; 3) power management for triboelectric energy

harvesters; 4) wireless wearable systems for biopotential monitoring. Based on the literature review, we will summarize and list our contribution comparing to the state-of-the-art in the final section.

2.1 Electrodes for Biopotential Monitoring

The biopotential signal is one of the most important indicators for health conditions. Biopotential monitoring is a powerful tool for chronic diseases diagnosis. For biopotential monitoring, the electrodes are generally wet or dry contact which requires physical contact with the skin with or without conductive gel (for example, Ag/AgCl gel). Wet contact electrodes, known as the standard electrodes, are the most common type of electrodes used in hospital facilities [22]. It requires some sort of explicit electrolyte to conduct the biopotential signals from human skin to electrodes. Different types of electrolytes have been used as the conductive gel. Ag/AgCl gel is the most common type [22]. Wet contact electrodes are simple, lightweight and disposable, and can provide excellent signals with properly using. These golden features make sure that wet contact electrodes are still the best choice in clinical and research applications. However, due to the conductive gel being adhesive on the human skin through the whole detecting process, wet contact electrodes are not suitable for some specialist domains, e.g. long-term, unsupervised monitoring and patients with extremely sensitive skins (i.e., burn skins, neonatal care) [23]. In these applications, dry contact

and non-contact electrodes offer benefits over wet contact electrodes.

Dry contact electrodes are designed to detect biopotential signals without explicit electrolytes. Instead, they usually operate with the moisture on the skin (i.e. sweat) [23]. Meziane et al. [24] have reviewed the dry electrodes for biomedical use and physiological research, especially, for ECG monitoring. New materials and manufacturing methods have been integrated into developing dry electrodes for long-term biopotential monitoring. Actually, any conductive material, like stainless-steel disc, conductive foam, and conductive fabric, can be built as dry contact electrodes to contact with skins. Le et al. [25] have developed an active dry electrode with a silver-coated plate.

Applying the conductive fabric or textile in the dry electrodes design is a popular trend in the recent researches. Catrysse et al. [26] developed so-called textrodes based on textile sensors for ECG measurement. Choi et al. [27] applied the conductive fabric and PVDF film to develop a belt-type sensor for ECG monitoring. Lin et al. [28] introduced a dry contact electrode based on polymer foam for long-term EEG measurement. Chen et al. [29] have presented a type of dry electrodes made of polymer fabric that offer high use of comfort for ECG and EEG monitoring. They optimized the polymer composition to reduce the skin-electrode impedance to approximately 10 times larger than that of Ag/AgCl gel electrodes. Boehm et al. [30] have developed a 12-lead ECG T-shirt with active electrodes. They have verified the

system performance with the subjects wearing this ECG T-shirt in different scenarios (including lying, sitting, and walking). Their T-shirt design has the advantage of offering high user comfort during detecting 12-lead ECG. Pani et al. [31] have designed dry textile electrodes based on woven fabrics. As claimed by the authors, they present an easy and reproducible fabrication process, very good performance in wet and dry (at rest) conditions and a superior level of comfort with respect to textile electrodes proposed so far. Yokus and Jur [32] have proposed fabric-based dry electrodes for biopotential recording. The multilayer dry electrodes are fabricated by screen printing of Ag/AgCl conductive inks on flexible nonwoven fabrics. Compared to the Ag/AgCl wet electrodes, their dry electrodes feature the flexibility and comfort to provide an inexpensive monitoring platform for biopotential measurements. Das and Park [33] have proposed a dry electrode based on conductive elastomer for biopotential monitoring applications. The experiments indicate that their flexible touch sensor is capable of bringing good quality biopotential signals including ECG and EMG. Guo et al. [34] have developed a flexible and cost-effective dry electrode with low and stable contact impedance. The dry electrode features self-wetting by the aid of moisture on the skin. The electrode has a thickness of 33 μm, which offers high comfort during long-term biopotential monitoring. Xiao et al. [35] have designed the dry electrode for ECG monitoring by using the plain weave and honeycomb weave patterns in the design. Experimental data indicated that more content of conductive filaments and larger connection area of conductive fabric part to human skin would

lead to lower skin-electrode impedance, larger R-peak amplitude, a larger value of signal-to-noise ratio, but poorer comfortability. The authors recommend to find out a balance point between the higher quality of ECG acquisition and wearable comfortability in the design of weave-based dry electrodes. Choi et al. [36] have developed a driver ECG measuring system with a conductive fabric-based dry electrode. The dry electrode is manufactured by an electroplating method with the conductive fabric material. Achilli et al. [37] have developed a dry electrode based on screen-printed textile for ECG monitoring. The ECG signals obtained by the dry electrodes are highly similar to those detected with disposal gelled Ag/AgCl electrodes (confidence $\rho > 0.99$). Golparvar and Yapici [38] have built an active dry contact electrode for EOG acquisition based on graphene-coated electroconductive textile. The detected EOG signals show a correlation of up to 87% with the simultaneously recorded signal by the pre-gelled, wet, Ag/AgCl electrodes.

Another popular trend for designing the dry electrodes is utilizing the micro-needle array, especially for EEG minoring. Huang et al. [39] have proposed an active comb-shaped dry electrode to effectively acquire EEG in hairy site on the subject's head. Different from MEMS-based dry electrodes, their active dry electrode has a simple structure and manufacture procedure which make it suitable for mass-production. Pei et al. [40] have developed a dry electrode with the microneedle design which is insensitive to the skin-potential variation during ECG monitoring. Wang et al. [41] have also designed a dry electrode with the microneedle array on a flexible substrate.

They have tested the performance of the dry electrode in long-term EEG monitoring (3 hours). Zhou et al. [42] have designed an ear-EEG acquisition system with dry-contact active electrodes. High CMRR (over 100 dB@DC) has been obtained in the experiments with active electrodes. New technologies, like 3D printing, are also applied to develop the dry contact electrodes. Salvo et al. [43] have designed and fabricated a 3D printed dry electrodes for ECG/EEG recording. The 3D printed structures are in 10 μm levels. Wolterink et al. [44] have developed a soft and flexible 3D-printed dry electrode for surface EMG sensing. They claim that there is no significant difference between the printed sEMG electrode and the gold standard Ag/AgCl gel electrodes. Fiedler et al. [45] have investigated the influence of contact pressure, flexibility, and pin number of the dry electrodes with the multipin structure on the electrode-skin impedance during EEG monitoring. These recent proposed that dry electrodes even have comparable signal quality as commercial Ag/AgCl wet electrodes.

The latest electrode type is the non-contact electrode. Different from the wet and dry contact electrodes, non-contact electrodes allow the electrodes attaching outside the cloth without contacting the human skin alternatively. The non-contact feature can reduce skin irritation and increase the comfortability of individuals during long-term monitoring. The first non-contact electrodes were probably first developed in 1994. Clippingdale et al. [46] demonstrated a working non-contact system with ECG array sensors. The signals were acquired with an approximate 3-mm spacing from

the human body. In 2000, Prance et al. [47] improved their non-contact electrodes with an instrumental amplifier design. Harland et al. [48] described detecting ECG signals by their ultra-low-noise, ultra-high-input-impedance probes. In their tests, the electrical activity of the heart can be detected at distances of up to 1 m from the human body. Spinelli et al. [49] have built and tested a capacitive electrode featured with fast recovery in acquiring ECG signals. Fong et al. [50] have developed a fabric electrode with an embedded polymer for non-contact ECG monitoring. The designed hygroscopic sensor has an embedded super-absorbent polymer layer to provide humidity to enhance the capacitive coupling. The strong coupling allows the measurement of a stable, clear biopotential signal. Chen et al. [51] have developed a novel non-contact electrode with adaptive mechanical design for EEG measurements. The experimental results indicate that the non-contact electrode can provide good performance of measuring EEG in a hairy site and a good ability to avoid the influence of motion artifacts. Parente et al. [52] have developed a capacitive sensor for the contact-less detection of ECG signals. They provided the detailed circuit design of the measurement system. The experimental results showed that their system was capable of detecting the heart rate signal at a distance of 0.5 cm from the skin. Vlach et al. [53] have presented the design of an active capacitive electrode for monitoring ECG signals. The proposed capacitive electrode uses a dielectric ceramic layer with high permittivity and a surface area no greater than a few cm^2. The results show 26 dB signal to noise ratio (SNR) for the electrode with a ceramic dielectric layer, which

was put on a skin over a cotton fabric, compared to 13 dB SNR for an electrode with a metal plate with a four times larger surface area.

Various applications have been developed for daily monitoring with non-contact electrodes placed off the body. Lim et al. [54] recorded ECG signals by placing insulated electrodes in the bathtub. The recorded signals have relatively large R peaks for heart rate detection. Kim et al. [55] developed an insulated electrode based on copper plates and PTFE films. The electrodes were placed on the toilet cover. They compared the detected signals with and without electrical ground. Their results showed the heartbeat signals could be detected in both settings. Chair application is one of the most popular applications with non-contact electrodes. The possible reason is that chairs belong to the most common tool which people keep contact within the normal days. Lim et al. [56] presented a method of ECG measurement with non-contact electrodes while subjects sat on a chair wearing normal clothes. Their study showed the feasibility of their method for long-term, convenient, everyday use. Aleksandrowicz and Leonhardt [57] integrated the capacitively coupled electrodes into an office chair to measure ECG through the cloth. The QS complex and the T wave of their detected ECG signals were clearly identified. Baek et al. [58] developed a diagnostic chair for simultaneous ECG, photoplethysmogram (PPG), and ballistorcardiogram (BCG) measurements based on non-contact electrodes. For ECG detection, their electrodes are capacitive coupled electrodes. For PPG monitoring, they used seat-mounted sensors with specially designed amplifier circuits. For BCG measurement, they used a

PVDF film-type transducer which was installed beneath the seat cover. Kim et al. [59] proposed a seat-type non-contact electro-mechanical film sensor to detect the respiratory rate from BCG. Their results showed that the respiratory rate could be measured in real-time on a moving wheelchair. There are also bed applications for non-contact electrodes. Lim et al. [60] developed an array of high-input-impedance non-contact electrodes and put the electrodes on the mattress with a cotton bedcover covered. The detected ECG signals had lower quality and larger motion artifacts than the conventional wet contact electrodes. Bu et al. [61] put the fabric electrodes on the mattress to detect ECG signals through clothes. Non-contact electrodes have also been integrated into wearable applications. Chi et al. ([62], [63], [23], [64]) developed a few versions of active dry or non-contact electrodes for cardiac and neural monitoring. In their study [64], headband for EEG detection and vest for ECG monitoring have been developed based on their non-contact electrodes. Sun & Yu [65] reviewed the capacitive biopotential measurements for ECG/EMG/EEG signal acquisition. Automotive applications are also proposed and studied ([57], [66], [67], [68], [69]).

The state-of-the-art of common dry contact electrodes and the latest electrode type - non-contact electrodes - have been reviewed in this section. The current research direction for designing dry contact electrodes is applying the conductive fabric or textile or utilizing the micro-needle array. In recent years, researchers have put great efforts into designing non-contact electrodes to monitor biopotentials with electrodes

placed off the body. The performance of the non-contact electrodes has been improved to extend the application scenarios.

2.2 Human Motion Energy Harvesting

Energy harvesting and self-powered devices have been studied for a long time and gain the continuous interest of researchers in recent decades. Benefited by the impressive development of sensor network and electronics technologies, environmental autonomous sensor and sensor networks became possible in the near future. Motivated by the practical requirements of self-powered sustainable devices, energy harvesting techniques have much progress.

A number of good literature reviews have been done in the last decades to summarize the development of portable and wearable devices powered by ambient resources. Different reviews focus on different interests, such as power and energy management, various energy resources and system design, and specific energy resources. Wan et al. [70] reviewed sustainable wireless sensor networks from the aspect of energy management. Szarka et al. [71] present depth research review on power conditioning and power management techniques for kinetic energy harvesting systems. Harb [75] reviewed energy harvesting for low-power systems, as well as the state-of-art of energy harvesting techniques, power conversion, power management, and battery charging.

Vullers et al. [73] summarized the energy harvesting techniques from various power sources, such as motion, heat, the sun, and radio waves. Vullers et al. [8] summarized the recent energy harvesting research in the field of thermal, motion, vibration and electromagnetic radiation, and their power management circuits. They have also summarized the output power that could be obtained from various energy sources available in the ambient, including the vibration/motion of the human body [8].

As the mechanical movement, the vibration is a popular energy source for harvesting. Sodano et al. [78] discussed energy harvesting from vibration source using piezoelectric materials. Anton et al. [79] summarized the advancements of power harvesting based on piezoelectric materials and technologies in 2003 – 2006. Kim et al. [59] reviewed energy harvesting from mechanical vibration based on piezoelectric technology. Harne and Wang [80] reported the major efforts and findings on vibration energy harvesting via bi-stable systems. Invernizzi et al. [72] have reviewed the main processes and phenomena that can be used for vibrational energy harvesting, as well as the materials of interest, with particular attention to the activation frequencies of interest for human motion (1-10 Hz).

As a type of vibration, human motions are movements characterized by low frequency and high amplitude displacements and are the combination of low-frequency vibrations ($<$ 10 Hz) that vary from activity to activity and from person to person [88]. Gorlatova et al. [88] have provided the measurements of motion frequencies and

harvested power from 4 typical human motion activities (relaxing/walking/running/-cycling) based on an accelerometer. The available energy from human daily activities has been summarized in Table 2.1. As shown in Table 2.1, the available energy from different human motions in daily lives varies in a relatively large range (from 6.9 mW to 67 W) [89][90][17][91].

Table 2.1
Summary of the available energy from human motions in daily lives.

Motions	**Power**	**Motions**	**Power**
Ankle motion	$\sim$ 33.4 W	Knee motion	$\sim$36.4 W
Hip motion	$\sim$ 38 W	Heel strike	2 - 20 W
Bicep curls	$\sim$ 24 W	Arm lifts	$\sim$ 60 W
Elbow motion	$\sim$ 2.1 W	Shoulder motion	$\sim$ 2.2 W
Walking	$\sim$ 67 W	Respiration	$\sim$ 1.0 W
finger movement	6.9 - 19 mW		

Human motion, as a vibration source that can provide a reasonable amount of energy to be harvested, has become a focus of attention from researchers. Poulin et al. [77] have studied the capability of harvesting human mechanical energy by the electromagnetic system and piezoelectric system. Riemer et al. [17] focused on reviewing biomechanical energy harvesting from human motion. They reviewed different applications for human motion harvesting by integrated the power scavenging techniques into different equipment, such as backpack and knee devices.

Researchers have put great efforts into building different energy harvesting systems to

convert mechanical energy from human motion into electricity. Rome et al. [92] have developed a suspended-load backpack (weighing 20 to 38 kg) to convert mechanical energy from human walking into electricity (up to 7.8 watts). Donelan et al. have developed a biomechanical energy harvester that generates electricity during human walking [93]. The harvester can scavenge energy from subjects walking and produce an average power of 5 watts per device on one leg. Xie & Cai [74] have reported a backpack-based harvester and an insole-like harvester for harnessing kinetic energy from human motion. Qian et al. [95] have designed and tested embedded piezoelectric footwear for energy scavenging from human walking. The experimental results showed that an average power of 9 mW/shoe could be harvested by the footwear at the walking speeds of 3.0 mph (4.8 km/h).

For human motion energy harvesting, researchers have proposed smart ideas to improve the design of energy harvesters enhancing power density, such as nonlinear monostable ([85]), bistable ([86]) and tristable ([87]) piezo-structures. However, there are still big challenges towards harvesting energy from human motion due to its nature of irregularity and low frequency.

In recent 5 years, flexible energy harvesters based on triboelectric generators (TENGs) have received more notably attention since the first TENG was developed in 2012 [19]. Ha et al. [84] and Fan et al. [21] summarized the recent progress of TENGs in 2015 and 2016. Researchers start to apply TENGs into harvesting energy from human

motion. A few devices have then been demonstrated to harvest human motion and power wearable electronics with harvesters embedded on shoes ([96]) or attached to cloth ([97]). Vasandani et al. [94] have designed a contact-separation mode based TENG to harvest energy from the respiratory motion. A maximum area power density of 7.584 mW/m^2 has been achieved in their experiments.

In this section, energy harvesting has been reviewed first, following by the popular energy source for harvesting - vibration. As a vibration source that can provide a reasonable amount of energy to be harvested, the human motion has been reviewed by focusing on energy harvesting related systems and applications. Finally, TEHs applying into harvesting energy from human motion has been reviewed. The state-of-the-art energy harvesting techniques, especially for human motion, in recent years, have been proposed by the researchers.

2.3 Power Management for Triboelectric Energy Harvesters

For power management for TEHs to power electronics, full-wave bridge rectifiers are commonly used for AC-DC conversion in current triboelectric energy harvesting studies. Pu et al. [97] used a full-bridge rectifier to reverse the negative current of a TENG into positive. Pu et al. [98] stored the energy harvested from TENGs into

a capacitor to charge the electronics. The energy was directly transferred from a full-bridge rectifier.

A wide variety of TENGs have been proposed in the state of the art with innovative design, improved power, and flexible and diverse characteristics for various applications; they often adopted bridge rectifiers for converting AC triboelectric pulses to DC power. Some commercial power management integrated circuits (PMICs) with a full-wave bridge rectifier and a buck converter have also been applied for TENGs. Ryu et al. [99] utilized a commercial PMIC (LTC3331, Linear Technology) to provide boosted output current up to at 4.5 V. Chen et al. [100] applied a commercial power management circuit (LTC3588-1, Linear Technology) to convert the AC output of the TENG to a sustainable DC output of 3.3V. These PMICs usually integrate a low-loss full-wave bridge rectifier with a high-efficiency buck converter to boost the current.

Full-wave bridge rectifiers are no doubt a simple and effective way to achieve DC power from TEHs but have the limitation of low power efficiency for mechanical energy harvesting. To address the limitation, a few remarkable studies have recently been proposed, in which buck-converters are introduced to improve the power efficiency of DC-DC conversion for triboelectric energy harvesting.

Notably, Bao et al. [101] have demonstrated a power management circuit consisting of a DC-DC management circuit and a bridge rectifier for AC-DC conversion for TENGs. The proposed power management circuit mainly includes the full-bridge

rectifier and DC-DC management circuit. The DC-DC management circuit is a buck-boost static converter that consists of a parallel small capacitor, a serial switch, a parallel inductor, and a parallel diode. The switch is automatically controlled by a control unit based on comparing the load voltage and the small capacitor. A rotating TENG with maximum energy output of 106 mW at 170 rpm is used for the experimental verification. The experimental results show that the energy transferring to the storage capacitor can reach up to 53 mW, which indicates the energy efficiency is up to 50% with implementing the power management circuit.

A universal power management strategy using DC buck conversion for TENGs has been proposed by Xi et al. [102]. The authors firstly maximized the energy transfer from the TENG to the back-end circuit by controlling a switch based on the status of the open-circuit voltage. Then they coupled a classical DC-DC buck converter in the conversion circuit. The classical buck converter usually consists of a parallel freewheeling diode, a serial inductor, and a parallel capacitor between the rectifier and the load. The switch applied in the previous stage was also utilized to control the DC buck conversion. A function in the power management module was the self-management, which was mainly the sequential control of the switch. The autonomous switching was achieved by a micro-power voltage comparator to decide when the switch was on and off, and a MOSFET as the low-loss switch. The authors claimed that with the implemented power management module, about 85% energy can be autonomously released from the TENG and output as a steady and continuous DC

voltage on the load resistance.

Cheng et al. [103] have introduced the optimized inductor-capacitor oscillating into a power management circuit to improve the charging efficiency in TENGs. The experimental results show that with the proposed power management circuit, the transferred energy is over 2,600 times than the energy achieved by the full-bridge rectifier. An AC-DC power transfer efficiency of more than 72% has been obtained for different modes TENGs.

Park et al. [104] proposed a buck converter with maximum power tracking for TENGs. The buck converter features high input voltage (up tp 70 V), dual inputs, and with maximum power point tracking (MPPT). Benefit from the MOSFETs in the structure design, the proposed buck converter needs no additional switch, which decreases the internal power consumption. The experimental results show that the proposed system exhibits a maximum MPPT efficiency of 97% and a maximum power conversion efficiency of 51.1%.

Among these studies, the proposed buck-converters generally integrate a switching device and an inductor to lower the dissipation of harvested energy from the bridge rectifiers to the load. These studies solved the main issue of the impedance matching with different loads. These designs show universality and high-efficiency in DC-DC stage for different modes of TEHs [101][102][103][104].

Some studies have applied switching techniques into the power management of TENGs, which provides a research direction for the DC-DC conversion in power management studies of triboelectric energy harvesting. Qin et al. [105] investigated transferring and storing energy from TENGs with unidirectional switches and passive power management circuits. Vasandani et al. [106] used a synchronous switch to enhance the output performance of TENGs. The switches are equipped into the power management circuit with a bridge rectifier to prevent charge leakage.

In this section, power management methods, mainly the rectifying strategies, have been reviewed. For TEHs, the full-bridge rectifiers are commonly adopted in the AC-DC stage. Researchers mainly focus on improving the power efficiency of TEHs on the DC-DC stage. Some commercial PMICs consisting of a buck converter have been utilized in some studies. The power management strategies using DC buck conversion have been proposed by researchers in recent years. For the AC-DC stage, however, no existing studies have been identified so far to design rectifiers for TEHs to enhance power efficiency other than adopting bridge rectifiers.

2.4 Wireless Wearable Systems for Biopotential Monitoring

Researchers have provided multiple solutions from both electrodes and electronic design to improve ECG, EMG, and EEG monitoring. Fensli et al. [107] described a new wireless wearable ECG monitoring system concept. This system concept is intended to follow up with critical patients while they are carrying out daily activities. Park et al. [108] developed a wearable ECG monitoring system based on a new class of miniature, ultra-low noise, and capacitive sensor. In their study, the performance of the capacitive sensor is comparable to the gold standard ECG electrodes. Lin et al. [109] present a wireless ECG detecting system for early atrial fibrillation detection. Penders et al. [110] built a low-power wireless ECG platform which integrated into a necklace and allowed reliable cardiac activity monitoring on the move. Mass et al. [111] proposed a wireless wearable ECG monitor for real-time epileptic seizure detection. Luev et al. [112] present a multichannel wireless system for EMG measurement. Kobayashi [113] dealt with a wireless system for EMG/ECG acquisition. They integrated the wireless transmission modules into the electrodes.

In the recent 5 years, the researchers have greatly contributed by developing the wireless wearable systems for biopotential monitoring. Xu et al. [114] have proposed an

8-channel wearable system for biopotential monitoring. The proposed wireless system is capable of recording EEG and electrode-tissue impedance (ETI). Xu et al. [115] have developed a wearable system for multiple biopotential measurements including the ECG/EMG/EOG/EEG. The proposed system features up to 16 digital active electrodes (15 channels) and achieves state-of-art performance on the measured signal. Li et al. [116] have built a wearable system for EEG monitoring. It is designed based on a smartwatch for detecting driver drowsiness by monitoring the driver's EEG during driving. The wearable system is mainly designed to acquire the EEG signals, then transfer the data to the smartwatch via Bluetooth. Imani et al. [117] have developed flexible wearable biosensing system for real-time health and fitness monitoring. Rachim and Chung [118] have built a wearable armband for mobile ECG monitoring. The electrodes for the monitoring system are non-contact. The armband is capable of communicating with a smartphone via Bluetooth. Sun et al. [119] have developed a wearable Health-Shirt for exercise ECG monitoring. The ECG acquisition system was mounted on the T-shirt, then wirelessly connected to the smartphone via Bluetooth. ECG monitoring experiments at different exercise intensities and the heart rate-based lactate threshold computations were performed to testify the exercise ECG monitoring performance of the system. Mahmud et al. [120] have designed and developed a wireless health monitoring system that mounted on a mobile phone case. The phone case is 3D-printed. The monitoring system communicates with a smartphone via Bluetooth. Liu et al. [121] have developed non-contact electrodes based

on multi-layer flexible printed circuits materials for biopotential monitoring. They have tested the non-contact electrodes on detecting ECG and EMG signals. The experimental results show that the signal quality acquired by the proposed non-contact electrode is comparable to the commonly used wet electrodes. Table 2.2 presents a comparison among the wireless wearable systems for biopotential monitoring in recent 5 years (2014 - 2018). In order to narrow the scope of comparison, we specify the type of electrodes to only dry contact or non-contact.

In this section, the wireless wearable systems with dry contact or non-contact for biopotential monitoring in recent 5 years have been reviewed. Biopotential signals are most commonly recorded in one channel. Conductive fabric or textile is the most common active material for dry contact or non-contact electrodes. The wireless systems mainly adopted 2.4 GHz wireless protocols for data transmission, including various types of Bluetooth and Zigbee. During the reviewed systems, the ADC for converting the biopotential signals into digital data has a resolution of a range from 10-bit to 24-bit. The range of sampling rate is from 100 Hz to 2 kHz. The summary is based on the available collected data in this section.

Table 2.2
Comparison of wireless wearable systems for biopotential monitoring with dry contact or non-contact electrodes in recent 5 years.

Year	Ref.	Biopotential Type	Channels	Electrode Type	Active Material	Electrode Size	Data Transmission	Signal Acquisition Module			
								ADC	Sampling Rate	Size	Weight
2014	[122]	ECG	1-ch	Dry contact	Ni/Cu coated on urethane polymer foam	14 mm × 8 mm × 8 mm	Bluetooth v2.0+EDR	12-bit	512 Hz	4 cm × 2.5 cm × 0.6 cm	-
2014	[114]	EEG/ETI	8-ch	Dry contact	-	Dia: 11 mm	-	12-bit	1 kHz	-	-
2015	[115]	ECG/EMG/ EOG/EEG	15-ch	Dry contact	-	-	-	12-bit	250 Hz - 2 kHz	15.8 mmˆ2	-
2015	[116]	ECG	1-ch	Dry contact	Conductive fabric	-	Bluetooth Smart	10-bit	128 Hz	-	-
2016	[118]	ECG	1-ch	Non-contact	-	3 cm × 3 cm	Bluetooth 4.0	10-bit	100 Hz	-	-
2016	[123]	ECG	1-ch	Dry contact	Copper plates	3 cm × 3 cm	2.4-GHz RF	10-bit	500 Hz	-	-
2016	[124]	ECG	1-ch	Dry contact	Conductive rubber	-	Zigbee	24-bit	320 Hz	65 mm× 34 mm × 17 mm	16 g
2016	[117]	ECG	1-ch	Dry contact	Prussian blue ink, hydrogen peroxide	1.5 cm × 1.5cm	Bluetooth	-	-	7 cm × 2 cm	-

Continued on Next Page...

Table 2.2 – Continued

Year	Ref.	Biopotential Type	Channels	Electrode Type	Active Material	Electrode Size	Data Transmission	Signal Acquisition Module			
								ADC	Sampling Rate	Size	Weight
2017	[119]	ECG	1-ch	Dry contact	Conductive fabric	-	Bluetooth Low Energy	-	250 Hz	15 mm × 50 mm × 1.5 mm	10 g
2017	[125]	ECG	3-ch	Dry contact	Hook-shaped Ag on polyester film	Dia: 34 mm; 36 mm	Bluetooth	24-bit	1 kHz	80 mm × 42 mm × 10 mm	17.9 g
2017	[120]	ECG	1-ch	Dry contact	Silver-coated plates	-	Bluetooth Low Energy	12-bit	-	-	-
2017	[126]	ECG	1-ch	Dry contact	Conductive textile	40 mm × 40 mm	-	16 bit	-	-	-
2017	[127]	ECG	1-ch	Dry contact	Flexible printed circuit substrate, polyimide on copper film	-	Bluetooth	16-bit	125 Hz	-	-
2017	[128]	ECG	3-ch	Dry contact	-	-	Bluetooth GSM/GPRS	19-bit	250 Hz	-	-
2018	[129]	ECG/EMG	1-ch	Dry contact	Stainless steel contact plates	Dia: 10 mm	-	24-bit	-	-	-
2018	[130]	EEG	8-ch	Dry contact	Carbon fiber pins, filled PDMS/CNT	Dia: 17 mm	Bluetooth	24-bit	250 Hz	-	-

Continued on Next Page...

Table 2.2 – Continued

Year	Ref.	Biopotential Type	Channels	Electrode Type	Active Material	Electrode Size	Data Transmission	Signal Acquisition Module			
								ADC	Sampling Rate	Size	Weight
2018	[131]	ECG/BCG	1-ch	Dry contact	Soft conductive fabric	Dia: 1.2 cm	-	-	500 Hz	-	-
2018	[121]	ECG/EMG	1-ch	Non-contact	Multilayer flexible printed circuits	Dia: 2.5 cm	802.11 b/g/n WiFi	24-bit	2 kHz	-	-

2.5 Summary

In this chapter, the literature review has been represented that includes the three types of electrodes for biopotential monitoring, techniques for harvesting energy from human motion, power management strategies for a specific type of harvesters - TEH, and the latest wearable systems for monitoring common biopotentials in recent 5 years. Based on the literature review, the main challenges to achieve the desired wearable system for long-term biopotential monitoring can be summarized as below:

1) Considering the user comfort, the traditional contact electrodes are not suitable for long-term monitoring. Therefore, a proper type of electrodes, non-contact electrode, needs to be obtained and developed. Due to the variations happened on the electrode-skin interface, the stability of the non-contact electrode with the current design is not ideal for monitoring biopotentials.

2) Energy harvested from human motion is an appropriate power supply for wearable electronics because of the wearability requirement. However, harvesting energy from human motion is still challenging due to its nature of irregularity and low-frequency.

3) Due to the low energy efficiency, the traditional full-bridge rectifier needs to be replaced by a proper rectifying strategy for TEHs. The highly changeable inner

capacitance of TEHs leads to difficulty of achieving optimal synchronized switching time for the latest inductor-based switching rectifying strategy for TEHs.

4) Wearable systems equipped with non-contact electrodes feature high wearability and flexibility in biopotential monitoring. However, there are still not many wearable systems adopting non-contact electrodes for biopotential monitoring in recent years, especially for monitoring multiple biopotentials. The power consumption of the wireless system also needs to be optimized.

Therefore, correspondingly, four major tasks need to be addressed before achieving the desired system in this study: 1) Design and validate the non-contact electrodes for long-term biopotential monitoring; 2) Developing the TEH for harvesting energy from human motion; 3) Proposing an SSHI rectifying strategy to enhance the power efficiency for TEHs; 4) Building the wireless wearable system for monitoring multiple biopotentials with considering optimizing the power consumption on wireless transmission.

Chapter 3

Non-contact Electrode for Biopotential Monitoring

3.1 Introduction

Building a non-contact electrode for biopotential monitoring is the first proposed research objective. In this chapter, the non-contact electrode will be developed with a feedback design to increase stability. The performance of the non-contact electrodes is evaluated on a novel wearable system.

The wireless biopotential monitoring system can be divided into three major modules, the biopotential detection, the wireless transmission, and the power supply module.

The biopotential signal detecting module consists of a pair of active electrodes, an analog front end (AFE), ADC, and a signal processing back end. The AFE supports concurrent two-channel biopotential monitoring for ECG/EMG/EMG detection. The back-end adopts ATmega328P and Arduino Bootloader, converting the analog signals into digital data via an internal 10-bit ADC and then processing the data. The wireless module includes the nRF24L01+, a low-cost, easily-applied wireless module, which operates on 2.4 GHz ISM band with up to 2 Mbps data rate and low power consumption. The nRF24L01+ transmits the data from ATmega328P via SPI to the gateway wirelessly. Our Triboelectric energy harvesters, a Lithium-ion battery, and a power management circuit are used as the power supply module. The system architecture of the wireless biopotential monitoring system is shown in Fig. 3.1.

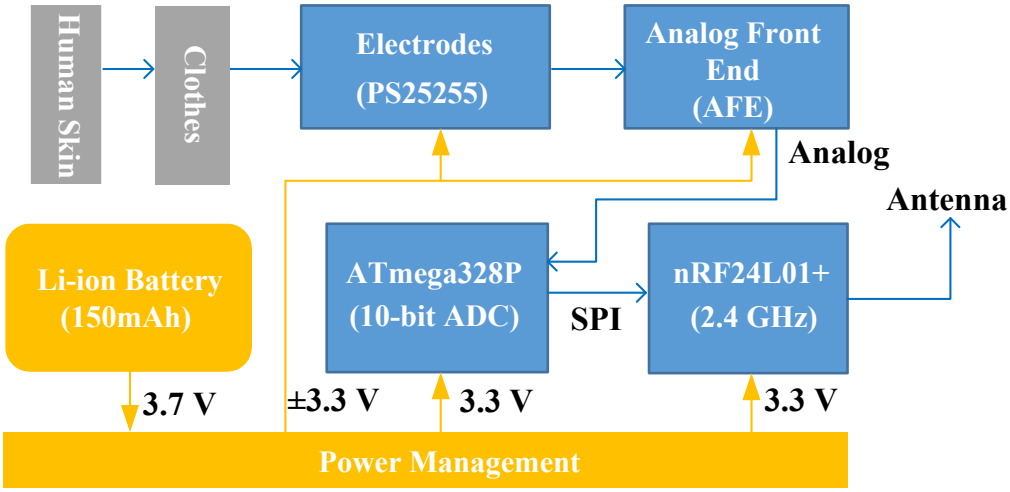

Figure 3.1: System hardware architecture of the Biopotential monitor.

3.2 Active Non-contact Electrodes Using Feedback Design

In the physical modeling of the non-contact skin-electrode interface, there are multilayers between skin and electrode including stratum corneum (SC), cloth, and air, which can be modeled as a resistor and capacitor (RC) parallel to each other as shown in Fig. 3.2 [65]. For non-contact detection, an active electrode is generally used to achieve high input impedance to collect the weak biopotential signals through the cloth. The equivalent circuit model is shown in Fig. 3.2. Therefore, the skin-electrode impedance can be simplified as Eq. 3.1,

$$Z_s = R + \sum_{i=1}^{n} R_i || \frac{1}{j\omega C_i} \tag{3.1}$$

where R is the total resistance of the conductive layer in the path which is negligible in the calculation; R_i and C_i are the resistance and capacitance for a certain layer, respectively; n is the number of layers.

Usually, the impedance of the air layer is very high and dominate the skin-electrode impedance due to the small capacitance C_{air}. In order to pick the signal of interest from human skin, an ultra-high input impedance on electrodes or AFE is required.

Therefore, we adopt an active electrode to achieve high input impedance. In this design, we choose PS25255 (Plessey Semiconductors Inc.) to design the active electrode. The input capacitance can be as low as 15 pF. A positive feedback is included in PS25255 to achieve this high input impedance, equivalent to C_f in Fig. 3.2 (Adopted from [65] with permission).

In this study, the non-contact electrodes are developed based on PS25255 EPIC which features ultra-high input impedance using positive feedbacks [132]. The Biopotential monitor can monitor ECG signals without directly contacting the human body, which reduces the chance of infection and makes recycle using possible. In addition, PS25255 has a voltage gain of 10, which can reduce the number of amplifiers in AFE and minimize the circuit.

The typical application circuit of PS25255 is shown in Fig. 3.3 (without red lines). In the study, we improved the circuit by introducing a single feedback loop in each electrode as the red lines in Fig. 3.3. The feedback is actually not necessary to be attached to the same location of skin as PS25255 sensing plate. One single feedback in the differential pair can also improve the detecting performance of the biopotential signals. The stability can be significantly enhanced by introducing the feedback to the skin. The comparison experiments and testing results are shown in the validation experiments in Section 3.5.

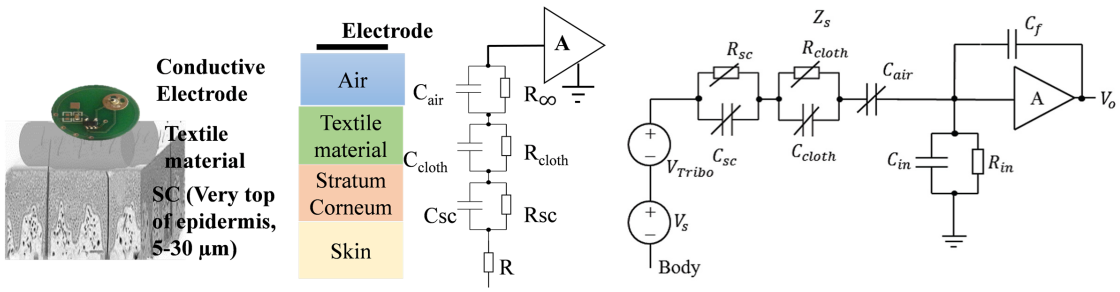

Figure 3.2: Skin-electrode interface for non-contact electrodes.

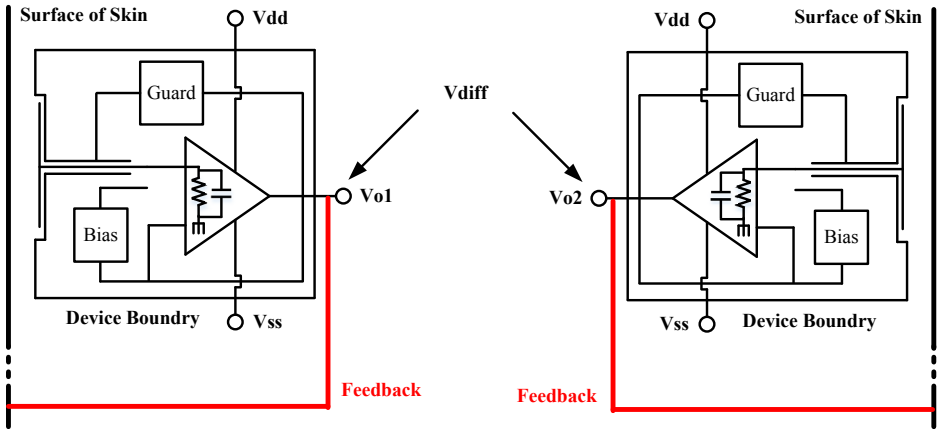

Figure 3.3: The way of adding the feedback cables (red lines) to PS25255 applications.

3.3 AFE

The AFE circuit used in the system is shown in Fig. 3.4. First, the differential inputs are connected to an instrumentation amplifier. Because of its low-cost and low voltage supply features, an AD623 has been used in this study. The instrumentation amplifying circuit is followed by a 0.07 Hz High Pass Filter (HPF), a 60 Hz Notch

Filter and a 100 Hz Low Pass Filter (LPF). In non-contact detection, the biopotential signals can be ten times lower than wet contact, which need to be amplified by the instrumentation amplifier and the second stage amplifier. The gain can be adjusted to be suitable for different types of biopotential signals. Due to the dual-supply of AFE circuit, the voltage of the output signal needs to be lifted to fit the analog input of the signal processing back-end. A simple summing amplifier has been adopted in the application.

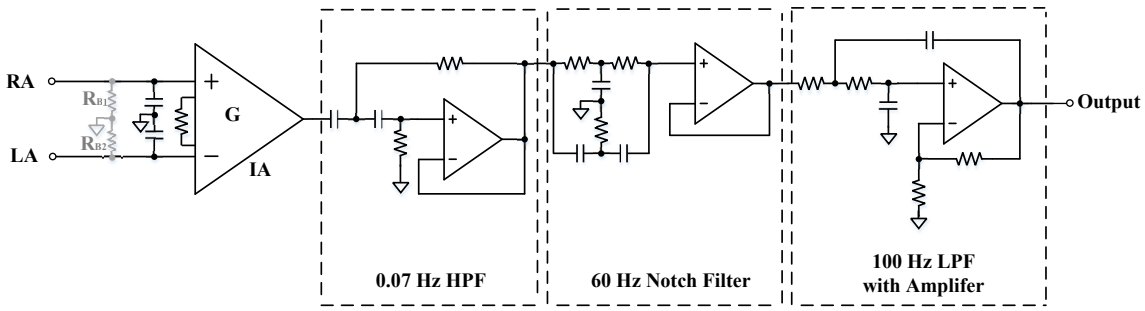

Figure 3.4: The AFE circuit.

3.4 Packaging

The entire system physically contains the Patch and the Gateway. The packaging of the system is designed and developed using 3D Printing technology. In our design, each case consists of two parts: the base and the cover as shown in Fig. 3.5. The Patch case hosts the electronics part, which provides a physical isolating environmental from the human body and cloth. The Gateway case holds the data transceiver module.

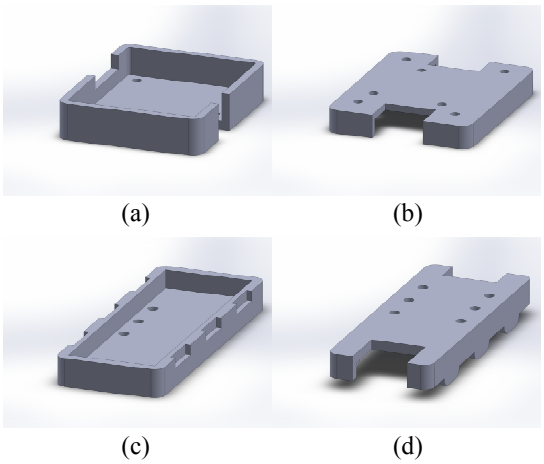

Figure 3.5: Case designs of the Patch and the Gateway. (a) Base and (b) cover of the Patch case; (c) base and (d) cover of the Gateway case.

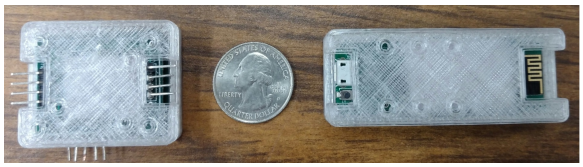

Figure 3.6: The actual sizes of the Patch and the Gateway.

The Gateway directly connects to PC via USB port and drains power from the USB port. The sizes of the Patch and the Gateway are 39 mm × 32 mm × 17 mm and 69 mm × 27 mm × 14 mm, respectively. The photo of the Patch and the Gateway is illustrated in Fig. 3.6. The total weight of the Patch is 24.0 g. The advantages of small size and lightweight make the Patch suitable for wearable applications, like being integrated into smartwatches, smart gloves, and smart helmets.

3.5 Electrodes Validation

Among the biopotential signals, ECG is a typical periodic signal. So, ECG monitoring is first applied to validate the design of the proposed wireless wearable system. In order to validate and calibrate the performance of the design with the feedback, PS25255 is used as dry contact electrodes to detect the ECG signals by contacting the electrodes with human skins. We compare the outputs of the feedback design and the normal design, which does not assemble the non-contact electrodes. In addition, the performances of electrodes with and without feedback have also been compared.

In the following experiments of ECG detection, the electrodes are placed on both hands of the subjects. As shown in Fig. 3.7, the subject used the thumbs and index fingers to hold the electrode and cloth tightly. The isolation layer of the electrode and the cloth sheet ensure the sensing layer of the electrode non-contacting with the skin. As such, the non-contact performance of the system can be tested.

In order to validate the performance of the feedback design proposed in Section 2.1, the button is used to detect ECG signals in different contacting conditions. The electrode, which is equipped with a feedback loop from the output pin to the skin, is called the feedback design in our study. On the contrary, the electrode without any feedback loop is the non-feedback design. The point of contact for the feedback loop

with human skin is as small as the cross-section of a conductive wire. The proposed feedback loop of the electrode has been also demonstrated in Fig. 3.7.

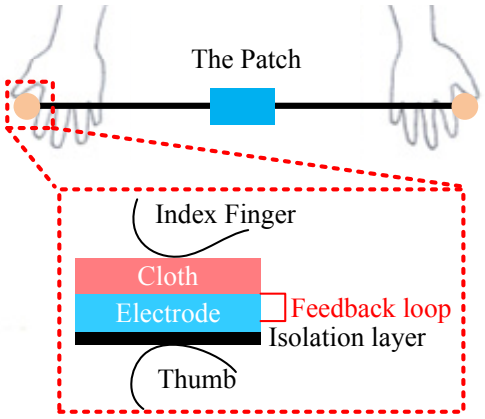

Figure 3.7: The diagram of system settings for measuring ECG signals.

First, the performances of non-contact electrodes with and without the feedback designs have been compared in terms of signal-to-noise (SNR). The ECG signals detected from the feedback and non-feedback designs are shown in Fig. 3.8 (a) and Fig. 3.8 (b), respectively. Both designs can detect ECG signals successfully. However, the feedback design has a higher SNR of 4.406 dB, while the non-feedback design has only 1.136 dB. It means that the feedback design is capable of reducing more noises and providing higher quality signals.

Then, the performances have been compared in terms of resisting to motion artifacts. Motion artifact is one of the major problems preventing accurate and successful biopotential monitoring. In out-of-hospital scenarios, multiple types of motions possibly

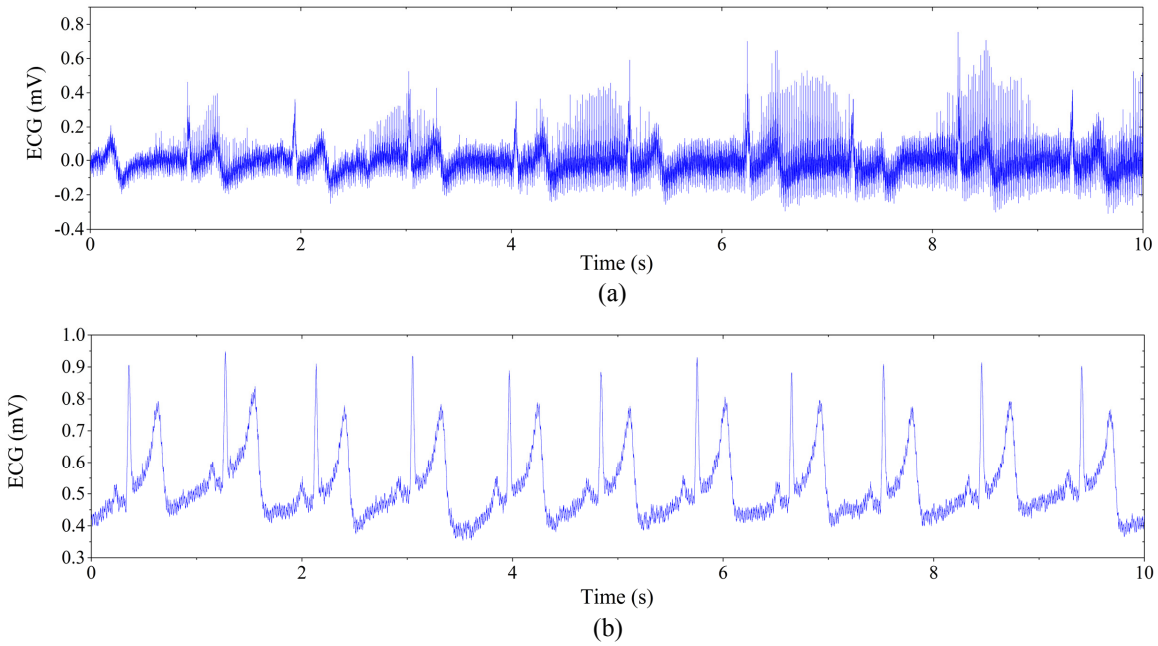

Figure 3.8: Raw ECG signals with (a) regular dry contact and (b) feedback design.

occur in realistic applications. As such, we investigated the performance of the feedback design with motion artifacts.

Three different types of motions, pressing, moving, and sliding, were applied to the electrodes with or without the feedback. In order to facilitate the description of these motions, two sensors, a force sensor (FlexiForce A201, Tekscan Inc., Boston, MA, USA) and an accelerometer (333B50, PCB Piezoelectronics Inc., Depew, NY, USA), were attached to the electrodes to record the pressing force and acceleration, respectively. The effects of these two sensors on the electrodes have been excluded. Typical simultaneous ECG, pressing force, and acceleration signals are shown in Fig. 3.9.

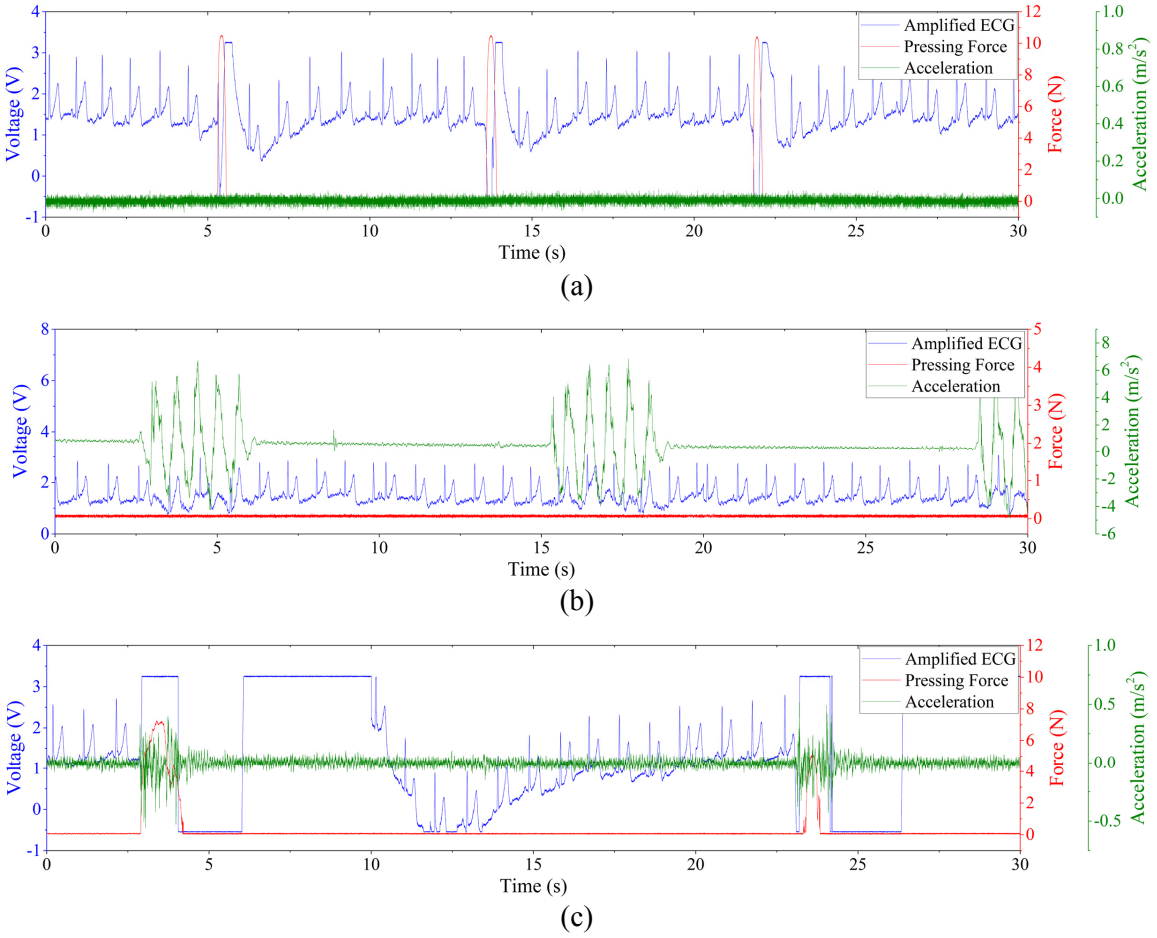

Figure 3.9: ECG detection with 3 movements applied on the electrodes, a) pressing; b) moving; c) sliding.

In Fig. 3.9 (a), the force signal represented the moments of pressing and releasing the electrode. Once the electrode was pressed, the ECG signal became out of range instantly. After a relatively long period, the ECG signal recovered to be stable. The stable acceleration signal indicated that the pressing processing was performed in a very short distance without large movement. Fig. 3.9 (b) shows the detected signals during the significant moving motion. The stable force signal indicated that there was no obvious pressing force on the electrodes. The acute acceleration signal indicated

that the electrode was moved in several shakes. However, the baseline of the ECG signal only fluctuated slightly during moving motion. The amplitude of the ECG signal kept inside of the voltage range. The effects of sliding motions on electrodes were shown in Fig. 3.9 (c). The severe force signal and mild acceleration signal implied the difference of the sliding motion from pressing and moving motions. The most dramatic changes in the ECG signal among all these three motions happened on the sliding motions. The ECG signal affected by sliding motions needed a much longer time to recover and had a much less stable baseline.

A quantitative analysis method is provided in this study to compare the different performances of the feedback and non-feedback designs under motion artifacts. Three parameters are proposed to quantify stability and recovery from motion artifacts. Recovering Time (RT) refers to the duration from the moment that the ECG signal becomes unstable until the moment that it recovers to the stable status. Out of Range Time (ORT) refers to the duration that the ECG signal staying out of the voltage range of the power supply. Out of Range Percentage (ORP) refers to the percentage of the ORT over the entire testing time. These three parameters are measured and summarized in Table 3.1 for both feedback and non-feedback design affected by different motions. In Table 3.1, for the same comparison item, lower values represent fewer effects of motion artifacts on detection performances. In other words, the design which has lower values of the same parameter has a more stable performance during motion artifacts. Comparing to the non-feedback design, most

of the parameters of the feedback design significantly have lower values. The only exception is the ORT during moving motions. The out-of-range event only happened once out of 26 times in the feedback design during moving motions. However, it occurred 6 out of 17 times on the non-feedback design. The ORPs (3.85% and 35.29%) showed a big difference.

Table 3.1
Results of different motions on feedback and non-feedback designs.

Movements	Feedbacks	RT (s)	ORT (s)	ORP
Pressing	Feedback	4.0231	1.1063	100.00%
	Non-Feedback	8.5338	3.2837	100.00%
Moving	Feedback	4.0178	3.5170	3.85%
	Non-Feedback	7.7329	1.3847	35.29%
Sliding	Feedback	16.4894	7.3549	100.00%
	Non-Feedback	17.9953	7.6239	100.00%

The higher SNR and those statistical results in Table 3.1 show the better performance of the proposed feedback design in this study. The feedback design has a much more stable performance than the non-feedback design. During ECG monitoring, the stability and fast recovery from motion artifacts of the proposed system can be significantly enhanced by introducing the feedback design. This conclusion can be also applied to other biopotentials in our study.

3.6 Conclusion

In this chapter, a new type of electrodes, non-contact electrodes, with a novel feedback design has been developed for long-term biopotential monitoring. In order to evaluate the performance of the proposed non-contact electrodes, a prototype of the wireless wearable system has been designed. The hardware structure with other technical details, including AFE and packaging, has been represented. Finally, the non-contact electrodes are validated by comparing the biopotential signals detected in the experiments with and without the non-contact electrodes on the system prototype. The experimental results show that the non-contact electrodes with the feedback design has high stability and fast recovery from motion artifacts, which indicates the proposed electrode is suitable for long-term biopotential monitoring.

Chapter 4

Triboelectric Energy Harvester

4.1 Introduction

Developing a Triboelectric Energy Harvester (TEH) for harvesting energy from human motion is the second proposed research objective. In this chapter, we report the design, experimental validation, and application of a scalable wearable e-textile triboelectric energy harvesting (WearETE) system for scavenging energy from activities of daily living to provide a power supply for our wearable system.

Generally, three mechanisms, piezoelectricity, electromagnetics, and electrostatics, are commonly adopted to convert mechanical energy to electricity. Triboelectric energy harvesting provides an alternative solution, which is applicable to human motion

energy harvesting. As an alternative mechanism that converts mechanical energy into electricity, Triboelectricity is a new type of energy harvesting technique and the first triboelectric energy harvester was introduced and developed in 2012 ([19]). However, to our best knowledge, the fundamental mechanism of Triboelectricity is still unknown. In this section, the mechanism of Triboelectric Energy Harvester will be introduced and studied first, following by the study of optimized power generating. Several possible designs of triboelectric energy harvester will be tested and practical design will be chosen for future development.

4.2 The Mechanism of Triboelectric Energy Harvester

Triboelectricity is a well-known phenomenon and often considered as harmful because it may cause damages to industrial electronics and non-comfort to human. Triboelectric energy harvesters use this harmful phenomenon to generate electrical power. Contact and separation, rubbing and friction between two different or even seemingly chemically identical materials, often result in electrical charge generation and distribution with opposite signs on either surface.

Human daily activities including walking, running, sitting and standing were calibrated in our previous publication [133]. When powering from human motion, there

is a random and low-frequency load as the input of the energy harvester. The relative movement of the two tribomaterials can be longitudinal or transverse corresponding to pressing and sliding.

With regard to real system design for mechanical energy conversion, the principle of inertia is generally used that a frame with a movable mass is attached to a vibrating source and the relative motion is controlled by the law of inertia. The system is made resonant by means of suspending the moveable part to a spring forming a unified mass-spring-damper system. Some kinetic energy of the moving mass is converted into electrical energy; whereas some are damped by parasitic effects of the system. A basic model of vibration acquisition is the mass-spring-damping system under force vibration. Eq. (4.1) is a general differential equation to describe the model.

$$m\ddot{x} + (c_{elec} + c_{mec})\dot{x} + kx = -m\ddot{y} \tag{4.1}$$

where x represents the motion of the mass; c_{elec} and C_{mec} are the damping effects caused by electricity conversion and parasitic effects, y is the frame movement. Assume in this case that the base of the mass-spring-damping system moves simultaneously with the force. Assume the reference the bottom part is fixed, the analytic solution for a random pulse input causing contact-separation is described as Eq. (4.2),

$$X = X_0 e^{-\zeta_1 \omega_1 t} cos(\sqrt{1-\zeta_1^2}\omega_1 t - \phi_1) \tag{4.2}$$

where X is the displacement of the mass relative to its equilibrium position; ζ_1 and ω_1 are the damping ratio and natural frequency of the object, respectively, $c = 2\zeta$; t is time, ϕ_1 is the phase angle of the displacement.

In the device, assume the area of layers are infinite comparing to the small separation distance. The generated potential on the electrode can be presented as Eq. (4.3),

$$U_{tribo} = \sum_{i=1}^{N} \sum_{j=1}^{M} E_{ij} X_j \tag{4.3}$$

where E_{ij} is the electrical field generated by the surface charges due to contact-separation, X_j is the thickness or distance of layer j. Therefore, the generated potential can be further calculated by Eq. (4.4),

$$U_{tribo}(t) = \frac{\sigma}{\varepsilon_0} x(t) \tag{4.4}$$

where σ is the surface charge density generated by contact and is also related to the material property, the constant ε_0 is the vacuum permittivity.

The mechanism of the proposed TEH has been shown in Fig. 4.1. The e-Textile and foam plates are flexible, so the plates in schematic have an arc during motion. However, in order to simplify the analysis, the part of both layers which have been totally contacted to each other during pressing only has been shown. The entire contact-separate-contact process can be constituted as one period. The schematic for an individual period has been represented in Fig. 4.1 (a)-(c). As the distance of two layers increases until the maximum separation, the open-circuit voltage rises towards a maximum value. The pressing process is the opposite. In a short-circuit condition, the resultant current appears as negative and positive pulses during each pressing and releasing cycle, which also shows periodicity. The mechanism of sliding is similar as illustrated in Fig. 4.1 (d)-(f).

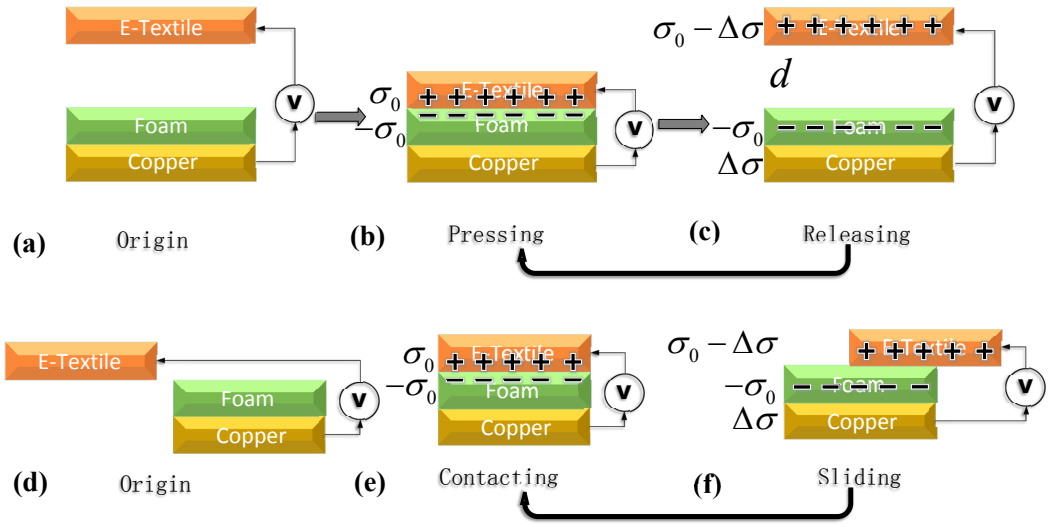

Figure 4.1: Mechanism of TEH. Pressing: a) original position; b) pressing; c) releasing. Sliding: d) original position; e) contacting; f) sliding.

4.3 Optimized Power Generation

Due to the randomness and irregularity of human motion, the measurement of input mechanical energy and power efficiency of human motion energy harvesters calls for a standard method for system performance calibration and evaluation. In this study, we propose a new measurement platform which can be used for calibrating random human motion energy conversion. In order to quantitatively estimate the power efficiency generated from low-frequency motion, a testing platform and the associated calculation methods are established. The power efficiency refers to the ratio of the generated electrical power to input mechanical power.

The power management circuit and energy storage component could influence the performance of harvesting energy of the TEH system. With the assumption that the internal circuit is independent of the external load, the power generated by TEH is approximately

$$P(\omega) = \frac{\sigma^2}{\varepsilon_0^2 R} X(\omega) \tag{4.5}$$

where R is the load resistance, ω is related to the excited frequency of external force during motion.

Usually, for piezoelectric energy harvesting, the maximum power can be harvested at the resonant frequency. Based on Eq. (4.5), in order to get the optimized power, small R should be chosen. In this study, we directly compose a capacitor to store energy and smooth the output voltage waveforms rather than assembling any resistors. In this case, R is the internal resistance of the capacitor. Usually, for piezoelectric energy harvesting, the maximum power could be harvested by a generator with a resonant frequency matched to the motion frequency. So, in order to get the optimized power, ω should be the resonant frequency (if any) of TEH. However, because of the low frequency and irregular nature of human motion, the triboelectric energy harvester may not be able to achieve the resonant frequency. In this study, we focus on the performance of the proposed system in the low-frequency range (<5 Hz). A capacitor is used to estimate the generated power, which can be calculated by

$$P_{out}(t) = \frac{dW}{dt} = CV(t)\frac{dV(t)}{dt} \tag{4.6}$$

where $V(t)$ is the voltage of the capacitor, C , during energy harvesting and can be measured by an oscilloscope; $P_{out}(t)$ is the generated power that stored in the capacitor at time t. The maximum power, P_{max} , can be found by Eq. (4.6) as well [134]. Then the generated average power $P_{avg}(t)$ during the time period t_i to t_j can be calculated as

$$P_{avg} = \frac{1}{t_i - t_j} \int_{t_i}^{t_j} P_{out}(t)dt \tag{4.7}$$

Generally, the equation $W_C = \frac{1}{2}CV^2$ represents the energy stored in the capacitor to calibrate energy output, where C is the capacitance, V is the potential difference (i.e., voltage) of the capacitor. It is therefore generally applied to calculate the energy stored in a charged capacitor. In our case when using a capacitor to calibrate the energy output, due to the energy leakage in the capacitor and the changing input mechanical energy during human motion, the voltage of the capacitor varies along with the time. The $V(t)$ stands for the changing voltage across the capacitor at an arbitrary time point t. Theoretically, $W_C(t) = \frac{1}{2}CV^2(t)$ then refers to the electrical energy output at the time point t. After integration with time, we can get the average energy in a time duration from t_1 to t_2. In light of that, Eq. (4.7) represents the average power output during the testing time period t_1 to t_2. Human motion has its nature of randomness and irregularity and therefore is challenging to calibrate as standard mechanical input. Thus, we are using an average value to represent the generated average electrical energy. The equation used to calculate average power (or effective power) in some similar studies is I^2R [135][136][137], which is normally adopted for calculating power based on the measured current I and the known resistance R. In our case, we use a load capacitor to calibrate the output energy, which is an alternative method and widely used to calibrate the output energy of energy harvesters [138][139][140]. As the goal of our study is to harvest the energy from

human motion (e.g. the hand clapping movements) and then store, the capacitors are suitable for storing the harvested energy as well.

To estimate the energy efficiency for kinetic energy harvesting, a known vibration input is generally adopted. However, there is no standard method to evaluate energy harvesting from human motion. In this study, we propose a measurement platform to quantitatively estimate the input power of human motion. Three signals are needed to calibrate the input human motion, including acceleration, velocity, and external force. The acceleration signal is obtained via a 3-axis accelerometer. The velocity can be then obtained via integration of acceleration. The external force signal is measured by a force sensitive resistor sensor (FlexiForce A201). There is a linear relationship between the external force applied to the sensor and the sensor resistance. This linearity can be obtained from the calibration data. A simple voltage divider is also applied to measure the voltage of the force sensor and then calculate the external force. For the measurement of acceleration, we used an accelerometer from PCB Piezoelectronics, Inc. (model 333B50) to measure in the input human motion. It has a sensitivity of ($\pm$10%) 102 mV/(m/s^2) with ultrahigh linearity, which is highly suitable for the human hand clapping movements. The voltage outputs of the accelerometer and the force sensor have been measured via an oscilloscope (PicoScope 4424, Pico Technology). The probes we used in the measurements are high impedance passive probes. The transferred data are analyzed offline. The typical synchronized signals are shown in Fig. 4.2, which corresponds to the motion process.

In Fig. 4.2, it is shown that the force signal became a very small value, which means the two substrates of the triboelectric energy harvester were nearly separated at that moment. Comparing with the output voltage of the WearETE system, it shows that the second peak of the output voltage comes from the separation motion. The small output voltage of WearETE at that moment may result from the moment of inertia.

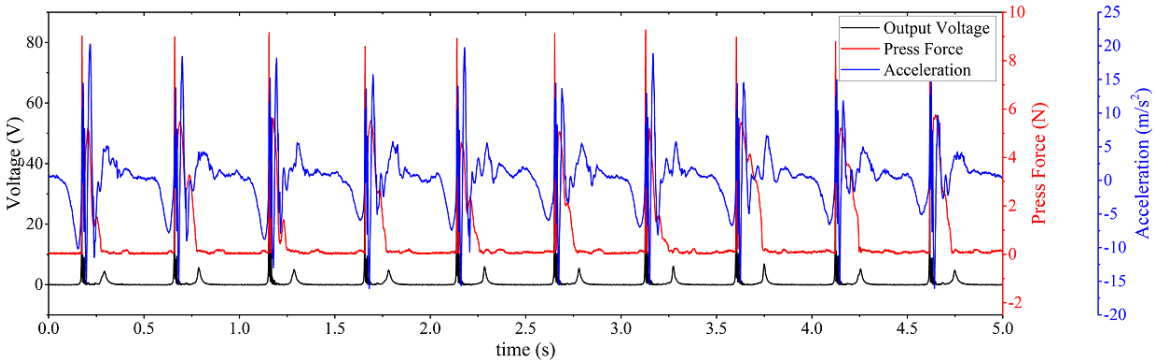

Figure 4.2: Typical synchronized measured signals during tapping including voltage output of energy harvester, force sensor, and accelerometer.

In the detected signals, multiple typical points are shown in the acceleration signal to divide the entire moving process into three sessions, which aligns with the real motion. The schematic of the three sessions has been shown in Fig. 4.3. In the first session (t_0 to t_1), the two substrates of WearETE move from their original points (i.e. maximum separation distance) to the point where they contact each other. In the second session (t_1 to t_2), the two tribomaterial layers keep contacting. Due to the moment of inertia, these two substrates keep moving for a short distance (less than their thickness) in the first half and then move in the opposite direction till the moment of separation in the second half. In the last one (t_2 to t_3), they move back to

the maximum separation distance. Finally, the two substrates are back to the original places as one period. Thus, the input power in the first and third sessions can be calculated from the acceleration signal as shown in Fig. 4.3 using Eq. (4.8); whereas that in the second session can be calculated from both the force sensor signal and the acceleration signal using Eq. (4.9).

$$P_{in1}(t) = m_1 \times v(t) \times a(t) \tag{4.8}$$

$$P_{in2} = m_2(t) \times g \times v(t) \tag{4.9}$$

where m_1 is the mass of one TEH layer; $m_2(t)$ is the measured external force during contacting; $v(t)$ and $a(t)$ are the velocity and acceleration of the layer during motion, respectively; g is gravity constant. Then the input power can be calculated by a piecewise function as Eq. 4.10,

$$P_{in}(t) = \begin{cases} m_1 \times v(t) \times a(t) & t_0 \leq t \leq t_1 \text{ or } t_2 \leq t \leq t_3 \\ m_2(t) \times g \times v(t) & t_1 \leq t \leq t_2 \end{cases} \tag{4.10}$$

For an individual hand-clapping motion, the power efficiency η for TEH could be

calculated by Eq. (4.11) within synchronized time duration for input power, P_{in}, and output power, P_{out}.

$$\eta = \frac{P_{out}}{P_{in}} \tag{4.11}$$

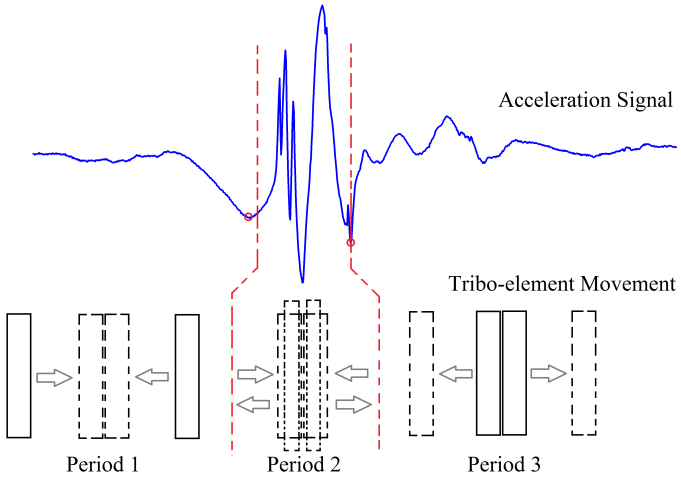

Figure 4.3: Schematic of tapping model.

4.4 Triboelectric Energy Harvester

In this section, the Triboelectric Energy Harvester has been experimentally validated by testing the output performance in two motion modes and the open-circuit voltage and short-circuit current. The process of choosing the materials for the TEH has also been provided. The potential of energy harvesting from human motion (e.g. hand-clapping movements) on the scalable TEH has been tested by powering LEDs.

A platform for measuring and calculating power efficiency is also established for measuring and calibrating random human motion. The harvested energy has been measured and calculated in this section. The TEH has also been applied to harvesting energy from human walking. The proposed WearETE system shows the possibility of powering wearable electronics during human motion using a wearable energy harvester.

4.4.1 Energy Harvester Validation

In the energy harvester validation experiment, we first test the open-circuit voltage and short-circuit current to calibrate the energy harvester performance and then measure the output on a regular oscilloscope without rectifier to compare with the cases with load capacitors for calibration. The oscilloscope used for testing the open-circuit voltage and short-circuit current in this study is an Electrochemistry Workstation (model: CHI660B, CHI Instruments, Inc.). The typical input impedance of the reference electrode is 10^{12} . The probes for measurements are high-performance passive probes with high impedance. The oscilloscope for system calibration with load capacitors is a regular digital oscilloscope (PicoScope 4424, Pico Technology). Triboelectric energy harvester can have two modes for harvesting human motion as shown in Fig. 4.1, the contact-separation mode, and sliding mode. The voltage outputs without the rectifier are shown in Fig. 4.4. For contact-separation motion, the

voltage output is more stable and has a larger magnitude than that during sliding motion. For sliding motion, due to its irregular nature, the voltage output is unstable but it still generates considerable power. The experiment results show that the power density is 17 $\mu W/cm^2$ under 5 Hz contact and separation and 11 $\mu W/cm^2$ under 5 Hz sliding. These results indicate that triboelectric energy harvester can harvest energy from both motions. An experiment has been conducted to test the open-circuit voltage and short-circuit current of the contact-separation mode. With the distance of the two layers, i.e. e-textile and foam, increasing until the maximum separation, the open-circuit voltage rises towards a maximum value following Eq. (4.1). The pressing process is the opposite. In a short-circuit condition, the resultant current appears as negative and positive pulses during each pressing and releasing cycle. The experimental results of the open-circuit voltage and short-circuit current as shown in Fig. 4.5 (a)-(c) align with the theoretical analysis.

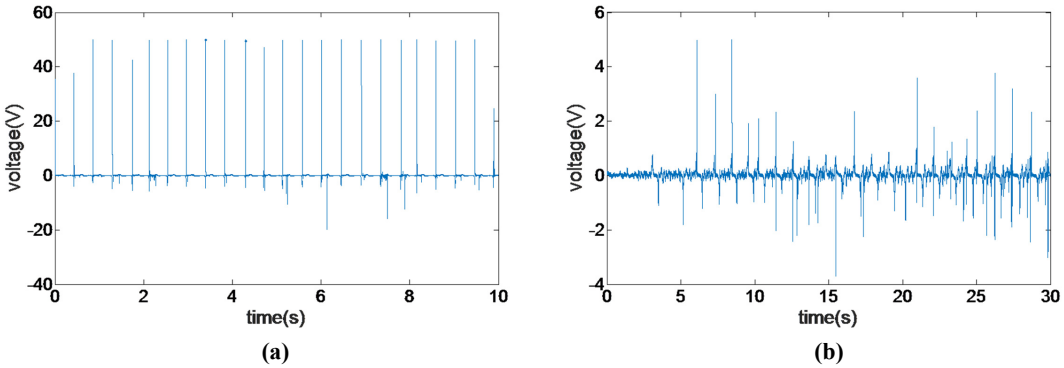

Figure 4.4: Performance of the harvester during (a) contact-separation motion and (b) sliding motion.

To select the two contact textile materials as discussed in Section 4.3, an experiment

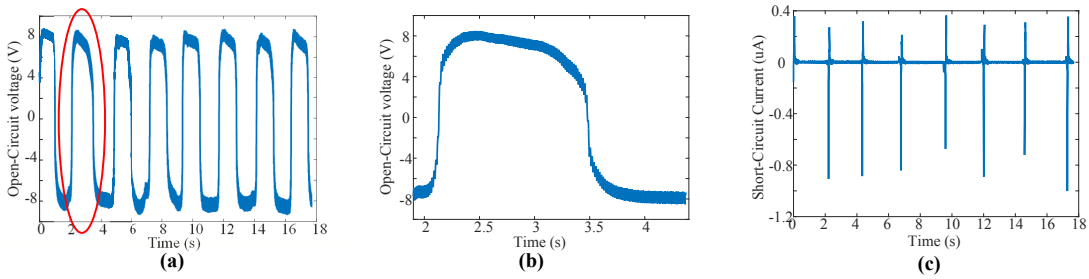

Figure 4.5: The open-circuit voltage (a) and short-circuit current (c) of the triboelectric energy harvester (PTFE and copper, pressing model). (b) is the enlarged figure of the green rectangle in (a).

was first conducted in the study to investigate the triboelectric property of flexible textile materials including cotton, polyester, paper, and foam. In the experiment, we prepared the samples of each material and slid them on the same copper substrate. A surface charge measurement device (USSVM2, AlphaLab Inc.) was used to detect the surface voltage after each sliding. The charge accumulation can be clearly observed from the experiment that the surface voltage significantly increased with the sliding times. In the first experiment, we slid the four samples with the copper substrate for five times and measured the surface voltage before and after sliding for all the four samples. For each sample, we tested at least five times. The average surface voltages caused by the generated triboelectric charges before and after sliding five times are listed in Table 4.1. Foam shows the highest charge generation capability when sliding with the conductive copper substrate, which is much higher than other materials. Then, we selected foam and measured the change generation of foam with sliding times. The surface voltage is almost linear with sliding times as shown in Fig. 4.6. Although the exact value of the detected surface voltage varies, this result is

repeatable in a certain range.

Table 4.1
Surface voltage caused by triboelectric charge before and after sliding five times

Material		Before Test (V)		After Test (V)	
A	B	A	B	A	B
Polyster	Copper	98.9	112.2	51.5	125.0
Paper	Copper	130.3	113.2	539.5	-13.6
Cotton	Copper	124.9	116.3	355.3	169.0
Foam	Copper	123.6	137.9	-2725.6	201.6

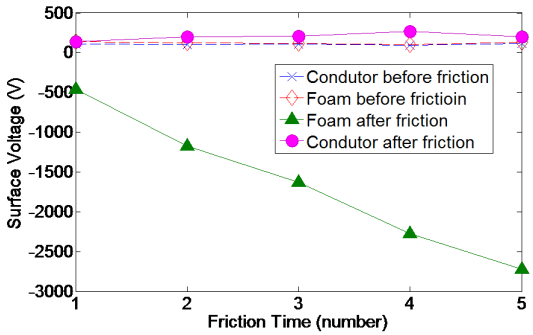

Figure 4.6: Triboelectric property of foam.

In order to visualize the performance of WearETE, a great number of LEDs were used to connect to the energy harvester as shown in Fig. 4.7. In the experiment, two WearETE (99 cm^2 and 1421 cm^2) were adopted to lighten 52 and 190 LEDs successfully, which have been shown in Fig. 4.8.

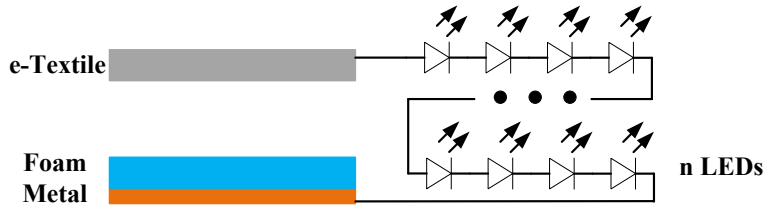

Figure 4.7: The Power Management Circuit for Powering a LED series.

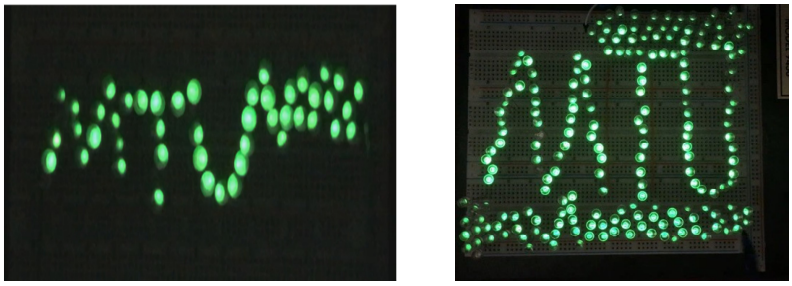

(a) **(b)**

Figure 4.8: (a) A single TEH powers 52 MTU LEDs at each pulse. (b) A larger version of TEH can power 190 LEDs.

4.4.2 Energy Harvester Performance

The WearETE system including the rectifier can harvest human motion to DC for powering purpose. Due to the irregular feature of human motion, it is challenging to control the input power as the same for all performed tests. In the experiment, we calibrate the system performance under different human motion conditions, which is similar to previous human motion energy harvester studies [27, 28]. The energy harvesting in contact-separation motion mode is first validated. For energy harvesting,

the capacitor and the exciting frequency govern the harvested energy. The capacitance generally influences the charging time constant and the output voltage. Thus, different capacitors under different frequencies are tested to calculate the power that the WearETE system can harvest and validate the system performance. The smaller the capacitance, the smaller the time constant, the faster it is charged or discharged, and vice versa. The frequencies are chosen based on the nature of human motion which is less than 5 Hz. The power generated by WearETE during contact-separation mode can be calculated by Eq. (4.4). The input mechanical energy is measured and calculated using the platform presented in Section 3.1. Then the energy efficiency is calculated by Eq. (4.11).

In the experiment, the accelerometer and the force sensor were precisely aligned to the backside of the WearETE during calibration, aiming to protect the triboelectric materials (e-texture, foam) from the impact caused by accelerometer and force sensor thin film. To acquire comparable results under different frequencies, the two substrates of the triboelectric energy harvester were pressed under repeated movement, which was validated using the force sensor. Under the stable tapping frequency, the output voltage of the WearETE system is periodic.

The typically measured output voltage of the WearETE system along with the calibration sensor data during contact-separation motion is shown in Fig. 4.2. In this case, the motion frequency is 2 Hz. The results, in this case, show that the output

peak voltage of the WearETE system with an area of 10.16 10.16 cm^2 through contacting (first peak) and separation (second peak) are approximately 70 V and 4.5 V, respectively.

In order to estimate the system performance of the WearETE during motion, a number of capacitors with different values, i.e., 0.22, 2.2, 4.7, 10, and 47 μF, are selected to test for charging under different frequencies, i.e., 1, 2, 3 and 4 Hz. The voltage through the capacitors during charging by WearETE system under 4 Hz are illustrated in Fig. 4.9. The capacitor of 0.22 μF increases to 1 V most fast but it oscillates most dramatically. The capacitor of 47 μF increases slowly but more stable and discharges slowly as well. The results show that the voltage of the capacitors with larger capacitance increases slower and more stable, and vice versa. The output voltage of the capacitor of 47 μF during charging under different frequencies are shown in Fig. 4.10. The results show that the voltage of this large capacitor can be charged to 1 V in 100 seconds, which demonstrates the possibility in practical application. When the motion frequency is stable, the capacitor can be charged up to a stable value if the charging time is long enough.

In addition, the power efficiency for charging different capacitors with different frequencies was also investigated in order to provide the estimation of the power generation due to frequencies of human motion and influence of the storage capacitors in the AC-DC process for entire energy harvesting system design. Figure 4.11 is to

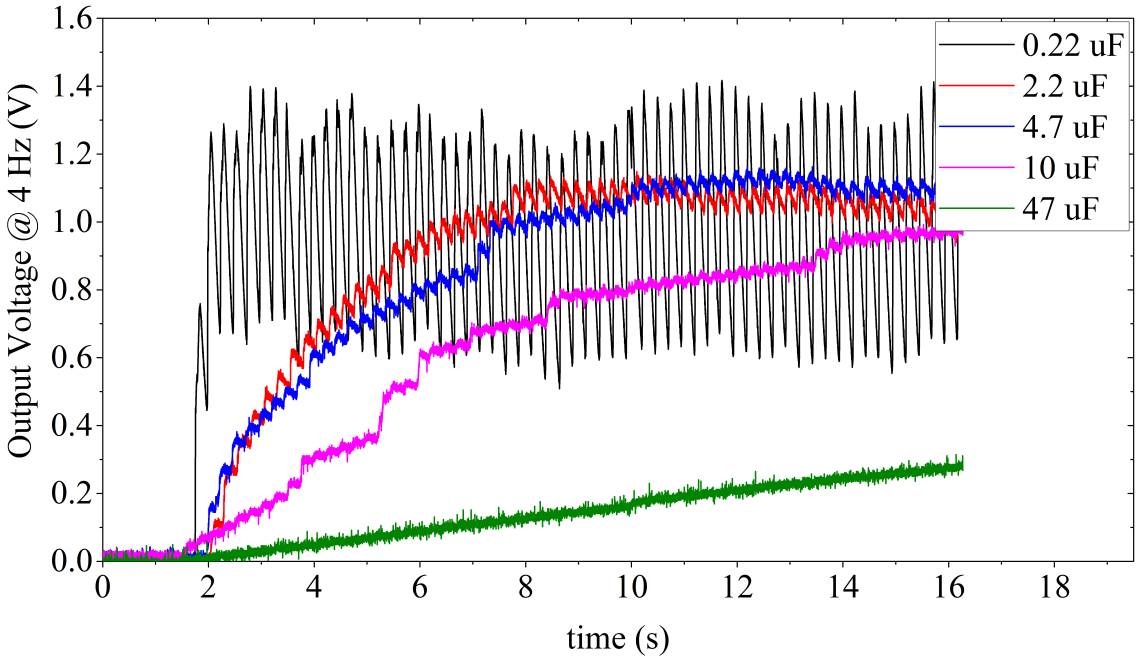

Figure 4.9: Charging different capacitors (0.22, 2.2, 4.7, 10 and 47 μF) by TEH under hand-clapping with 4Hz frequency.

show how the output power will change with different input frequency due to human motion, which will provide an estimation of the power generation due to frequencies of human motion. Figure **??** is to show how the power efficiency changes with load capacitance for storage and input frequency in order to provide a suggestion of selecting capacitance in the system design. The results show that higher load capacitance and input frequency generally cause higher output power. The results of charging the 47 μF capacitor under different motion frequencies are listed in Table 4.2. The input power is calibrated using the presented platform. In each experimental settings, i.e. different capacitances and frequencies, more than five sets of output voltage data were measured. These data show that the input power in different experiments is

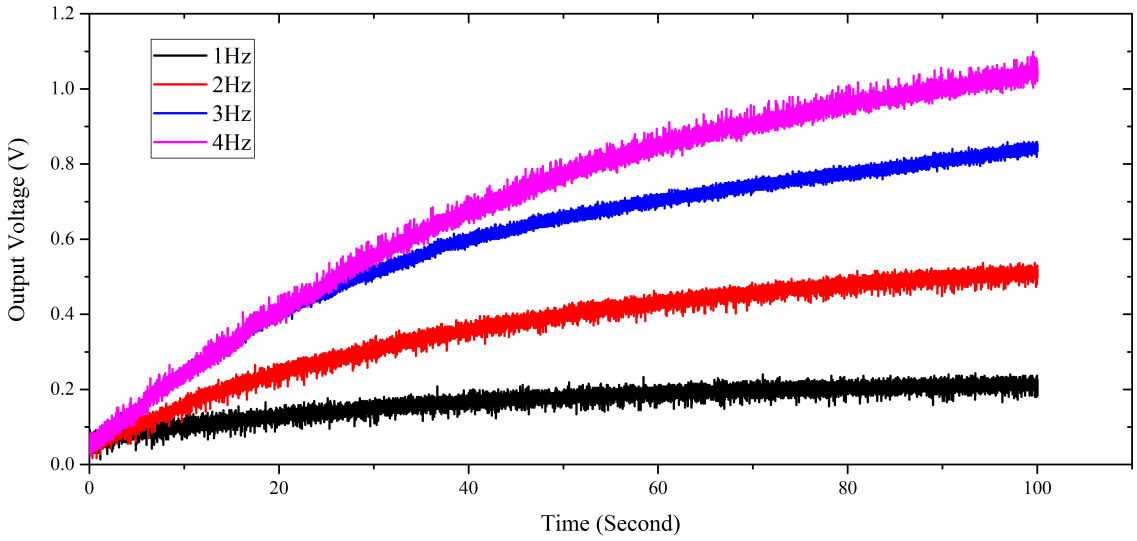

Figure 4.10: Charging 47uF capacitor by TEH under hand-clapping with different frequencies (1.0, 2.0, 3.0 and 4.0 Hz).

dispersed and varied in the range from 0.1 W to 1 W due to the irregular nature of human motion. Under the same experiment settings with a similar level of force measured by the force sensor, the output power of larger capacitance or frequency during motion are much higher. It indicates that for charging a capacitor, higher frequency means harvesting more energy in the same time interval. The conclusion is also applicable for charging a capacitor with higher capacitance. These trends are illustrated in Fig. 4.11. The output power increases with the capacitance as well as the input mechanical frequency, which can provide guidance in practical applications. Also, in the experiment, the power efficiency increased within 3 Hz; whereas the efficiency at 3 Hz is higher than that at 4 Hz due to the difference of the input power in these two cases. For charging a 47 μF capacitor, the power efficiency of average input and output power can be as high as 24.94%.

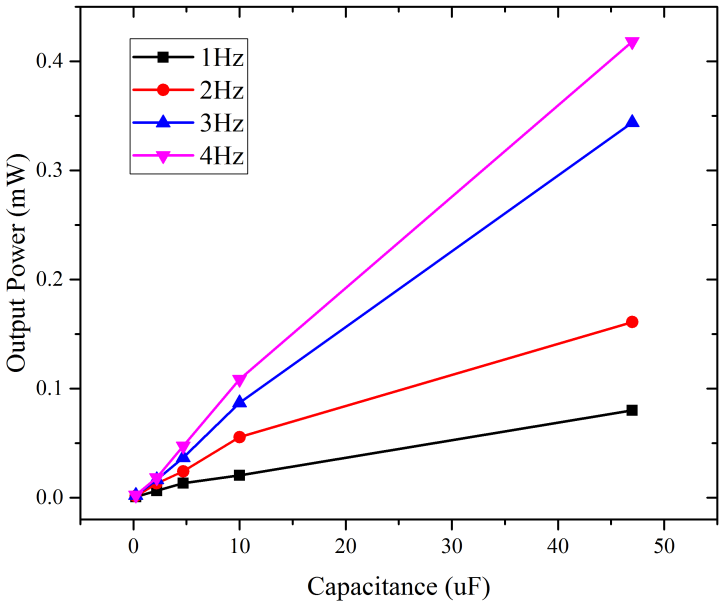

Figure 4.11: Harvested energy during charging different capacitors with different frequencies from hand-clapping motion.

Table 4.2
Average results of charging a 47 μF capacitor under hand clapping movements with different frequencies

Frequency (Hz)	**Input Power** (mW)	**Output Power** (mW)	**Efficiency** (%)
1.0	3.6460	0.0802	2.1996
2.0	1.5351	0.1611	10.4918
3.0	1.3790	0.3439	24.9374
4.0	2.5519	0.4182	16.3891

In addition to the average results, Table 4.3 summarizes the maximum power generated in these experimental settings with the capacitance of 0.22, 2.2, 4.7, 10, 47 μF under the frequency 1-4 Hz. From the experiment results, charging a 47 μF capacitor

Table 4.3
Maximum output power of charging different capacitors under hand clapping movements under different frequencies.

Maximum Power (mW)	1 Hz	2 Hz	3 Hz	4 Hz
0.22 μF	0.0222	0.0220	0.0265	0.0542
2.20 μF	0.0725	0.1182	0.1093	0.1700
4.70 μF	0.1656	0.1974	0.2402	0.4299
10.0 μF	0.1883	0.5115	0.5608	0.8986
47.0 μF	0.8288	1.6001	2.5916	4.8113

can harvest the highest maximum power, which is approximately 4.8113 mW, from the 4 Hz motion. The WearETE used in experiments has a size of 10.16 $\times$ 10.16 cm^2, which equals to 103.226 cm^2. The approximate area power density is approximately 46.6 μ W/cm^2.

In the experiment, we found that the power loss caused by the bridge rectifier was high. In this study, since we focus on proposing and validating the proof-of-concept using low-cost materials and manufacturing method for power generation for wearable electronics, we will consider the power conditioning circuit design in Chapter 5.

4.4.3 Harvesting Energy from Walking

During walking, people generally swing their hands to keep balance. Since the proposed WearETE system can generate power from sliding motion, a validation experiment was developed to harvest energy from people swinging their hands during

walking. In the experiment, the two substrates of the WearETE were attached to the cloth on the side of the body and front arm individually. Then the energy harvester was assembled with the power management circuit. The output voltage of the WearETE system is measured and recorded during walking. The power harvested during human walking is generated by sliding the two tribomaterials of the energy harvester. Finally, the output power is calculated based on the output voltage.

The output of the WearETE system for harvesting energy from walking is shown in Fig. 4.12. The output power harvested by WearETE during walking is 7.5248 μW. The results show the possibility of harvesting energy during human walking. Compared to other similar systems with energy harvester attached to the cloth [141], the WearETE system provides reasonable performance for human motion energy harvesting. In this study, we demonstrate the feasibility of using very low-cost materials and fabrication methods for human motion harvesting.

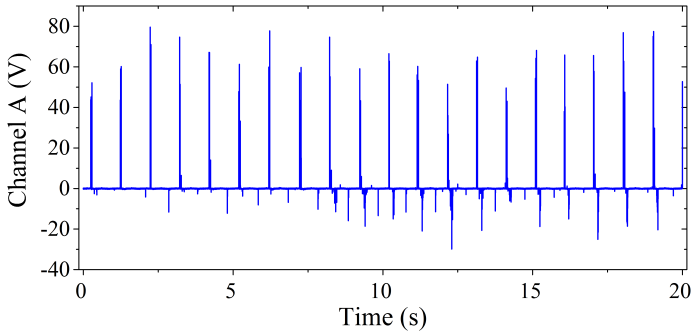

Figure 4.12: Output voltage of WearETE during harvesting energy from human walking.

4.5 Conclusion

In this chapter, a TEH has been developed for harvesting energy from human motion. The mechanism of the triboelectric energy harvester has been theoretically investigated. The optimized power generation from the TEH has been also estimated for the hand tapping model. The performance of the proposed TEH has been evaluated by charging different capacitors with different tapping frequency. The experimental results also show that the proposed TEH is suitable for harvesting a reasonable amount of energy from human walking. The proposed TEH will be applied to provide continuous power supply associated with the chargeable battery for long-term biopotential monitoring.

Chapter 5

Power Management for Triboelectric Energy Harvester

In this chapter, a synchronized switching harvesting on inductor (SSHI) based rectifier for triboelectric energy harvesting is reported for the first time. In recent few years, triboelectric energy harvesters (TEHs), also called triboelectric nanogenerators (TENGs) are emerging and extensively studied, which provide promising solutions for converting mechanical energy to electricity as power resources for electronics. To practically power electronics from TENGs, power management module with high energy efficiency is also essential. The current studies of power management circuits for triboelectric energy harvesting in the existing literature are mainly focused on increasing dc-dc power efficiency; few have been attempted for AC-DC stage yet. In

this section, we report an SSHI rectifying strategy associated with TEH design and provide a new perspective of designing TEHs or TENGs by considering their capacitance concurrently. A new theoretical model is developed for electricity generation from triboelectric energy harvesting considering the introduced pairing capacitance and the impact force in practical condition. We also demonstrate that ultra-low-cost, easy-fabricated TEHs can also generate a reasonable amount of power. The experimental results show that the proposed SSHI rectifier increases the harvested power by 242.83% when compared with that with a full-wave bridge rectifier from a newly designed low-cost TEH. The proposed new SSHI interface provides a promising strategy of rectifier design in the AC-DC stage for triboelectric energy harvesting.

5.1 Introduction

Since firstly introduced in 2012 [19], triboelectric energy harvesters (TEHs), namely triboelectric nanogenerators (TENGs) have been studied extensively in recent years. A great number of promising TENGs have been reported, which have shown great potential for providing sustainable power resources for electronics [142][133][21][143][144]. The energy conversion in TENGs is based on the mechanism of triboelectricity or contact electricity by which surface charge is generated from contact and separation or sliding between two materials. The generated charge fluctuates periodically with the input vibration, which thus can convert mechanical

energy to electrical energy. Previously we also proved that instead of using nanomaterials and nanoscale fabrication as TENGs, low-cost materials and manufacturing techniques can also achieve reasonable results by triboelectric energy harvesting [143]. Thus, we use TEHs throughout the section for all types of triboelectric energy harvesting devices. The proposed rectifying strategy in this study is universal for all TEHs.

In this study, we develop a new rectifier for TEHs based on synchronized switching harvesting on inductor (SSHI) technique. SSHI rectifiers have been studied for piezoelectric energy harvesting and can enhance the harvested power and energy efficiency for piezoelectric energy harvesters comparing with bridge rectifiers [145][146][147]. The SSHI interfaces introduce an optimal switching to reduce the energy dissipation and ensure the energy flowing from the mechanical part to the electrical circuit. However, the highly changeable inner capacitance of TEHs leads to difficulty of achieving optimal synchronized switching time for the LC loop composed of the added inductor and the inner capacitance of the harvester, which is one of the keys for successful SSHI interfacing with harvesters. This issue thus brings challenges for designing SSHI rectifiers for TEHs.

In this section, we propose an SSHI rectifying strategy for triboelectric energy harvesting and provide a new perspective of designing TEHs with the consideration of their inner capacitance concurrently. To the best of our knowledge, the proposed

SSHI rectifier associated with the TEH design in this section is among the first that provides a new AC-DC design for triboelectric energy harvesting and considers the capacitance in TEH design as well. The proposed TEH pairs a multilayer structure to the changeable part for converting mechanical input to achieve the capacitance which ensures that the equivalent source capacitance (i.e., inner capacitance) of the TEH controllable for designing the SSHI interface. We also develop a new theoretical model considering the source capacitance and the impact force to better understand the energy conversion in practical conditions and guide the TEH design.

5.2 Triboelectric Energy Harvesters

5.2.1 Proposed Multilayer Triboelectric Energy Harvester

Using different triboelectric materials generates a different amount of triboelectric charge basically following the triboelectric series. In our previous experiment [143], foam shows the high capability of charge generation and linear relationship with external work. The results showed that the surface voltage on the foam layer significantly increases linearly with sliding times as shown in Fig. 4.6. It is also ultra-low cost, highly accessible, flexible, and safe for various applications. E-textile is a wearable conductive material and often used for developing wearable sensors and systems. In

this study, we also choose foam and e-textile as triboelectric materials. It shows that low-cost materials and easy-assembly can also achieve reasonable results for triboelectric energy harvesting.

Besides the material, contact is also a critical factor for the charge generation. A multilayer-structure can significantly improve the contact area with the same overall size. It can also ensure a controllable capacitance of the TEH which is a key to the SSHI design. Thus, we use the multilayer-structure to achieve a pairing capacitor in our TEH design. The design and analysis are illustrated in details as follows.

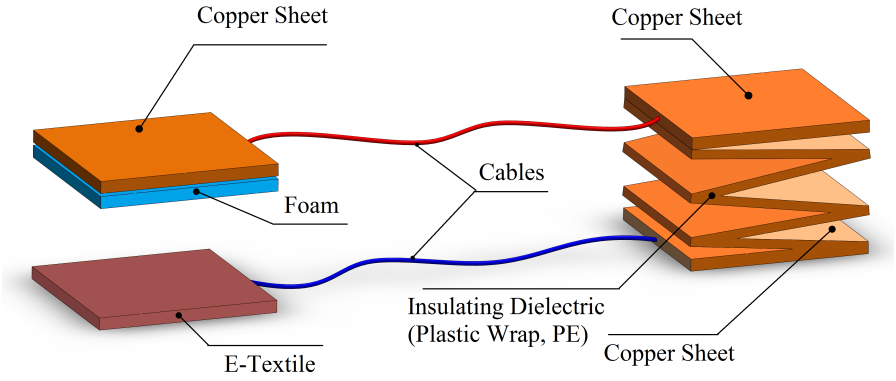

Figure 5.1: The structure of the proposed triboelectric energy harvester.

The proposed TEH with a multilayer-structure design is shown in Fig. 5.1. On the left side, a basic structure is to keep the contact separation process, while a pairing capacitor with a multilayer structure is shown on the right in Fig. 5.1. The pairing capacitor is multi-folded to a sandwich-like three-layer plate that consists of two copper sheets as the outer layers and a thin polyethylene (PE) layer in between.

The PE layer is used as the insulating dielectric and has an approximate thickness of 12.5 μm, which is proper for designing a pairing capacitor with a relatively large capacitance.

The multilayer pairing capacitor is controllable and will stabilize the source capacitance for further SSHI design. The original TEH without the pairing capacitor has a changeable capacitance C_{tribo} which is the series capacitance of the air layer and the foam layer, $\frac{1}{C_{tribo}} = \frac{x(t)}{\varepsilon_0 A} + \frac{1}{C_{Foam}}$, where $x(t)$ is the separation distance between the triboelectric material layers, A is the effective contact area, ε_0 is the permittivity of air, and C_{Foam} is the capacitance of the foam layer. This capacitance, C_{tribo}, is actually highly variable due to the relatively wide range of separation distance, $x(t)$, varying in a range from 100 μm to 10 mm in this case. The capacitance C_{Foam} also changes with its thickness in the mechanical process. The highly changeable source capacitance C_{tribo} brings difficulties in designing an SSHI rectifier interfacing with TEHs as the source capacitance of harvesters is critical for designing the synchronized switching.

When parallel with the pairing capacitor, C_{pair}, which has a relatively large capacitance resulted from the multilayer structure, the inner capacitance of the harvester can be stabilized in a controllable range. In this study, the total capacitance of the proposed TEH, C_T, can be calculated by $C_T = C_{tribo} + C_{pair}$. Here, C_{tribo} represents the capacitance of the basic TEH structure for the distinguishable purpose. By

adding the pairing capacitance, the total capacitance of the TEH can only vary by up to 30.03%, which stabilized the C_T for the rectifier design. This multilayer TEH will be then used in our proposed SSHI design.

5.2.2 New Model for Triboelectric Energy Harvesting

To further understand triboelectric energy harvesting and guide rectifier design interfacing with TEHs, we first develop a new model considering the source capacitance and the impact force in the dynamic process. Some remarkable studies are already carried out to investigate the theoretical model of triboelectric energy harvesting [148][149][96][144][150]. In practical applications of TENGs, the dynamic mechanical input often generates periodic contact and separation or sliding and therefore generates charges for powering electronics. In the dynamic process of contact and separation, there is an obvious impact force between the two parts of TENGs in most cases due to the fast contact and separation process. However, this impact force is seldom considered in existing models. In this section, the new theoretical model for triboelectric energy harvesting is shown in details.

In existing models, a well-accepted theoretical voltage-charge-distance ($V-Q-x$) relationship [148] has been given in Eq. (5.1) to model the TENG voltage in the contact-separation mode of triboelectric energy harvesting, which also aligns with

our previous equivalent circuit model [151],

$$V = -\frac{Q}{A\varepsilon_0}\left(\frac{d_{Foam}}{\varepsilon_{Foam}} + x(t)\right) + \frac{\sigma x(t)}{\varepsilon_0} \tag{5.1}$$

where V is the generated voltage across TEHs, Q is the amount of transferred charge between the two electrodes, d_{Foam} and ε_{Foam} represent the thickness and relative dielectric constant of the foam layer, σ is the generated surface charge density, and thus $Q_0 = \sigma A$ is the generated amount of charge.

For triboelectric energy harvesting, the contact force has been proved as a critical factor that affects charge generation. Equation (5.2) shows the relationship between triboelectric charge and contact force [150]:

$$\sigma A = \left(\frac{F}{E'}\sqrt{\frac{\pi}{m_2}}\right)\frac{\varphi_{Foam}\varepsilon_0}{3ex(t)} \tag{5.2}$$

where F is the contact force, E' is the equivalent elastic modulus, m_2 is the Root Mean Square (RMS) slope which is a statistical surface parameter and is a constant for a given triboelectric material, φ_{Foam} is the effective or surface work functions of the foam layer, e is the elementary charge which equals to the electric charge carried by a single proton. This equation reveals that the triboelectric charge generation is

proportionally affected by the applied contact force.

During continuous dynamic contact and separation cycles in most practical conditions, the contact force in each period is not static due to the fast contact. It is actually an impact force in each contact cycle caused by the dynamic process. This impact force can be calculated by equivalent static force which is the static force multiplied by the actual impact factor as shown in Eq. (5.3):

$$F_e = F\left(1 + \sqrt{1 + \frac{\dot{x}(t)^2}{g\delta_{st}}}\right) \tag{5.3}$$

where δ_{st} is the static deflection, $\dot{x}$ is the velocity, F is the contact force in static condition whereas $\left(1 + \sqrt{1 + \frac{\dot{x}(t)^2}{g\delta_{st}}}\right)$ is the impact factor.

Combining Eq. (5.1) - Eq. (5.3), we can obtain the nonlinear relationship of the voltage with the separation distance and the impact force as represented in Eq. (5.4). In the real harvesting system, there is always a load resistance R_L, and $V = IR_L$, where $I = dQ/dt$ is the current through the load resistance caused by the transferred charge. Thus, we can derive Eq. (5.5) from Eq. (5.4).

$$V = -\frac{Q}{A\varepsilon_0}\left(\frac{d_{Foam}}{\varepsilon_{Foam}} + x(t)\right) + \frac{F\varphi_{Foam}}{3eAE'}\sqrt{\frac{\pi}{m_2}}\left(1 + \sqrt{1 + \frac{\dot{x}(t)^2}{g\delta_{st}}}\right) \tag{5.4}$$

$$R_L\frac{dQ}{dt}=-\frac{Q}{A\varepsilon_0}\left(\frac{d_{Foam}}{\varepsilon_{Foam}}+x(t)\right)+\frac{F\varphi_{Foam}}{3eAE'}\sqrt{\frac{\pi}{m_2}}\left(1+\sqrt{1+\frac{\dot{x}(t)^2}{g\delta_{st}}}\right) \tag{5.5}$$

By solving Eq. (5.5), the voltage through TEHs, V, has the analytical solution as Eq. (5.6).

$$\begin{aligned}V(t)=&-\frac{F\varphi_{Foam}}{3eAE'}\sqrt{\frac{\pi}{m_2}}\left(1+\sqrt{1+\frac{\dot{x}(t)^2}{g\delta_{st}}}\right)-\frac{\frac{d_{Foam}}{\varepsilon_{Foam}}+x(t)}{A\varepsilon_0}e^{-\int_0^t\frac{\frac{d_{Foam}}{\varepsilon_{Foam}}+x(\tau)}{A\varepsilon_0R_L}d\tau}\times\\&\int_0^\tau\left(\frac{F\varphi_{Foam}}{3eAE'}\sqrt{\frac{\pi}{m_2}}\left(1+\sqrt{1+\frac{\dot{x}(t)^2}{g\delta_{st}}}\right)\right)e^{\int_0^\tau\frac{\frac{d_{Foam}}{\varepsilon_{Foam}}+x(z)}{A\varepsilon_0R_L}dz}d\tau\end{aligned} \tag{5.6}$$

From Eq. (5.6), once the structure of TEHs is fixed, the impact force F_e dominates the output voltage as shown in the simulation.

Next, we need to further consider the pairing capacitance. When adding the pairing capacitance,C_{pair}, the output voltage of the TEH can be derived from Eq. (5.4) and represented as Eq. (5.7). The difference between Eq. (5.7) and Eq. (5.4) indicates the influence of the pairing capacitance for triboelectric energy harvesting. Using the same method as Eq. (5.4) - Eq. (5.6), we can have an analytical solution of voltage generation considering pairing capacitance as Eq. (5.8).

$$V = -\frac{Q\left(d_{Foam} + \varepsilon_{Foam}x(t)\right)}{A\varepsilon_0\varepsilon_{Foam} + C_{pair}\left(d_{Foam} + \varepsilon_{Foam}x(t)\right)} + \frac{F\varphi_{Foam}}{3eAE'}\sqrt{\frac{\pi}{m_2}}\left(1 + \sqrt{1 + \frac{\dot{x}(t)^2}{g\delta_{st}}}\right) \tag{5.7}$$

$$\begin{aligned} V(t) = &-\frac{F\varphi_{Foam}}{3eAE'}\sqrt{\frac{\pi}{m_2}}\left(1 + \sqrt{1 + \frac{\dot{x}(t)^2}{g\delta_{st}}}\right) - \frac{d_{Foam} + \varepsilon_{Foam}x(t)}{A\varepsilon_0\varepsilon_{Foam} + C_{pair}\left(d_{Foam} + \varepsilon_{Foam}x(t)\right)} \\ &\times e^{-\int_0^t \frac{d_{Foam}+\varepsilon_{Foam}x(\tau)}{R_L\left(A\varepsilon_0\varepsilon_{Foam}+C_{pair}\left(d_{Foam}+\varepsilon_{Foam}x(\tau)\right)\right)}d\tau} \times \\ &\int_0^t \left(\frac{F\varphi_{Foam}}{3eAE'}\sqrt{\frac{\pi}{m_2}}\left(1 + \sqrt{1 + \frac{\dot{x}(\tau)^2}{g\delta_{st}}}\right)\right) e^{\int_0^\tau \frac{d_{Foam}+\varepsilon_{Foam}x(z)}{R_L\left(A\varepsilon_0\varepsilon_{Foam}+C_{pair}\left(d_{Foam}+\varepsilon_{Foam}x(z)\right)\right)}dz} d\tau \end{aligned} \tag{5.8}$$

With this new model, we can quantitatively analyze the contributing factors and understand their contribution to the output voltage of TEHs. This new model will then be used as the guideline for identifying the typical waveforms of TEHs. From Eq. (5.6) and Eq. (5.8), the output voltage of the TEH is determined by different contributing parameters mainly including the dynamic contact force in practical condition and the proposed pairing capacitance. The influences of these two contributing factors are clear as shown in Fig. 5.2 (a) and (b), which is the numerical analysis conducted using MATLAB. The theoretical output voltage is plotted. With the change of the impact factor (i.e., the impact force), the output voltage changes not only its amplitude but also the waveform. The impact factor causes the frequency shift of the voltage output. The pairing capacitance mainly affects the amplitude of the output

voltage theoretically. The detailed simulation and experimental validation and the results will be presented in Sections 5.4.2 and 5.4.3 theoretically. With the validation, this model will further be used to design the SSHI interface as identifying peaks of the TEH output voltage and source capacitance of harvesters is the key in the SSHI design. The model quantitatively shows the typical waveform and the effect of the pairing capacitance.

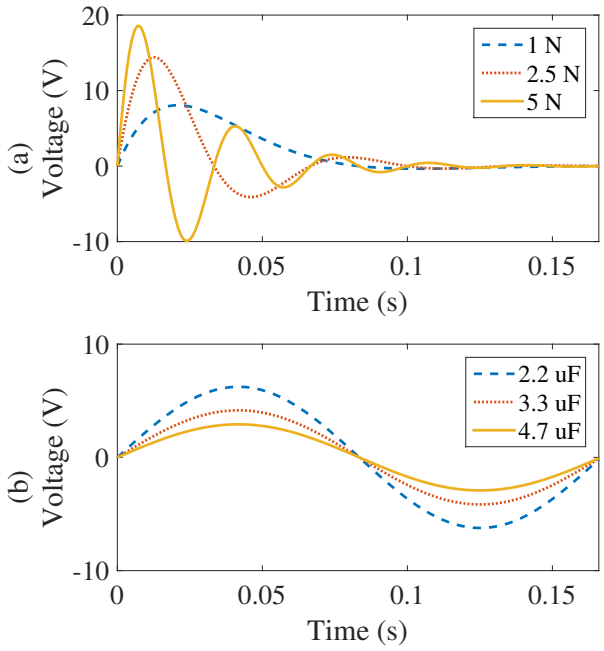

Figure 5.2: Theoretical solution of output voltage of TEHs in one cycle. Effects of changing (a) the impact force and (b) the pairing capacitor on the voltage output of TEHs.

5.3 Proposed SSHI Rectifier

5.3.1 Proposed SSHI Circuit

Bridge rectifiers are simple and effective for AC-DC conversion for most mechanical energy harvesters. This type of rectifiers, however, cannot ensure the energy flow direction during certain intervals in each cycle, which may result in energy returns from the electrical part to the mechanical part [152]. SSHI rectifiers interfacing with harvesters is capable of overcoming this energy-returning problem in piezoelectric energy harvesting by introducing an inductive switch path in which an inductor and a switching component are added either in parallel or in series to the bridge rectifier. According to whether parallel or series, SSHI rectifiers can be divided into two categories, p-SSHI, and s-SSHI. Both have been successfully implemented for piezoelectric energy harvesting with a variety of existing studies [153][154][155][156][157][158][159][160]. SSHI rectifiers minimize the energy dissipation on the source capacitance of harvesters by controlling the optimal timing of switching approaches to match the LC loop formed by the added inductor and the source capacitance. By using these SSHI rectifiers, piezoelectric energy harvesting systems can achieve higher energy efficiency for mechanical energy conversion.

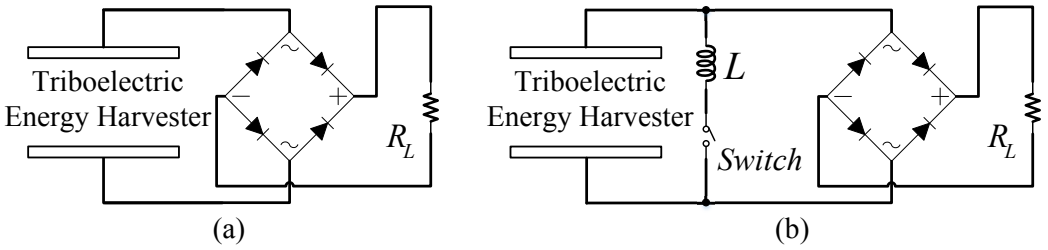

Figure 5.3: Equivalent circuits for managing power of TEHs: (a) A full-wave bridge rectifier; (b) adding an SSHI interface.

In this study, we successfully develop an SSHI rectifier for triboelectric energy harvesting. Comparing to simply using the conventional bridge rectifier as illustrated in Fig. 5.3 (a), we develop a p-SSHI rectifier interfacing with the TEHs as the power management circuit. The equivalent circuit model is shown in Fig. 5.3 (b). Figure 5.4 illustrates the detailed circuit of the proposed SSHI interface. Previously we proposed an equivalent circuit model for TEHs in which a current source $d\Delta Q/dt$ is in parallel to the changeable air layer C_{air} and then in series to other layers, such as C_{Foam} in this case. This is because when capacitors are connected in series, each of them stores an instantaneous charge equal to each other. As described in Section 5.2.1, the original TEH is then parallel to the pairing capacitor C_{pair}. In Fig. 5.4, R_T is the inner resistance of the TEH which is negligible in this case. The dash line circles equivalent circuit model of our TEH with consideration of the source capacitance design. i_T is the output current of the overall TEH. When using a bridge rectifier, this output current will charge the source capacitance of the harvester first before it can flow to the output in every half cycle. The proposed p-SSHI interface circuit contains an inductor and a switch in parallel to the TEH. The switching circuit, in

this case, consists of a pair of n-MOSFETs in a symmetric structure which ensures the switching process working properly for both positive and negative peaks. The MOSFETs are low energy consumption during switching. The interface circuit then connects to a bridge rectifier. R_L is the load.

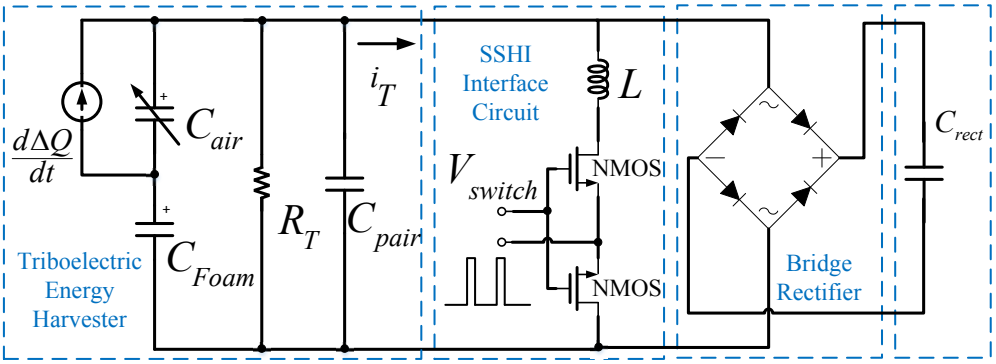

Figure 5.4: Proposed SSHI interface circuit.

5.3.2 The Operation

In the contact-separation mode of triboelectric energy harvesting, the charge is generated when the two TEH plates contact each other and then redistributed when the separation distance increases. In the analysis, we assume one plate is fixed whereas the other is movable to achieve contact and separation. Thus we also use displacement for separation distance.

Due to the periodic contact and separation between the plates with a sinusoidal separation distance as shown in Fig. 5.5 (a), the TEH output voltage with or without

the SSHI interface are periodic as well with the same period. In the displacement plot in Fig. 5.5 (a), the negative peaks refer to the contact point of the two plates whereas the positive peaks refer to the maximum separation distance. In the experiment, an accelerometer is attached is the fixed plate to monitor the effect of the impact force. The signal from the accelerometer is shown in Fig. 5.5 (b). The output voltage is affected by the impact force and the following interfacing circuit, which shows high nonlinearity from the displacement input. This is different from the other three types of mechanical energy harvesting.

Here we use one single period from t_0 to t_3 as marked in Fig. 5.5 (d) to analyze the operation of the TEH first. In each cycle of the input sinusoidal movement, the two layers start to physically contact with each other before the displacement reaches its minimum due to the thickness of the foam layer. This contacting time point is defined as t_0. Before t_{0-}, the two TEH plates are separated and the movable plate moves towards the fixed plate. After t_{0+}, the movable plate continues moving till the displacement reaches its minimum that the foam layer is compressed till the minimum thickness as the negative peaks in Fig. 5.5 (a). When the two places physically contact, the impact force occurs and a pulse is generated from the accelerometer as shown in Fig. 5.5 (b). During the physical contact, due to the triboelectric effect, the charge is generated on the contacting surfaces of the two triboelectric material layers. In this study and other theoretical analyses for triboelectric energy harvesting, the charge is assumed to be evenly distributed with a surface charge density σ. Then the

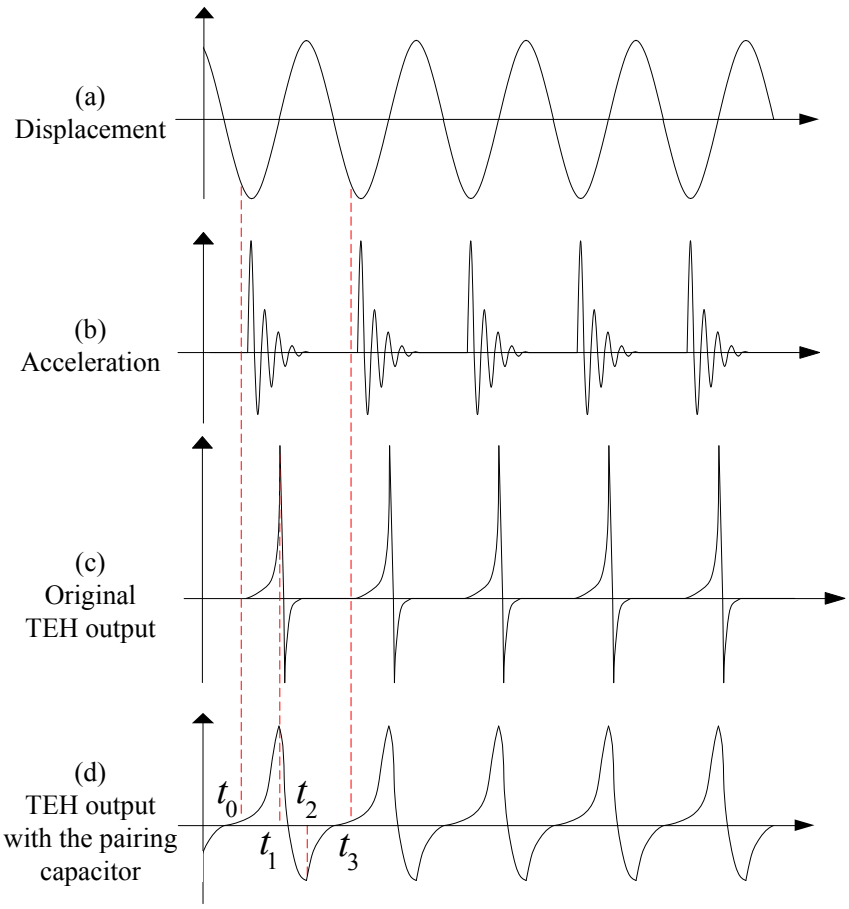

Figure 5.5: Typical waveforms of TEHs. (a) Displacement; (b) accelerometer signal; (c) TEH voltage with changeable capacitance; (d) TEH voltage with pairing capacitance.

movable plate changes its moving direction and the two layers begin the separation. When the separation physically occurs, the potential difference of the two electrodes emerges and drives the electrons to flow through the external circuit (e.g. a load resistor for oscilloscope). The output voltage (i.e. the voltage through the load resistor) reaches the maximum (positive peaks in Fig. 5.5 (d)) at the time t_1 and then decreases during the separation. After the plates separate from t_1, the potential difference between the two plates decreases with the diminished charge density. The

voltage reaches its minimum at t_2 as the negative peaks in Fig. 5.5 (d). The two plates keep separating and their distance increases till the maximum. The output voltage of the TEH changes from negative to positive at t_3 which is the starting of the next cycle when the two plates start to physically contact again. When there is no pairing capacitor, the charge flow through the external circuit quickly ends, which acts as a high electrical pulse. The movable plate repeats the motion as that from time t_{0+} to time t_{3-} as one cycle. The schematic diagrams of the physical process with the circuitry analysis have been represented in Fig. 5.6. During the entire process, the source current, i_T, in the TEH is shown in Fig. 5.7 (a).

When there is a full-wave bridge rectifier with a smoothing capacitor C_{rect}, the rectifier voltage V_{rect} is ideally dc but with ripples. The ripples are mainly determined by the smoothing capacitance and can be negligible when the capacitance is large. Firstly, we assume that V_{rect} is dc as in the ideal case. In the analysis, we make an assumption that the source capacitance with the added pairing capacitance from the TEH multilayer structure is independent and stable from the mechanical motion. In the operation, the source current i_T needs to charge the harvester capacitance C_T until it reaches $|V_{rect} + 2V_{th}|$ so that the bridge conducts, and then $|V_T| = |V_{rect} + 2V_{th}|$. When i_T changes the direction and $|V_T| < |V_{rect} + 2V_{th}|$ again, the load side and the harvester side are isolated. In triboelectric energy harvesting, the source current i_T can seldom be sinusoidal due to the high nonlinearity between the displacement and

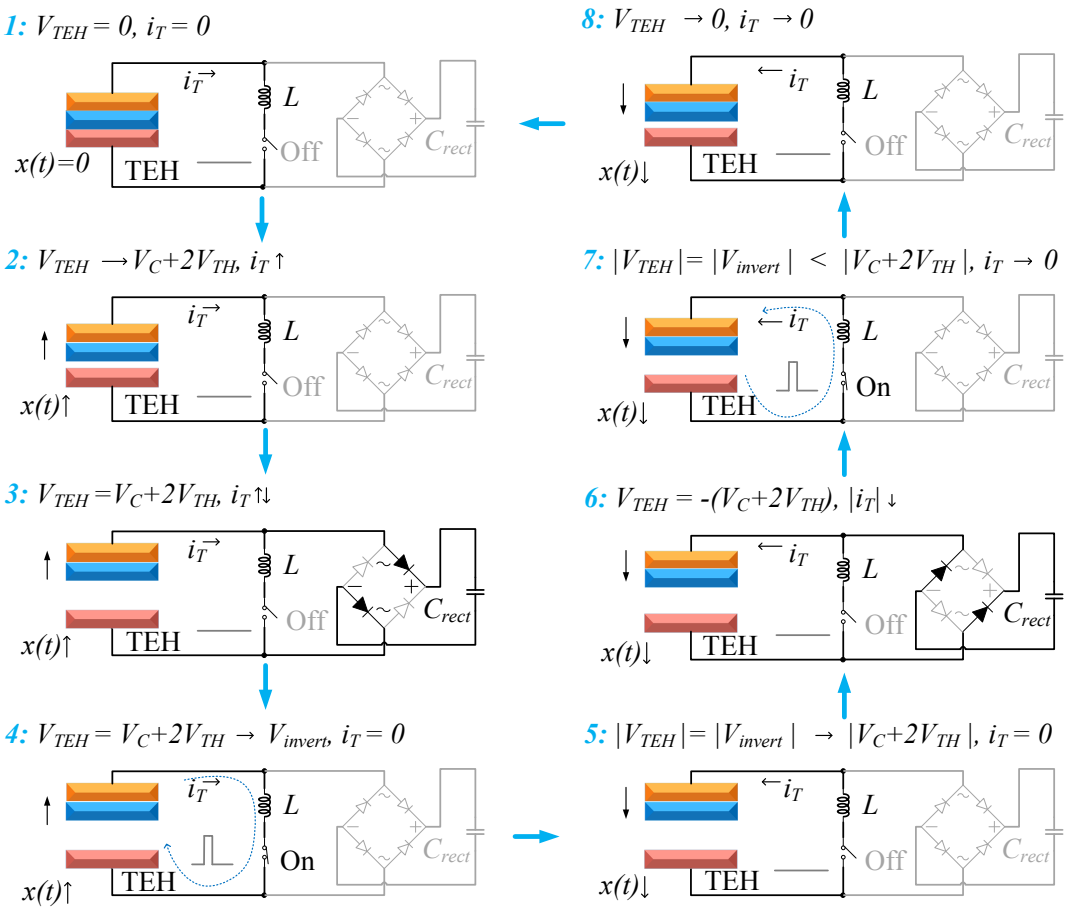

Figure 5.6: The schematic diagrams of the physical process with the circuitry analysis.

the charge generation as analyzed in our model in Section 5.2.2. Also unlike piezoelectric energy harvesting that has a steady current source resulted from continuous mechanical input, the source current i_T in triboelectric energy harvesting not always exists in every cycle as shown in Fig. 5.7 (a). The voltage of the TEH, V_T, either varies following the current i_T or equals to $V_{rect} + 2V_{th}$, depending on whether the bridge conducts. When isolated, the current needs to charge the harvester capacitance C_T until the next bridge conduction. Thus, a considerable amount of energy is

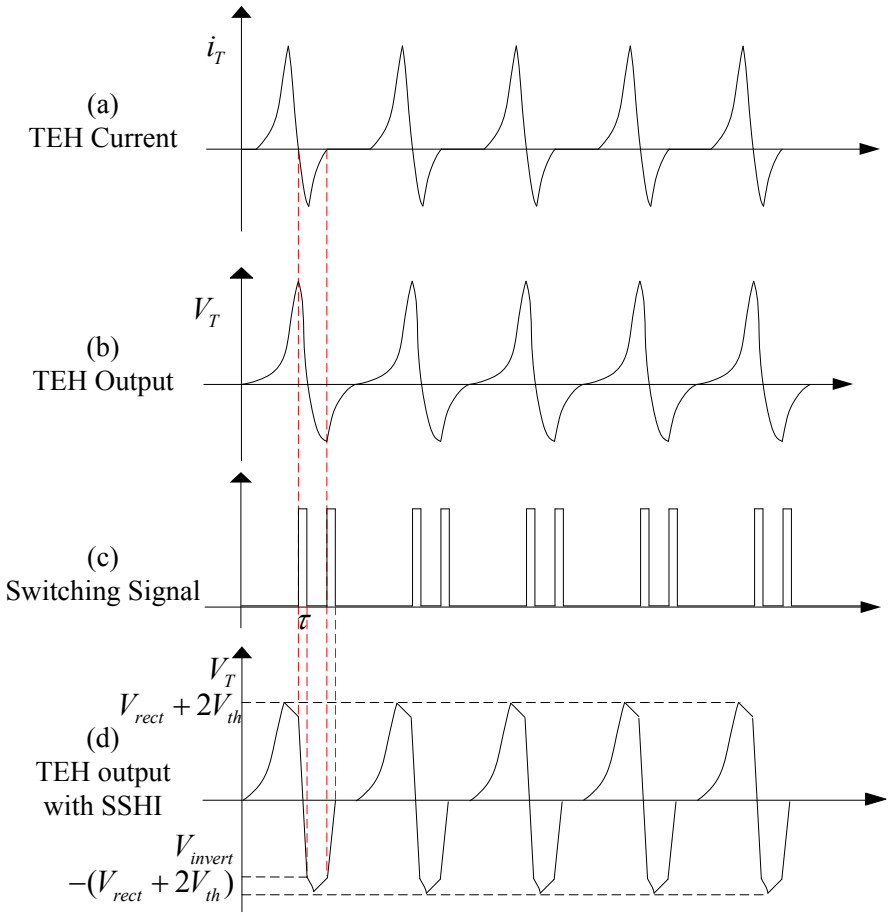

Figure 5.7: Typical waveforms of the SSHI rectifier circuit. (a) The TEH current; (b) the TEH voltage without the SSHI interface; (c) switching signals; (d) the TEH voltage with the SSHI interface.

dissipated on the source capacitance. Also in some conditions of triboelectric energy harvesting, the negative voltage peaks are not high so that they cannot make the bridge conduct, although the positive peaks are mostly high enough. In addition, when considering the ripples of V_{rect} and the short conducting time in each cycle, there may not be a perfect steady duration in the TEH voltage waveform V_T. A typical waveform of the TEH voltage with a bridge rectifier is shown in Fig. 5.7 (b).

When adding an SSHI interface with the optimal switching-on time, the LC resonant loop which consists of the source capacitance of the TEH C_T and the inductor in the SSHI interface L is able to flip the voltage quickly instead of charging the source capacitance at each zero-crossing point of the source current i_T, which reduces the energy return to the harvester and enhances the energy efficiency in the rectifier stage. In the equivalent circuit as Fig. 5.3 (b), the switch in the inductor path is controlled to be closed at each zero-crossing point of the current i_T as shown in Fig. 5.7 (c). At this moment, the current i_T changes its direction, and the switch instantly turns on. The harvester side is an LC resonant circuit and will quickly flip V_T to $-V_{invert}$. So $|V_T|$is lower than the rectifier voltage $|V_{rect}|$ plus $2V_{th}$, and the bridge is not conductive. The current i_T will charge C_T for a short time until $|V_T| = |V_{rect} + 2V_{th}|$. And the bridge will conduct again, and i_T flows to the load side. In triboelectric energy harvesting, the source current i_T does not always exist in one cycle as shown in Fig. 5.7 (a) because the charge transfer may be much faster than the mechanical vibration because the mechanical input is often low frequency (e.g. ¡10 Hz) in a great number of cases when using TEHs or TENGs due to the application scenarios such as human motion, wind-induced motion, etc. Thus the TEH voltage goes to zero in between cycles. Also as mentioned above, the negative voltage peaks are not as high as positive peaks, and the bridge rectifiers sometimes cannot flip the negative peaks as shown in Fig. 5.7 (b) and validation experiment (e.g. Fig. 5.12 (d)). When using LC resonance to flip voltage, the negative peaks can be as high as

positive peaks as shown in Fig. 5.7 (d), which is also validated in the experiment as shown in Fig. 5.12 (e). This will further enhance energy efficiency for triboelectric energy harvesting comparing to adopting bridge rectifiers.

During the operation, the switching process needs to be conducted quickly. The key to success is the timing of the switch. Generally, the time interval of switching-on, τ , is optimized to be half period of the LC loop, which is $\tau = \pi\sqrt{LC_T}$. It is usually only tens or hundreds of microseconds when adopting a small inductance.

5.3.3 Harvested Power Estimation

With the SSHI interface, the energy efficiency is theoretically enhanced by lowering energy dissipation on the source capacitance as well as saving energy in low-level negative peaks as described in Section 5.3.2. We then quantitatively estimate the saved power by using SSHI rectifiers compared to simply using bridge rectifiers. In one cycle, the charge loss on the source capacitance C_T of the TEH happens when charging the source capacitance C_T from 0 to $V_{rect} + 2V_{th}$ at the beginning of each cycle and from V_{invert} to $V_{rect} + 2V_{th}$. Comparing with using a bridge rectifier, the saved charge loss can be expressed as,

$$\begin{aligned} Q_{C_T,loss} &= 2(V_{rect}+2V_{th})C_T - (V_{rect}+2V_{th}-V_{invert})C_T \\ &= (V_{rect}+2V_{th}+V_{invert})C_T \end{aligned} \tag{5.9}$$

where V_{invert} is the achieved inverted voltage in each cycle as shown in Fig. 5.7 (d), which is determined by the LC resonance circuit. Specifically, V_{invert} depends on the quality factor, which is given by [157]:

$$\begin{aligned} V_{invert} &= (V_{rect}+2V_{th})e^{-\frac{\pi}{Q_F}} - V_{th}\left(1+e^{-\frac{\pi}{Q_F}}\right) \\ &= V_{rect}e^{-\frac{\pi}{Q_F}} + V_{th}\left(e^{-\frac{\pi}{Q_F}}-1\right) \end{aligned} \tag{5.10}$$

where Q_F is the quality factor of the LC resonant loop that is composed of the source capacitance C_T and the inductor L. Thus, the quality factor Q_F is given by

$$Q_F = \frac{\omega}{\alpha}, \quad \omega = \sqrt{\omega_0^2-\alpha^2}, \quad \omega_0 = \frac{1}{\sqrt{LC_T}}, \quad \alpha = \frac{R_{para}}{2L} \tag{5.11}$$

where R_{para} is the parasitic resistance of the LC resonator. Also, the charge loss on the internal resistance of the TEH, R_T, in every cycle is simply $Q_{R_T,loss} = \int_0^T \frac{V_T}{R_T}dt$. As the inner resistance of the TEH R_T is very large, the charge loss on the inner

resistance can be negligible.

The total charge produced by the TEH in every cycle is:

$$Q_{total} = \int_0^T |i_T|\, dt \tag{5.12}$$

And i_T can be calculated from Eq. (5.7) and Eq. (5.8) as dQ/dt, which is generated by triboelectric energy harvesting.

Therefore, the harvested power of the circuit with SSHI interface for every cycle is:

$$P_{invert} = V_{rect}\left(\frac{Q_{total} - Q_{C,loss}}{T}\right) \tag{5.13}$$

The difference between the full-wave bridge rectifier and the circuit with the proposed SSHI interface of the harvested power comes from the inverted charges due to the switching approach as Eq. (5.13). Therefore, the saved power comparing to only using abridge rectifier, P_{saved}, can be calculated as

$$P_{saved} = V_{rect}\frac{(V_{rect} + 2V_{th} + V_{invert})C_T}{T} \tag{5.14}$$

In some cases that the negative voltage peaks are not high enough to make bridge conduct, more power can be saved when using SSHI. In this case, the saved power can be estimated as

$$P_{saved} = V_{rect}\left(\frac{Q_{C,loss} + Q_{N,loss}}{T}\right) \tag{5.15}$$

where $Q_{N,loss}$ is the charge loss caused by the non-conduction of the bridge during the negative period of the TEH voltage.

5.4 Experiments and Results

In this section, the experiments and results for validating the new theoretical model of triboelectric energy harvesting and the proposed SSHI rectifier are both presented. The experiment platform for generating the sinusoidal distance and measuring necessary signals is established as shown in Fig. 5.8.

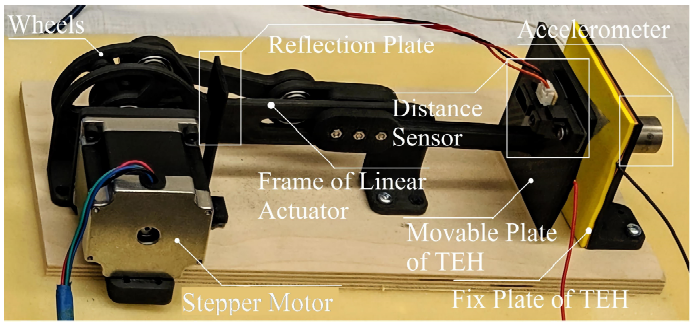

(a)

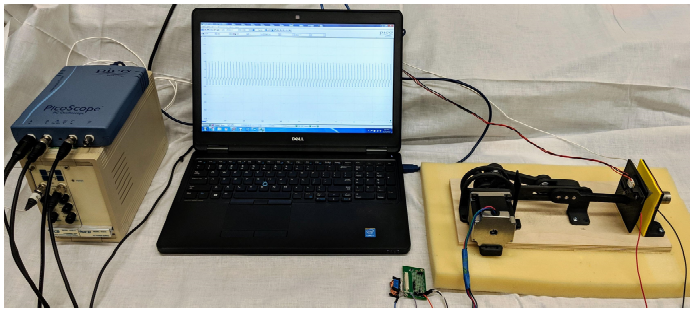

(b)

Figure 5.8: Experimental setup. (a) Linear actuator with sensors equipped that can generate sinusoidal displacement of the TEHs; (b) the entire experimental setup.

5.4.1 Experimental Platform and Setup

In order to achieve a sinusoidal separation distance of the two TEH plates for validation experiments, we first build an experiment platform that is capable of providing continuous sinusoidal movements. The details of the system are illustrated in Fig. 5.8 (a). The structure is mainly built based on a linear actuator and the mechanical design of a slider-crank mechanism [161]. A movable plate is mounted on the slider, which is connected to a coupler via a revolute joint and driven by a stepper motor. The frame and the wheels of the linear actuator are 3D printed using carbon fiber

nylon to provide a strong and light structure. An IR distance sensor (GP2Y0A21, Sharp Inc.) is equipped to monitor the displacement in real time. A reflection plate is coupled with the distance sensor. To measure the impact force during the two plates contacting, an accelerometer (50 g, 353B33, PCB Piezotronics Inc.) is attached to the fixed plate to measure the generated acceleration signal during contacting as the fixed plate is generally stable except when two plates contact.

The experimental setup is shown in Fig. 5.8 (b). The linear actuator is mounted on the wood board with a foam pad to stabilize the movement. The displacement and acceleration signals are monitored and stored in a laptop via an oscilloscope (PicoScope 4262, Pico Technology Inc.). This platform is capable of providing sinusoidal separation distance for TEHs as the controllable mechanical input and recording the necessary signals for validation experiments.

5.4.2 Simulation Results for Proposed Model of Triboelectric Energy Harvesting

For conventional mechanical energy harvesting, three mechanisms are generally used, which are piezoelectricity based on piezoelectric materials, electromagnetics based on Lenzs Law, and electrostatics based on variable capacitance [8][162]. For analyzing

these processes of energy conversion, sinusoidal forces are typically considered as mechanical input. For typical piezoelectric or electromagnetic energy conversion, the displacement or distance $x(t)$ and the generated source voltage $V(t)$ of harvesters are usually sinusoidal as well. This is because of the basically linear relationship between the displacement and the input force or vibration in these harvesting models although nonlinear terms also exist [163]. Although there could be a slight misalignment between theoretical models and experimental results, the output voltage is generally sinusoid with damping, phase shift and other slight modification comparing to the input waveform. However, in triboelectric energy harvesting, a sinusoid motion input generally cannot generate the sinusoid voltage across the two electrodes. Although a few studies have discussed the reason [148][150], it is also likely that the impact force dominates the generated charge as our analysis in Section 5.2.2 and Eq. (5.5) and Eq. (5.8).

We then conduct the numerical simulation of our proposed model and the corresponding experiments to validate the model. In the simulation, a sinusoid waveform is set as the input separation distance between the two TEH layers (also called displacement of the movable plate) of the TEH. Assume that the input displacement is $x(t) = D_{pp}sin(2\pi ft)$, where D_{pp} is the maximum displacement which equals to 25 mm in the experiment setup, f is the frequency and $f = 6$ Hz which is to simulate the low-frequency movement. The waveform of the displacement is plotted in Fig. 5.9 (a). The smaller the displacement, the closer the two layers are. When the impact

factor of the dynamic force is changed, it is dominant to both the amplitude and the waveform (*i.e.* frequency shift) of the output voltage of TEHs as shown in Fig. 5.2 (a). The higher the impact force is, the larger peaks the output voltage will achieve. When the impact factor (i.e. impact force) is higher and the contact and separation process is faster, the output voltage shows the higher frequency with damping. When changing the input frequency, simulation results show that the influence of the impact force is similar.

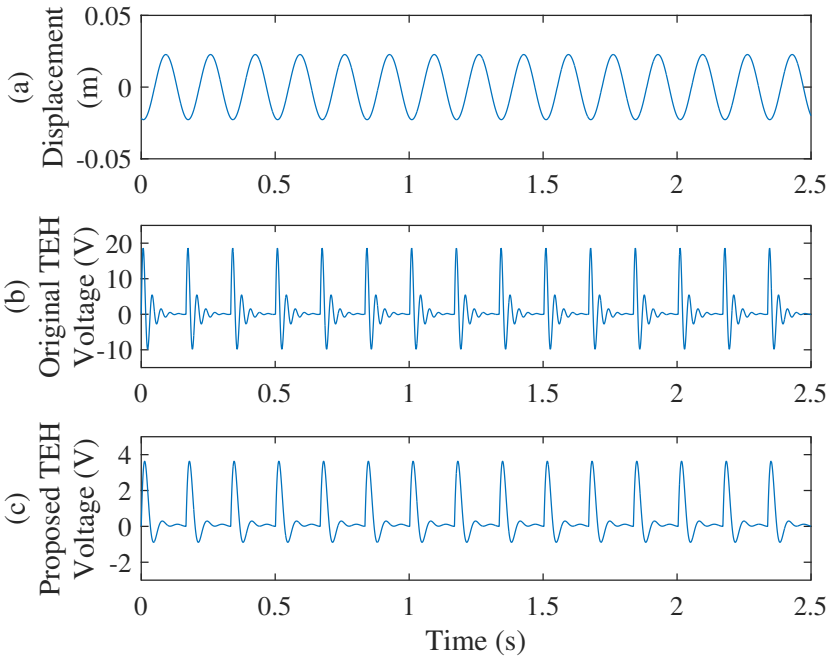

Figure 5.9: The simulation results from MATLAB: waveforms of (a) the displacement, (b) output of the original TEH, and (c) output of the proposed TEH with the pairing capacitor. The waveforms of (b) and (c) are related to Eq. (5.6) and Eq. (5.8), correspondingly.

In order to clearly illustrate the difference between Eq. (5.6) and Eq. (5.8) (without and with pairing capacitor) in Section 5.2.2, the solutions of the theoretical voltages

have been derived in MATLAB and plotted as 5.11 (b) and (c). By the new model as in Eq. (5.6), the theoretical voltage through TEH is plotted in Fig. 5.9 (b). With adding the pairing capacitor, the generated voltage of the TEH is plotted in Fig. 5.9 (c). After adding the pairing capacitor, the amplitude of the voltage output of the TEH is decreased but the width of the peak wave is extended. From Eq. (5.8), the pairing capacitance which determines the switching time in the SSHI interface also influences the amplitude of output voltage of TEHs. Figure 5.2 (b) shows the voltage with different values of pairing capacitance with the same other parameters. Higher pairing capacitance relates to a lower voltage for the same impact force. In the real design of rectifiers, however, we also need to consider the switching time and the practical multilayer structure of the TEHs and therefore cannot use very small pairing capacitance in the real design. With the analytical solution of the output voltage of the TEH, we then conduct experiments to validate it.

5.4.3 Validation Experiment and Results for Proposed Model of Triboelectric Energy Harvesting

In the validation experiments, the sinusoid separation distance $x(t)$ is achieved by the experiment platform in Fig. 5.7 as the mechanical input. The frequency is also 6 Hz. The real displacement is measured by the IR distance sensor and the signal is plotted in Fig. 5.10 (a). During each cycle of the sinusoidal movement, a periodic signal is

achieved. After the plates contact, the foam layer is pressed till having a minimum thickness. After a short period, the TEH output reaches its maximum value. Both positive and negative peaks are clearly shown in Fig. 5.10 (b) and (c), which are the measured voltage output of the TEH without and by adding the pairing capacitor, respectively. In Fig. 5.10 (b), the TEH output shows deep narrow positive and negative peaks as the theoretical voltage in Fig. 5.9 (b). The similarity also exists in the case by adding the pairing capacitor. In Fig. 5.10 (c), the positive and negative peaks of the TEH output are enlarged in terms of time, which corresponds to Fig. 5.9 (c). With a higher impact force, the positive voltage peak is always higher in the experiments as well. From the validation experiments, it shows that our proposed theoretical model aligns well with the experimental results.

5.4.4 The TEH Performance

Next, more experiments are conducted to evaluate the energy harvesting performance. First of all, the performance of the new low-cost easy-assembly TEH as designed for the proposed SSHI is estimated. In the experiment, the TEH applied to charge a load capacitor under a low-frequency periodic motion via the linear actuator. The experiment setup is the same as Section 5.4.1. The load capacitors with different capacitance, 2.2 μF, 10 μF, 47 μF, and 470 μF, are used to quantitatively demonstrate the charging behavior in comparison. The results are shown in Fig. 5.11. For all

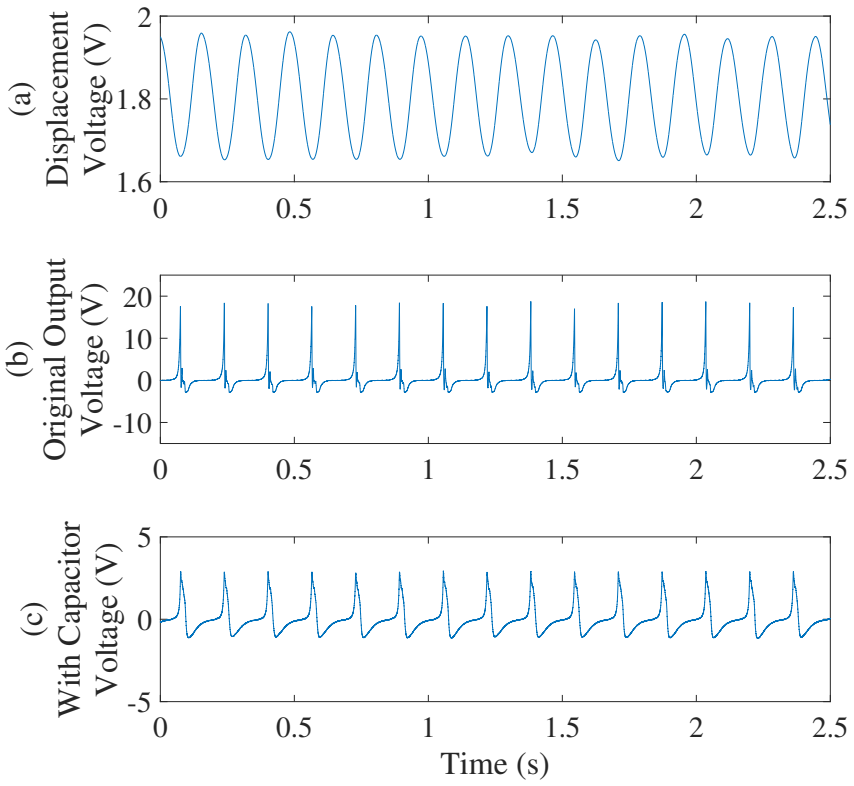

Figure 5.10: Measured voltage in the validation experiments of the new model. Signals of (a) the displacement, (b) output of the original TEH, and (c) output of the proposed TEH with the pairing capacitor.

load capacitors, the saturation charging curves are observed. The charging speed gradually decreases along with time until the charging voltage reaches the maximum of approximately 1.3 V. For a 2.2 μF load capacitor, it takes about 10 seconds to charge to 1.3 V. For a load capacitor with larger capacitance, it takes a longer time to reach its saturation voltage. This demonstrates that our ultra-low-cost, easily-assembled TEHs can also achieve good results.

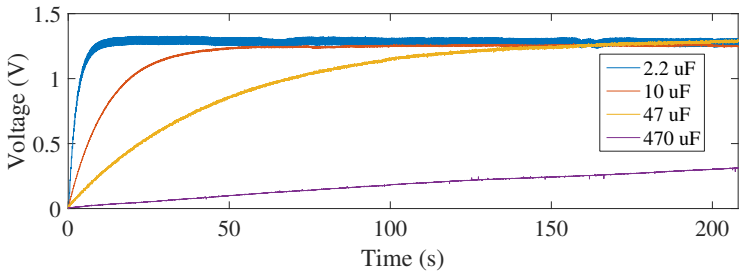

Figure 5.11: Charging different capacitors with the proposed TEH.

5.4.5 Experiment and Results for the Proposed SSHI Rectifier

In the design of the pairing capacitor that is used to ensure the source capacitance within a controllable range, the pairing capacitance C_{pair} is designed to be larger than the value of $C_{air}||C_{Foam}$. The total capacitance of the TEH is designed to have a limit of 50 nF. The inductance L is 100 mH. Therefore, the optimal switching-on time is selected to be half period of the LC resonance circuit, which is 222 μs in this case.

In the experiments, the fixed plate keeps stable while the movable plate moves at a frequency of 6 Hz which is the same as the simulated input for the theoretical model. The switching signals have a frequency of 12 Hz and a period of 83.33 ms which is much longer than the switch-on time. The switching is turned on twice in one cycle when the voltage of the TEH reaches its positive and negative peaks. This is because when the current i_T is zero crossing, the voltage V_T reaches its maximum.

The synchronization of the switching interval and the extreme positions of the plate movements are critical to power efficiency. If the switching-on occurs before or after the time point, the mechanical energy is hardly ensured to be optimized to transfer to the load. The switch is composed of a pair of n-MOSFETs to ensure the switching for both positive and negative peaks. The input impedance of the oscilloscope for measurements acting as the load resistance in the validation experiments is 10 M. Four signals are measured and recorded, displacement of the movable plate by the IR sensor, the acceleration signal from the accelerometer, the output voltage of the TEH with a bridge rectifier and that with an SSHI rectifier.

The experiment results of the synchronized signals are illustrated in Fig. 5.12. Figure 5.12 (a) shows the periodical signal of the displacement detected by the IR distance sensor, which shows that our platform using the slider-crank mechanism and linear actuator can generate a stable sinusoidal motion for experiments. The acceleration signal is plotted in Fig. 5.12 (b) to illustrate the contact force in each cycle. The original output of the TEH without the pairing capacitance is shown in Fig. 5.12 (c). The output voltage ranges from -3 V to +19 V, which equals to a peak-to-peak voltage of 22 V. For the new TEH with the pairing capacitor added by the multilayer structure, the peak output voltage is lower whereas the effective area is wider.

The TEH voltage with a bridge rectifier and with the SSHI rectifier are measured for validation and plotted in Fig. 5.12 (d) and (e), representatively. The actual output of

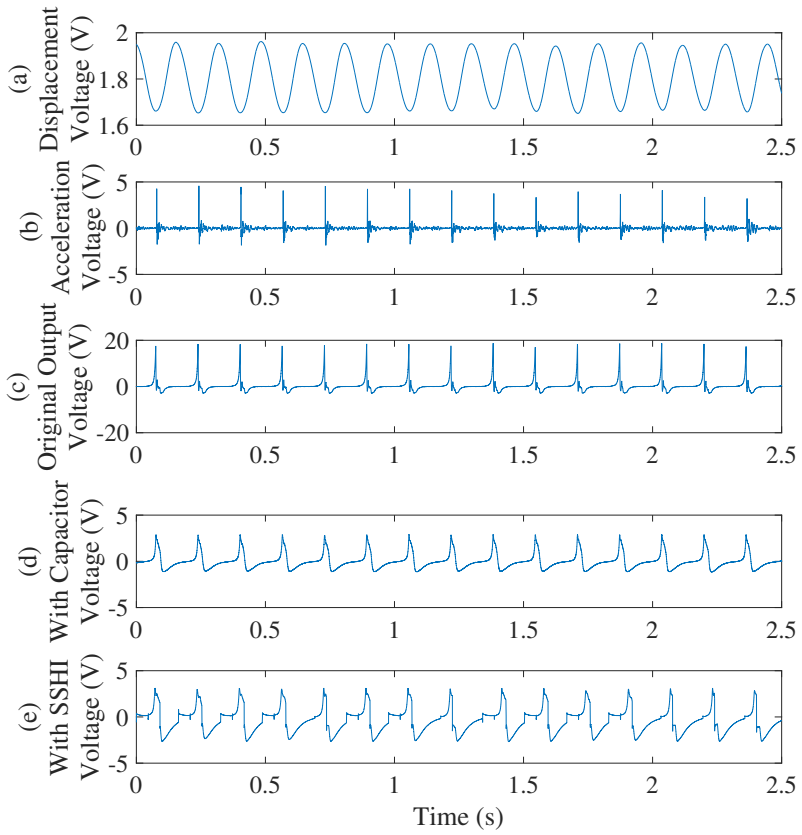

Figure 5.12: Measured voltages in the experiments for validating the SSHI rectifier performance. (a) Displacement voltage detected by the IR distance sensor; (b) acceleration signal from accelerometer; (c) TEH voltage with no rectifiers or pairing capacitor; (d) TEH voltage with a bridge rectifier; (e) TEH voltage with the SSHI rectifier.

the SSHI interface aligns well with the theoretical analysis of the operation as shown in Fig. 5.7. In the measured TEH voltage with the SSHI rectifier, in the beginning, the voltage gradually increases to the peak. There is a very short slope down after the peak which may be the ripple of V_{rect}. Then the switch is quickly turned on, and the TEH voltage immediately flips to a negative value that is lower than the negative peak, which is V_{invert}. From V_{invert} to a negative peak, a charge process can be clearly observed from the measured TEH voltage waveform. Also, in this case,

the negative peak of the TEH voltage with a bridge rectifier is not high and cannot conduct the bridge in the negative half as shown in Fig. 5.12 (d). Thus the TEH voltage in the negative half cannot reach $V_{rect} + 2V_{th}$ and stay low. The LC resonant loop in the SSHI rectifier seems to successfully flip the voltage and thus can achieve a much higher peak in the negative half and conduct the bridge in the negative cycle in Fig. 5.12 (e). This synchronized switching approach can boost up the harvested power. Thus, the measure results align well with our theoretical analysis.

We then measured and calculated the harvested power in the experiments by adding a load resistor. In order to estimate the energy enhancement of the proposed SSHI rectifier for the TEH compared with the commonly used bridge rectifiers in existing studies, the output power with and without the SSHI interface circuit is calculated and compared. The input for both cases is the same and is generated by the linear actuator and a step motor. The input power is approximately constant in the experimental platform. The average power in one cycle is calculated as

$$P_{avg} = \frac{1}{(t_3 - t_0)} \int_0^T \frac{V_{rect}^2}{R_L} \, dt \tag{5.16}$$

In the experiments, 60 sets of experimental data have been recorded and analyzed. The average power harvested in 60 sets of experiments with or without the proposed SSHI interface circuit has been organized and shown in Fig. 5.13. In all the 60

experiments, the outputs with the proposed SSHI interface circuit are higher than that from the TEH. Similar results occur in the average harvester power, as shown in Fig. 5.13. For both average power and maximum power, the ratio of the harvested energy with and without the SSHI interface circuit can be up to 3.4283, which indicates that the energy efficiency has been enhanced by up to 242.83%. This value shows that the proposed SSHI interface can significantly improve energy efficiency in triboelectric energy harvesting.

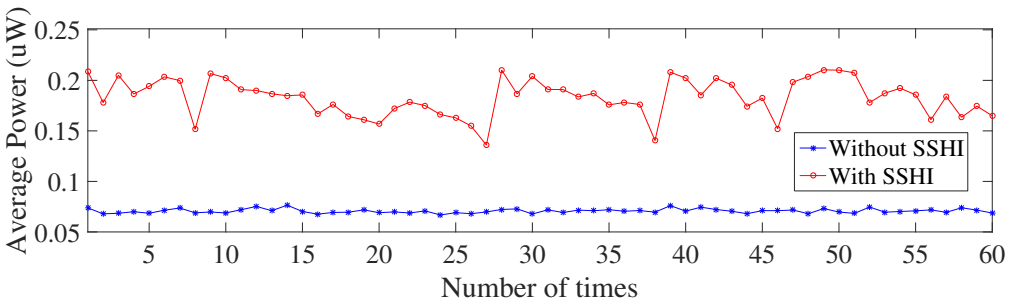

Figure 5.13: Average harvested power of the proposed TEH with or without the SSHI interface circuit in 60 sets of experiments with the frequency of the input motion of 6 Hz.

5.5 Conclusion

In this chapter, an SSHI rectifier for triboelectric energy harvesting is first attempted and reported. A new design of TEH with a multilayer structure is also presented with the consideration of the source capacitance. It also shows that ultra-low-cost materials and easy fabrication can also generate good results for mechanical energy harvesting

using TEHs. The experimental results show that the harvested energy efficiency can be significantly improved by the proposed SSHI interface. The efficiency enhancement of the proposed synchronized switching approach is up to 242.83%. The introduction of the SSHI interface provides a promising strategy for triboelectric energy harvesting in the AC-DC stage.

Chapter 6

Wireless Biopotential Monitoring System

6.1 Introduction

In this chapter, a wireless wearable system will be developed for monitoring multiple biopotentials. The performance of the proposed system, including the capability of detecting multiple biopotentials and the stability in long-term monitoring, will be evaluated. Moreover, the power consumption on wireless transmission will be optimized by proposing a data compression algorithm. The power and lifetime of the proposed system will be theoretically estimated.

6.2 Biopotential Monitoring

The biopotential signals in long-term monitoring will provide essential information for various human physiological conditions and are usually used for chronic diseases diagnosis. The most common biopotential signals include electrocardiogram (ECG), electromyography (EMG), and electroencephalogram (EEG). ECG is a good indicator of heart diseases, as well as EMG for muscle relevant diseases and EEG for brain relevant disorders. In this section, the proposed wireless wearable system will be tested for ECG/EMG/EEG monitoring.

6.2.1 ECG Monitoring

The wireless biopotential monitor designed in this study can apply to detect ECG signals without directly contacting human skins. The performances have been tested by attaching different layers of cloth with different materials between the electrodes and human skins. The biopotential monitor is applied to detect ECG signals without directly contacting electrodes with human skins. Between the electrodes and the skin, there are different layers of cloth with different materials. In this experiment, the ECG signals were recorded using a digital scope. The ECG signals are detected from fingers locations of the right and left hands.

Before the non-contact ECG detecting experiments, the features of different materials have been studied. In the experiments, five types of common fabric materials (Cotton, Jeans Cotton, Polyester Blend and 2 types of Polyesters) have been used. Table 6.1 summarizes the relative permittivity and the average thickness of those clothes. The relative permittivity values in 6.1 are reference values. The average thicknesses are obtained by measuring different levels of cloth multiple times.

The ECG signals detected by attaching different cloth with different materials to the electrodes have been represented in Fig. 6.1. The raw ECG signals have been recorded as a reference to compare the performances of non-contact electrodes outputs. Among the ECG signals shown in Fig. 6.1, the signals obtained from contacting with polyesters are freer from noises than the other signals. One of the reasons is related to the thickness of the cloth since the coupling capacitance between electrodes and human skins changes along with the inside distance. This explanation has been supported by testing how many layers of cloth with different materials can be attached before detecting unrecognized ECG signals. In this study, the maximum layers for Cotton, Jeans Cotton, Polyester Blend, Polyester A, and Polyester B are 5, 4, 5, 13, and 19, respectively. The thinnest cloth (Polyester B) obtain the biggest value of the maximum layers. The maximum thickness of cloth during testing is 2.6 mm for Jeans Cotton. But the order of the cloth with the maximum layers is different from the order of the thicknesses. However, the other reasons are related to the triboelectric artifacts, which was discussed in Chapter 4.

Table 6.1
Characteristics of clothes with different materials.

Materials	ε_{ref}	Average Thickness (mm)	Maximum Through-layer	Maximum Through-Thickness (mm)
Cotton	1.3 - 1.4	0.254	5	1.27
Jeans Cotton	$\sim$ 1.59	0.650	4	2.60
Polyester Blend	$\sim$ 1.39	0.226	5	1.13
Polyester A	2.8 - 4.5	0.130	13	1.69
Polyester B	2.2 - 2.4	0.090	19	1.71

6.2.2 EMG Monitoring

As the ECG signals, the EMG signals are important biopotential signals that provide vital health information of muscles. The biopotential monitor designed in this study is also capable of detecting EMG signals. In order to obtain the potential of the biopotential monitor, two kinds of EMG signals have been detected: the Upper Limb EMG and EMG during eyes blinking. The positions of the biopotential monitor attached to the human body have been demonstrated in Fig. 6.2.

For detecting the Upper Limb EMG, one of the biopotential monitor electrodes was fixed via clenching fingers. Another electrode was attached to the forearm. During detecting, the subject moved the hand along the wrist and toward to the forearm. The EMG signals have been shown in Fig. 6.3. The signals recorded in the 20 seconds

can be divided into 3 parts: the first part and the third part are EMG signals during the forearm muscles stay in the tension status. The middle part of the signal is the EMG signal while the muscles stay in relaxation status. The signals fit well as the experiment sets, which indicates that the biopotential monitor can successfully detect EMG of the Upper Limb movement.

During eyes blinking, the muscles around the eyes stay in the tension or the relaxation status. The EMG signals of eyes blinking can be detected by attaching the electrodes around the eyes. Fig. 6.4 shows the EMG signals during blinking the left or the right eye separately. When blinking one of the eyes, there will be pulses emerged on the signal waves. The main difference between the pulses is peaks or troughs existed. It is clear from the EMG signal in Fig. 6.4 that, for the settings in our study, there are troughs emerged while blinking the left eye and peaks existed while blinking the right eye. The pulses indicate that the biopotential monitor is capable of detecting the EMG signals of eyes blinking.

6.2.3 EEG Monitoring

EEG is a good and important biopotential signal to identify activities in human brains, like the wakefulness and fatigue. EEG is usually recorded by a measurement system. Evaluation of EEG measurement system can be difficult since EEG signals

cannot be reproduced in different recording sessions and have no fixed patterns like ECG signals. However, there are four major bands of EEG signals that range in 0 - 4 Hz (Delta wave), 4 - 7.5Hz (Theta wave), 7.5 - 13 Hz (Alpha wave) and 13 - 30 Hz (Beta wave), respectively. The appearing of typical waveforms of the major bands, especially the Alpha wave, can be used to recognize the detection of EEG signals. With the help of the power spectrum and time-frequency plots, it is easy to analyze the typical waveforms. So, in this study, the evaluation of our wireless wearable system is conducted by deriving these typical waves of EEG signals.

The EEG data collection has been finished by the biopotential monitor system. The proposed system has an adjustable gain that could be applied to different measurement scenarios. High gains have been equipped for EEG signal detection while low gains are used for ECG monitoring. Two electrodes have been attached to the left ear and the left forehead of the subject. According to the EEG detection standard (International 10-20 system), the EEG channel recorded at these positions are related to EEG signals at Fp3 (the left forehead) referred to A1 (the left ear). The subject was taking a nap before the test. During the test, firstly, the subject kept the eyes opened for 10 seconds. Then the subject closed eyes for another 10 seconds. The raw EEG signal has been recorded. However, the raw EEG signal is bared to the baseline drift due to subjects tiny movements. So the raw EEG has been filtered by a bandpass filter (4 - 30 Hz). The detected EEG signal after filtering has been shown in Fig. 6.5. We can tell the difference between the first half and second half signals.

The waves in the second half signal have larger amplitudes.

Though the raw EEG signal has the baseline drift, the signals features in our interested frequency bands have still been recorded successfully. The bandpass filters are applied to get the four major bands. Fig. 6.6 shows the raw EEG signal and its extracted waves. Comparing the signals of the Alpha band in the first and second 10 seconds, the typical Alpha waveform has appeared obviously in the second half period. It is well known that the Alpha waves appear most prominent when the subject is at rest with eyes closed and disappear gradually with eyes open [48]. The observation of Alpha waves can be used as evidence that EEG signals are in fact being monitored. In order to confirm the Alpha waves did appear when the subject closed the eyes in the test, the power spectrums of detected EEG signals in eye-closed and eye-open states have been conducted and compared in Fig. 6.7. A frequency peak (10.35 Hz) in Alpha wave band has shown in the eyes closed period. Joint Frequency Time (JFT) plot is always applied to demonstrating the Alpha waves in EEG signal analysis. The JFT plot for the Fp3-A1 differential EEG data in this study has been shown in Fig. 6.8. These dark red regions in the white dash circle correspond to peaks in Alpha waves at around 10.35 Hz during the second 10 seconds testing. The analysis above has illustrated that the EEG signals can be detected successfully via the biopotential monitor system.

6.3 System Stability

For the out-of-hospital applications, the biopotential monitoring systems are generally used for long-term purpose. We also tested the system stability in a relatively longer duration. An experiment of monitoring the ECG signals for 45 minutes was conducted. Various parameters were extracted to validate the system performance during the experiment. The 45-minute testing was divided into 9 time periods to show the system performance with possibly changed skin-electrode interface due to long time use. The extracted parameters include the signal-noise ratio (SNR), heart rate (HR), out of range times, and shift percentage. The raw ECG in longer time duration is shown in Fig. 17, which is quite stable over time. The HR is calculated by averaging the heart beats in every one minute. The out of range times refers to how many times the signal was out of range during the testing time period. The shift percentage is defined as the ratio of the time duration that the signal shifts around the baseline to the total time duration. These four parameters during 45 minutes of testing were summarized and compared in Table 3. Those values show that there are no obvious changes for these parameters during the total testing. Take the SNR as an example. The SNR of the first 5 minutes (1-5 min) has no significant difference comparing to the last 5 minutes (41-45 min).

Table 6.2
System performance during 45-minute testing.

Time (min)	1-5	6-10	11-15	16-20	21-25	26-30	31-35	36-40	41-45
SNR (dB)	1.52	19.00	19.17	19.27	18.86	18.52	18.74	18.43	19.05
HR	64.6	67.0	67.2	70.2	71.6	69.2	69.8	71.6	71.4
Out-of-Range Times	0	0	0	0	1	2	1	0	0
Shift Percentages	1.05%	1.17%	1.83%	3.54%	4.22%	7.12%	3.67%	2.33%	1.33%

In addition, we also tested the system performance regularly since it was built. One test after nearly one year was conducted to validate the long-term performance. We followed the same testing procedure. During this test, different layers of jeans cotton cloth were stacked between the electrode and the finger skin. The detected ECG signals are shown in Fig. 6.10. It indicates that the button has high stability during long-term use.

6.4 Power Optimization

Due to the limited power supply, energy efficiency imposes a stringent constraint in the wearable systems, where long life is highly demanded in long-term biopotential monitoring. In order to maintain the long lifetime, the system needs to obtain the high energy efficiency, which can be achieved by two paths, increasing the harvested energy from the energy source and lowering the power consumption of the system. The

former path has been discussed in Chapter 5, which relates to developing a power management circuit to improve the efficiency of the TEH. The latter path will be introduced and explained in this section. As a wireless sensor network, the wearable system proposed in this study has a significant amount of power consumed by wireless transmission. A common and practical way to lower the power consumption of the wireless system is decreasing the power demand on its wireless transmission module. This study adopts the data compression technique to effectively decrease the power utilization on data transmission. In this study, we develop a new method for ECG signal compression by leveraging empirical mode decomposition (EMD) and online dictionary for the proposed wireless wearable system. The algorithm and framework of the EMD algorithm will be introduced in this section.

6.4.1 Data Compression

Low-power consumption is a major challenge to wireless wearable systems for long-term biopotential monitoring with limited battery life. For a wireless system, the wireless data transmission consumes most of the system energy. Recently, data compression has become a common method of low-power data transmission for wireless wearable systems. In this study, we propose a new data compression method in our wireless wearable system for long-term biopotential monitoring. The data compression method in this study is presented by leveraging EMD to construct a new

online dictionary composed of Intrinsic Mode Functions (IMFs), which includes three phases, online dictionary construction, signal compression, and recovering after wireless transmission.

Table 6.3
The process of obtaining the IMFs from an ECG signal [164].

Algorithm 1: Decompose signal into IMFs
1) Identify all extrema of the input ECG frame, $x(t)$;
2) Interpolate the local maxima to to form an upper envelope, $u(x)$;
3) Interpolate the local minima to form a lower envelop, $l(x)$;
4) Calculate the mean envelope $m(t) = \frac{1}{2}(u(x) + l(x)$;
5) Extract the mean from the signal and obtain $h(t) = x(t) - m(t)$;
6) Check wheather $h(t)$ satisfies the IMF property:
If yes, save $h(t)$ as an IMF and continue for other ECG frames;
If not, keep iteration on $h(t)$ till it is satisfied.

In the first phase, a dictionary with $M \times N$ IMFs is constructed. These IMFs extracted from the biopotential signals (i.e ECG in this study) are self-similarities leveraging the inherent property for decomposition. The symbol M represents the depth of the possible layers of IMFs needed for the signal recovery. It is decided by the user and commonly around 5-7. Another symbol N means the number of arbitrary input ECG frames. It is identified depending on the situations. The process of decomposing the ECG signals into a finite number of IMFs is expressed as Algorithm 1 in Table 6.3 (adopted from [164] with permission). The IMF property shown in Algorithm is that the number of extrema and zero-crossings in an IMF differs at most by 1. After the Algorithm 1, all extracted $M \times N$ IMFs are saved in the memories of both

the transmitter and the receiver for the compression and reconstruction, respectively. The pre-saved IMF bases are pre-stored without the computational cost and can be updated as needed.

The second phase is the signal compression stage. A specific signal frame needs to be selected from the N frames. For the ECG signals used in this study, the location of QRS complexes in both the input ECG frame and the matching ECG framework needs to be close enough. The index of the matching ECG frame in the N frames needs to be stored and sent to the receiver with the coefficients of the M IMFs. Therefore, for an input ECG signal, only $M + 1$ number of data will be transferred and used for reconstruction in the third phase. The coefficients of the IMFs can be expressed as

$$\alpha = (IMF^T IMF)^{-1} IMF^T Y \tag{6.1}$$

where $\alpha = \alpha_1, \alpha_2, ..., \alpha_M$, $IMF = IMF_1, IMF_2, ..., IMF_M$, Y is the input ECG frame, which can be represented by

$$Y = \alpha IMF^T + \epsilon \tag{6.2}$$

where ϵ is the error of the reconstruction of the ECG frame. It can be minimized by

$$min||Y - \alpha IMF^T|| \tag{6.3}$$

The third phase, ECG reconstruction, will be performed on the receiver. The recovered ECG frame Y' is the linear combination of the corresponding IMFs under the matching ECG frame with the received coefficients. Y' can be expressed as Eq. 6.4.

$$Y' = \alpha IMF^T \tag{6.4}$$

In our previous experiments, the performance of the proposed EMD method has been validated by comparing to the performance of the state-of-art dictionary based ECG compression methods. Table 6.4 (adopted from [164] with permission) shows the comparison results. Our EMD method has achieved a compression rate (CR) of up to 42.8 with the average root mean square error (RMSE) of 4.82%. Figure 6.11 (adopted from [164] with permission) compares the reconstructed ECG signal recovered by the proposed EMG method with the original clinical ECG data from MIT-BIH ECG database [165]. The data compression method in this study has a much higher CR with the comparable RMSE, and can successfully reconstruct the ECG signals from the compressed data in high quality. It indicates the proposed data

compression method is capable of significantly optimize the power consumption for our wireless wearable system.

Table 6.4
Results of ECG compression performance.

Methods	CR	RMSE
Ref. [166]	27.50	5.00%
Ref. [167]	25.64	5.50%
Ref. [168]	13.79	4.20%
Proposed	42.80	4.82%

6.5 Conclusion

In this chapter, a wireless wearable system for monitoring multiple biopotentials has been developed with considering optimizing the power consumption on wireless transmission. The performance of the proposed system (capability and stability) has been evaluated by detecting multiple biopotentials (ECG/EMG/EEG) and testing in long-term monitoring. Moreover, a data compression algorithm (EMD), has been applied to optimize the power consumption on wireless transmission.

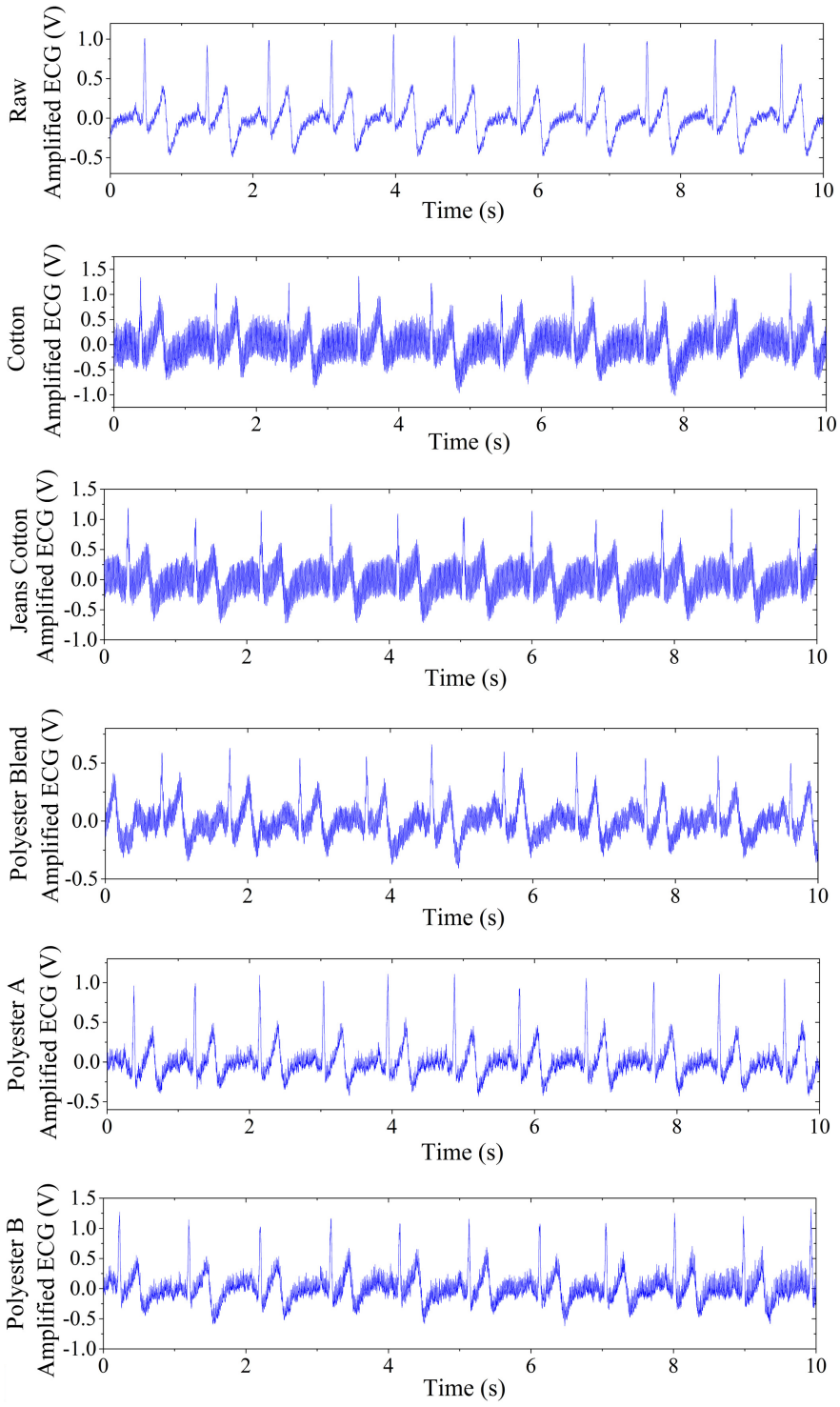

Figure 6.1: The outputs of ECG signals detected by the proposed system with different cloth materials.

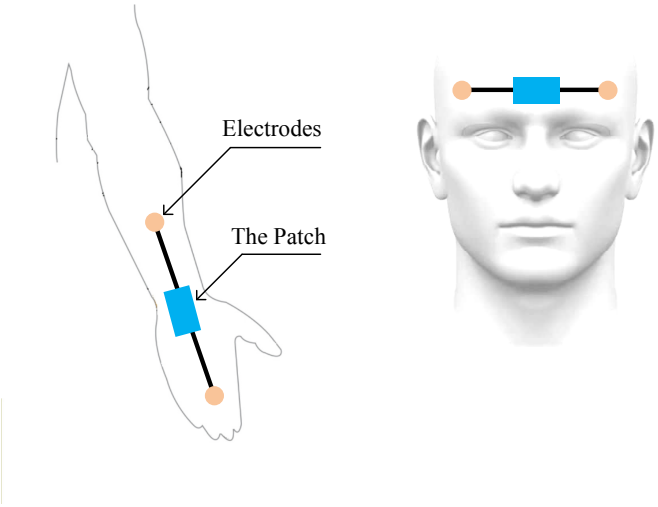

Figure 6.2: Positions of the Patch during detecting upper limb and eyes blinking EMGs.

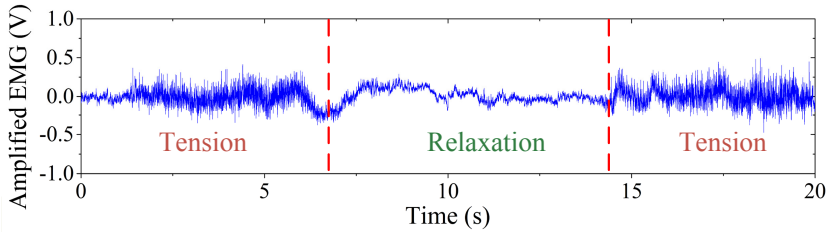

Figure 6.3: EMG signals detected at the upper limb.

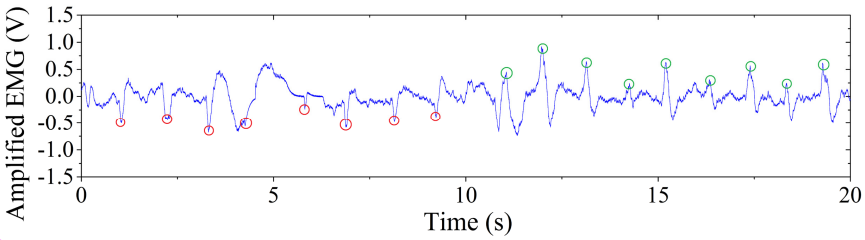

Figure 6.4: EMG signals of eyes blinking (red circles: blinking the left eye; green circles: blinking the right eyes).

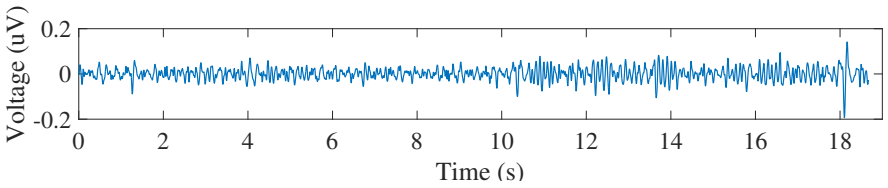

Figure 6.5: Detected EEG signal after filtering.

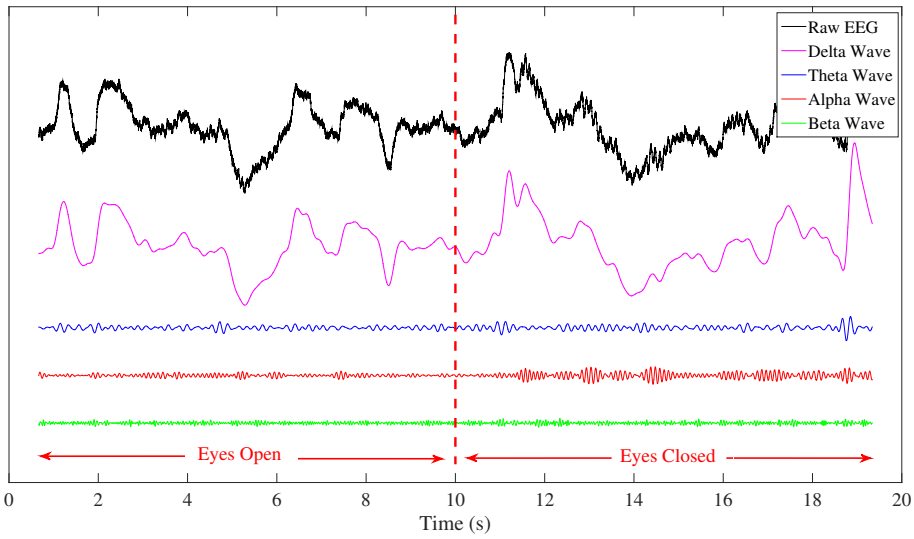

Figure 6.6: Extracted EEG waves in time domain during testing.

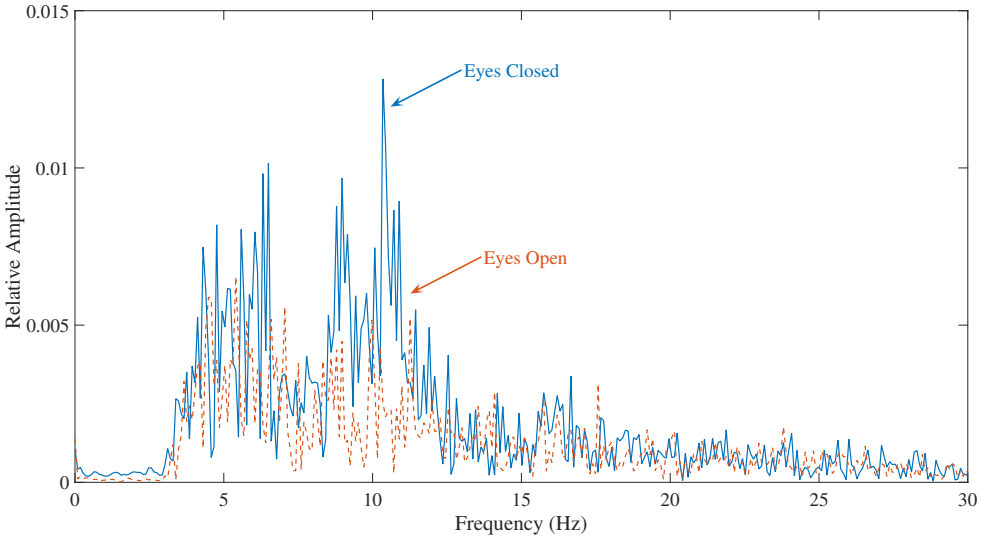

Figure 6.7: Power spectra in the frequency domain for Alpha and Beta rhythms.

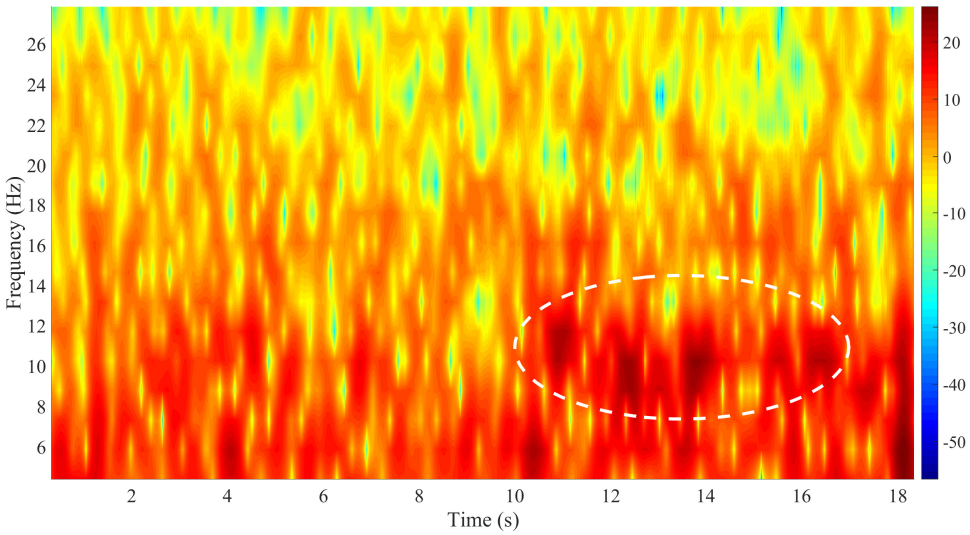

Figure 6.8: JFT plot for the Fp1-A1 differential EEG data (the dark red regions in the white dash circle correspond to peaks in Alpha waves at around 10.35 Hz).

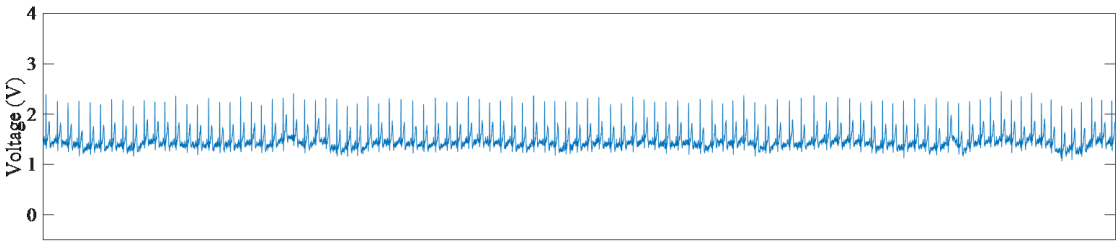

Figure 6.9: Raw ECG signal in longer time duration.

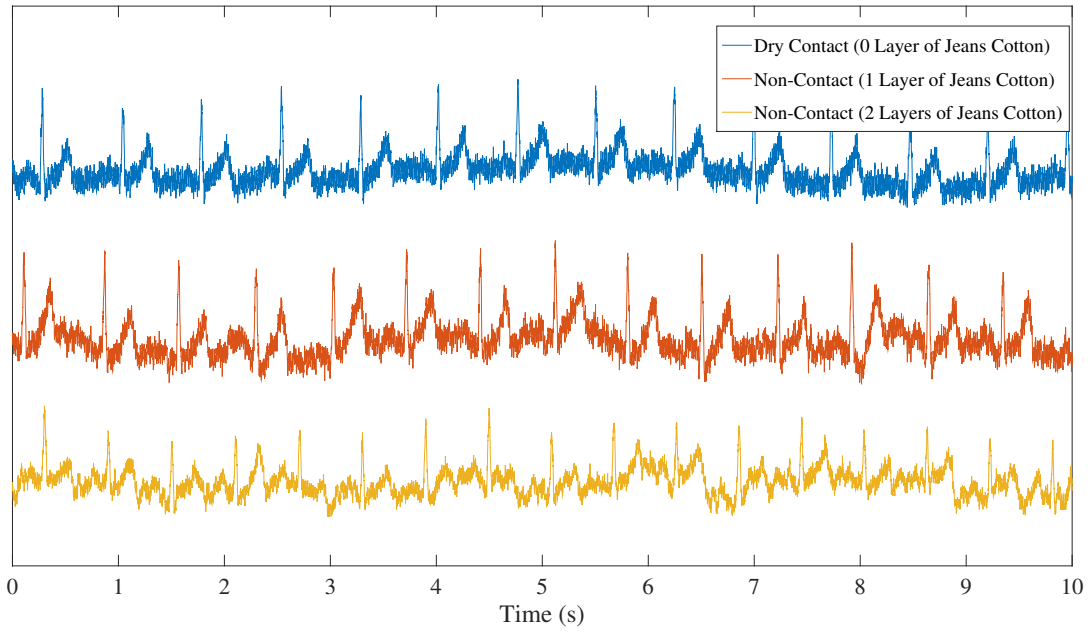

Figure 6.10: Detected ECG signals through different layers of jeans cotton cloth after one-year use.

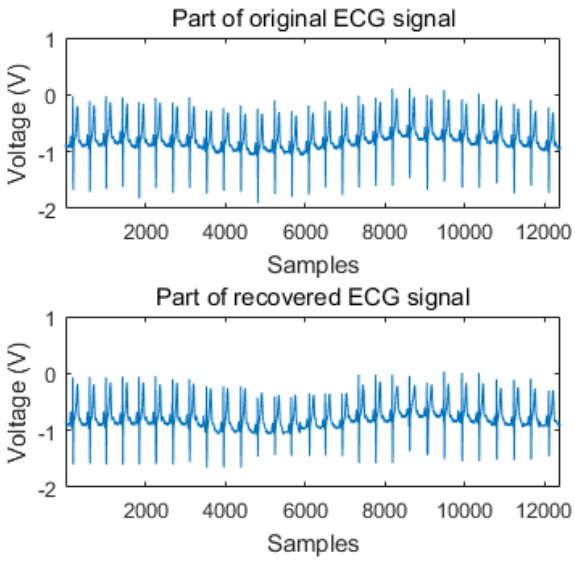

Figure 6.11: Comparison of Clinical ECG and the reconstructed signal with CR of 42.8.

Chapter 7

Conclusion and Future Work

7.1 Conclusion

In this dissertation, we developed a wireless wearable system for biopotential monitoring. The system features high comfortability in the measurement of biopotentials on the human body by applying the non-contact electrodes and requires no physical contact with the skin. The non-contact electrodes can significantly detect biopotential signals through several levels of fabric materials. It increases the flexibility and possibility of long-term monitoring biopotentials for the patients with extreme sensitivity skins (i.e. burn skins). The system is capable of being powered by a hybrid power supply consisting of energy harvesting and chargeable battery. The

system can be partially powered by the energy harvested from human motions via triboelectric energy harvesters. The lifetime of the system can also be boosted up by several strategies for the long-term monitoring purpose. An SSHI rectifying strategy has been proposed to increase the energy efficiency of the triboelectric energy harvesting at AC-DC stage. A new perspective on designing the TEHs is proposed by considering the capacitance concurrently. The power consumption of the system is reduced by introducing the data compression technique into the biopotential data transmission. The performance of the wireless wearable system has been validated by monitoring multiple biopotentials including ECG, EMG, and EEG. System stability has also been tested. The power consumption and the lifetime of the proposed wearable system have been theoretically estimated.

7.2 Recommendation for Future Work

This dissertation is an interdisciplinary study that integrated wireless wearable sensor networks, biopotential monitoring, and triboelectric energy harvesting. Based on the current research, we have recommendations for future work in the following three directions. They are multiple electrodes deployment, Internet-of-Things (IoT) integration, and triboelectric artifacts study.

For the clinical diagnosis, 2-electrode in this study is not enough for getting the

essential required biopotential features. For example, because of providing essential information of the heart's electric activity, 12-lead ECG is commonly adopted in the hospitals, instead of the simple 2-lead ECG. In other words, 12-electrode are required for detecting the patient's ECG signals and indicating the physiological condition of the patient's hearts. Deploying multiple electrodes is the trend of enriching the function and enlarging the applicable scenes for the proposed wireless wearable system in biopotential monitoring.

As a popular trend nowadays, IoT enriches the technological experience of people's normal lives. As a part of the IoT system, our wireless wearable system needs the ability to communicate with the web-enabled smart devices, like smartwatches or smartphones. One method to conveniently enable and enhance the communication ability is applying the wireless technology standards, i.e. Bluetooth 5.0 [169], for the system. With ensuring the data transmission rate, the new adopted wireless standards will enhance the communication capability of our system to other IoT devices. Combing with the suggestion of deploying multiple electrodes, we recommend applying those with better data bandwidth capacity while considering applying the wireless standards.

Motion-induced artifacts are inevitable in long-term biopotential monitoring and widely exist in the recording process for wearable devices regardless of electrodes.

In our study, motion artifacts have two primary origins: 1) electrification and triboelectrification caused by contact and friction and 2) variation of the skin-electrode interface caused by motion. The electrification and triboelectrification caused by contact and friction lead to the triboelectric artifacts. A fundamental understanding of triboelectric artifacts can provide new evidence for estimating the artifacts and inspire new methods to mitigate the triboelectric artifacts and to improve the signal stability of biopotential monitoring systems.

References

[1] WHO. (2017) World Health Organization cardiovascular diseases (cvds). [Online]. Available: https://www.who.int/news-room/fact-sheets/detail/cardiovascular-diseases-(cvds)

[2] E. J. Benjamin, S. S. Virani, C. W. Callaway, A. M. Chamberlain, A. R. Chang, S. Cheng, S. E. Chiuve, M. Cushman, F. N. Delling, R. Deo *et al.*, "Heart disease and stroke statistics2018 update: a report from the american heart association," *Circulation*, vol. 137, no. 12, pp. e67–e492, 2018.

[3] S. Mendis, P. Puska, and B. Norrving, *Global atlas on cardiovascular disease prevention and control*, 2011. [Online]. Available: https://apps.who.int/iris/bitstream/handle/10665/44701/

[4] CDC. (2017) Centers for Disease Control and Prevention death and mortality. [Online]. Available: https://www.cdc.gov/nchs/fastats/deaths.htm

[5] A. S. Go, D. Mozaffarian, V. L. Roger, E. J. Benjamin, J. D. Berry, M. J. Blaha, S. Dai, E. S. Ford, C. S. Fox, S. Franco *et al.*, "Heart disease and stroke statistics2014 update: a report from the american heart association," *Circulation*, pp. 01–cir, 2013.

[6] S. Patel, H. Park, P. Bonato, L. Chan, and M. Rodgers, "A review of wearable sensors and systems with application in rehabilitation," *Journal of neuroengineering and rehabilitation*, vol. 9, no. 1, p. 21, 2012.

[7] M. Rasouli and L. S. J. Phee, "Energy sources and their development for application in medical devices," *Expert review of medical devices*, vol. 7, no. 5, pp. 693–709, 2010.

[8] R. Vullers, R. van Schaijk, I. Doms, C. Van Hoof, and R. Mertens, "Micropower energy harvesting," *Solid-State Electronics*, vol. 53, no. 7, pp. 684–693, 2009.

[9] P. D. Mitcheson, E. M. Yeatman, G. K. Rao, A. S. Holmes, and T. C. Green, "Energy harvesting from human and machine motion for wireless electronic devices," *Proceedings of the IEEE*, vol. 96, no. 9, pp. 1457–1486, 2008.

[10] P. L. Green, E. Papatheou, and N. D. Sims, "Energy harvesting from human motion and bridge vibrations: An evaluation of current nonlinear energy harvesting solutions," *Journal of Intelligent Material Systems and Structures*, vol. 24, no. 12, pp. 1494–1505, 2013.

[11] A. Khaligh, P. Zeng, and C. Zheng, "Kinetic energy harvesting using piezoelectric and electromagnetic technologiesstate of the art," *IEEE Transactions on Industrial Electronics*, vol. 57, no. 3, pp. 850–860, 2010.

[12] C. Saha, T. Odonnell, N. Wang, and P. McCloskey, "Electromagnetic generator for harvesting energy from human motion," *Sensors and Actuators A: Physical*, vol. 147, no. 1, pp. 248–253, 2008.

[13] P. D. Mitcheson, T. Sterken, C. He, M. Kiziroglou, E. Yeatman, and R. Puers, "Electrostatic microgenerators," *Measurement and Control*, vol. 41, no. 4, pp. 114–119, 2008.

[14] R. Shukla and A. J. Bell, "Pendexe: A novel energy harvesting concept for low frequency human waistline," *Sensors and Actuators A: Physical*, vol. 222, pp. 39–47, 2015.

[15] J. W. Clark Jr, "The origin of biopotentials," *Medical instrumentation: application and design*, vol. 3, pp. 121–182, 1998.

[16] G. Boyle, "Renewable energy," *Renewable Energy, by Edited by Godfrey Boyle, pp. 456. Oxford University Press, May 2004. ISBN-10: 0199261784. ISBN-13: 9780199261789*, p. 456, 2004.

[17] R. Riemer and A. Shapiro, "Biomechanical energy harvesting from human motion: theory, state of the art, design guidelines, and future directions," *Journal of neuroengineering and rehabilitation*, vol. 8, no. 1, p. 22, 2011.

[18] D. A. Winter, *Biomechanics and motor control of human movement*. John Wiley & Sons, 2009.

[19] F.-R. Fan, Z.-Q. Tian, and Z. L. Wang, "Flexible triboelectric generator," *Nano energy*, vol. 1, no. 2, pp. 328–334, 2012.

[20] B. Lee, "The triboelectric series," *AlphaLab Inc*, 2009.

[21] F. R. Fan, W. Tang, and Z. L. Wang, "Flexible nanogenerators for energy harvesting and self-powered electronics," *Advanced Materials*, vol. 28, no. 22, pp. 4283–4305, 2016.

[22] A. Searle and L. Kirkup, "A direct comparison of wet, dry and insulating bioelectric recording electrodes," *Physiological measurement*, vol. 21, no. 2, p. 271, 2000.

[23] Y. M. Chi, T.-P. Jung, and G. Cauwenberghs, "Dry-contact and noncontact biopotential electrodes: Methodological review," *IEEE reviews in biomedical engineering*, vol. 3, pp. 106–119, 2010.

[24] N. Meziane, J. Webster, M. Attari, and A. Nimunkar, "Dry electrodes for electrocardiography," *Physiological measurement*, vol. 34, no. 9, p. R47, 2013.

[25] T. Le, H.-D. Han, T.-H. Hoang, V. C. Nguyen, and C. K. Nguyen, "A low cost mobile ecg monitoring device using two active dry electrodes," in *Communications and Electronics (ICCE), 2016 IEEE Sixth International Conference on*. IEEE, 2016, pp. 271–276.

[26] M. Catrysse, R. Puers, C. Hertleer, L. Van Langenhove, H. Van Egmond, and D. Matthys, "Towards the integration of textile sensors in a wireless monitoring suit," *Sensors and Actuators A: Physical*, vol. 114, no. 2-3, pp. 302–311, 2004.

[27] S. Choi and Z. Jiang, "A novel wearable sensor device with conductive fabric and pvdf film for monitoring cardiorespiratory signals," *Sensors and Actuators A: Physical*, vol. 128, no. 2, pp. 317–326, 2006.

[28] C.-T. Lin, L.-D. Liao, Y.-H. Liu, I.-J. Wang, B.-S. Lin, J.-Y. Chang *et al.*, "Novel dry polymer foam electrodes for long-term eeg measurement," *IEEE Transactions on Biomedical Engineering*, vol. 58, no. 5, pp. 1200–1207, 2011.

[29] Y.-H. Chen, M. O. de Beeck, L. Vanderheyden, E. Carrette, V. Mihajlović, K. Vanstreels, B. Grundlehner, S. Gadeyne, P. Boon, and C. Van Hoof, "Soft, comfortable polymer dry electrodes for high quality ecg and eeg recording," *Sensors*, vol. 14, no. 12, pp. 23 758–23 780, 2014.

[30] A. Boehm, X. Yu, W. Neu, S. Leonhardt, and D. Teichmann, "A novel 12-lead ecg t-shirt with active electrodes," *Electronics*, vol. 5, no. 4, p. 75, 2016.

[31] D. Pani, A. Dessì, J. F. Saenz-Cogollo, G. Barabino, B. Fraboni, and A. Bonfiglio, "Fully textile, pedot: Pss based electrodes for wearable ecg monitoring systems," *IEEE Transactions on Biomedical Engineering*, vol. 63, no. 3, pp. 540–549, 2016.

[32] M. A. Yokus and J. S. Jur, "Fabric-based wearable dry electrodes for body surface biopotential recording." *IEEE Trans. Biomed. Engineering*, vol. 63, no. 2, pp. 423–430, 2016.

[33] P. S. Das and J.-Y. Park, "A flexible touch sensor based on conductive elastomer for biopotential monitoring applications," *Biomedical Signal Processing and Control*, vol. 33, pp. 72–82, 2017.

[34] X. Guo, W. Pei, Y. Wang, Q. Gong, H. Zhang, X. Xing, Y. Xie, Q. Gui, and H. Chen, "A self-wetting paper electrode for ubiquitous bio-potential monitoring," *IEEE Sensors Journal*, vol. 17, no. 9, pp. 2654–2661, 2017.

[35] X. Xiao, S. Pirbhulal, K. Dong, W. Wu, and X. Mei, "Performance evaluation of plain weave and honeycomb weave electrodes for human ecg monitoring," *Journal of Sensors*, vol. 2017, 2017.

[36] Y.-J. Choi, J.-Y. Lee, and S.-H. Kong, "Driver ecg measuring system with a conductive fabric-based dry electrode," *IEEE Access*, vol. 6, pp. 415–427, 2018.

[37] A. Achilli, A. Bonfiglio, and D. Pani, "Design and characterization of screen-printed textile electrodes for ecg monitoring," *IEEE Sensors Journal*, vol. 18, no. 10, pp. 4097–4107, 2018.

[38] A. J. Golparvar and M. K. Yapici, "Electrooculography by wearable graphene textiles," *IEEE Sensors Journal*, vol. 18, no. 21, pp. 8971–8978, 2018.

[39] Y.-J. Huang, C.-Y. Wu, A. M.-K. Wong, and B.-S. Lin, "Novel active comb-shaped dry electrode for eeg measurement in hairy site," *IEEE Transactions on Biomedical Engineering*, vol. 62, no. 1, pp. 256–263, 2015.

[40] W. Pei, H. Zhang, Y. Wang, X. Guo, X. Xing, Y. Huang, Y. Xie, X. Yang, and H. Chen, "Skin-potential variation insensitive dry electrodes for ecg recording," *IEEE Transactions on Biomedical Engineering*, vol. 64, no. 2, pp. 463–470, 2017.

[41] R. Wang, X. Jiang, W. Wang, and Z. Li, "A microneedle electrode array on flexible substrate for long-term eeg monitoring," *Sensors and Actuators B: Chemical*, vol. 244, pp. 750–758, 2017.

[42] X. Zhou, Q. Li, S. Kilsgaard, F. Moradi, S. L. Kappel, and P. Kidmose, "A wearable ear-eeg recording system based on dry-contact active electrodes," in *VLSI Circuits (VLSI-Circuits), 2016 IEEE Symposium on*. IEEE, 2016, pp. 1–2.

[43] P. Salvo, R. Raedt, E. Carrette, D. Schaubroeck, J. Vanfleteren, and L. Cardon, "A 3d printed dry electrode for ecg/eeg recording," *Sensors and Actuators A: Physical*, vol. 174, pp. 96–102, 2012.

[44] J.-H. Low, M. H. Ang, and C.-H. Yeow, "Customizable soft pneumatic finger actuators for hand orthotic and prosthetic applications," in *Rehabilitation Robotics (ICORR), 2015 IEEE International Conference on*. IEEE, 2015, pp. 380–385.

[45] P. Fiedler, R. Mühle, S. Griebel, P. Pedrosa, C. Fonseca, F. Vaz, F. Zanow, and J. Haueisen, "Contact pressure and flexibility of multipin dry eeg electrodes," *IEEE Transactions on Neural Systems and Rehabilitation Engineering*, 2018.

[46] A. Clippingdale, R. Prance, T. Clark, and C. Watkins, "Ultrahigh impedance capacitively coupled heart imaging array," *Review of scientific instruments*, vol. 65, no. 1, pp. 269–270, 1994.

[47] R. Prance, A. Debray, T. Clark, H. Prance, M. Nock, C. Harland, and A. Clippingdale, "An ultra-low-noise electrical-potential probe for human-body scanning," *Measurement Science and Technology*, vol. 11, no. 3, p. 291, 2000.

[48] C. Harland, T. Clark, and R. Prance, "Remote detection of human electroencephalograms using ultrahigh input impedance electric potential sensors," *Applied Physics Letters*, vol. 81, no. 17, pp. 3284–3286, 2002.

[49] E. Spinelli, M. Haberman, P. García, and F. Guerrero, "A capacitive electrode with fast recovery feature," *Physiological measurement*, vol. 33, no. 8, p. 1277, 2012.

[50] E.-M. Fong and W.-Y. Chung, "A hygroscopic sensor electrode for fast stabilized non-contact ecg signal acquisition," *Sensors*, vol. 15, no. 8, pp. 19 237–19 250, 2015.

[51] Y.-C. Chen, B.-S. Lin, and J.-S. Pan, "Novel noncontact dry electrode with adaptive mechanical design for measuring eeg in a hairy site," *IEEE Transactions on Instrumentation and Measurement*, vol. 64, no. 12, pp. 3361–3368, 2015.

[52] F. R. Parente, M. Santonico, A. Zompanti, M. Benassai, G. Ferri, A. DAmico, and G. Pennazza, "An electronic system for the contactless reading of ecg signals," *Sensors*, vol. 17, no. 11, p. 2474, 2017.

[53] K. Vlach, J. Kijonka, F. Jurek, P. Vavra, and P. Zonca, "Capacitive biopotential electrode with a ceramic dielectric layer," *Sensors and Actuators B: Chemical*, vol. 245, pp. 988–995, 2017.

[54] Y. K. Lim, K. K. Kim, and K. S. Park, "The ecg measurement in the bathtub using the insulated electrodes," in *Engineering in Medicine and Biology Society, 2004. IEMBS'04. 26th Annual International Conference of the IEEE*, vol. 1. IEEE, 2004, pp. 2383–2385.

[55] K. K. Kim, Y. K. Lim, and K. S. Park, "The electrically noncontacting ecg measurement on the toilet seat using the capacitively-coupled insulated electrodes," in *Engineering in Medicine and Biology Society, 2004. IEMBS'04. 26th Annual International Conference of the IEEE*, vol. 1. IEEE, 2004, pp. 2375–2378.

[56] Y. G. Lim, K. K. Kim, and S. Park, "Ecg measurement on a chair without conductive contact," *IEEE Transactions on Biomedical Engineering*, vol. 53, no. 5, pp. 956–959, 2006.

[57] S. Leonhardt and A. Aleksandrowicz, "Non-contact ecg monitoring for automotive application," in *Medical Devices and Biosensors, 2008. ISSS-MDBS 2008. 5th International Summer School and Symposium on.* IEEE, 2008, pp. 183–185.

[58] H. J. Baek, G. S. Chung, K. K. Kim, and K. S. Park, "A smart health monitoring chair for nonintrusive measurement of biological signals," *IEEE transactions on Information Technology in Biomedicine*, vol. 16, no. 1, pp. 150–158, 2012.

[59] J.-M. Kim, J.-H. Hong, M.-C. Cho, E.-J. Cha, and T.-S. Lee, "Wireless biomedical signal monitoring device on wheelchair using noncontact electro-mechanical film sensor," in *Engineering in Medicine and Biology Society, 2007. EMBS 2007. 29th Annual International Conference of the IEEE.* IEEE, 2007, pp. 574–577.

[60] Y. G. Lim, K. K. Kim, and K. S. Park, "Ecg recording on a bed during sleep without direct skin-contact," *IEEE Transactions on Biomedical Engineering*, vol. 54, no. 4, pp. 718–725, 2007.

[61] N. Bu, N. Ueno, and O. Fukuda, "Monitoring of respiration and heartbeat during sleep using a flexible piezoelectric film sensor and empirical mode decomposition," in *Engineering in Medicine and Biology Society, 2007. EMBS 2007. 29th Annual International Conference of the IEEE.* IEEE, 2007, pp. 1362–1366.

[62] Y. M. Chi, S. R. Deiss, and G. Cauwenberghs, "Non-contact low power eeg/ecg electrode for high density wearable biopotential sensor networks," in *Wearable and Implantable Body Sensor Networks, 2009. BSN 2009. Sixth International Workshop on.* IEEE, 2009, pp. 246–250.

[63] Y. M. Chi and G. Cauwenberghs, "Wireless non-contact eeg/ecg electrodes for body sensor networks," in *2010 International Conference on Body Sensor Networks.* IEEE, 2010, pp. 297–301.

[64] Y. M. Chi, P. Ng, E. Kang, J. Kang, J. Fang, and G. Cauwenberghs, "Wireless non-contact cardiac and neural monitoring," in *Wireless Health 2010.* ACM, 2010, pp. 15–23.

[65] Y. Sun and X. B. Yu, "Capacitive biopotential measurement for electrophysiological signal acquisition: A review," *IEEE Sensors Journal*, vol. 16, no. 9, pp. 2832–2853, 2016.

[66] T. Matsuda and M. Makikawa, "Ecg monitoring of a car driver using capacitively-coupled electrodes," in *2008 30th Annual International Conference of the IEEE Engineering in Medicine and Biology Society*. IEEE, 2008, pp. 1315–1318.

[67] E. Michail, A. Kokonozi, I. Chouvarda, and N. Maglaveras, "Eeg and hrv markers of sleepiness and loss of control during car driving," in *Engineering in Medicine and Biology Society, 2008. EMBS 2008. 30th Annual International Conference of the IEEE*. IEEE, 2008, pp. 2566–2569.

[68] T. Wartzek, B. Eilebrecht, J. Lem, H.-J. Lindner, S. Leonhardt, and M. Walter, "Ecg on the road: Robust and unobtrusive estimation of heart rate," *IEEE Transactions on biomedical engineering*, vol. 58, no. 11, pp. 3112–3120, 2011.

[69] Y. Sun and X. B. Yu, "An innovative nonintrusive driver assistance system for vital signal monitoring." *IEEE J. Biomedical and Health Informatics*, vol. 18, no. 6, pp. 1932–1939, 2014.

[70] Z. Wan, Y. Tan, and C. Yuen, "Review on energy harvesting and energy management for sustainable wireless sensor networks," in *Communication Technology (ICCT), 2011 IEEE 13th International Conference on*. IEEE, 2011, pp. 362–367.

[71] G. D. Szarka, B. H. Stark, and S. G. Burrow, "Review of power conditioning for kinetic energy harvesting systems," *IEEE transactions on power electronics*, vol. 27, no. 2, pp. 803–815, 2012.

[72] F. Invernizzi, S. Dulio, M. Patrini, G. Guizzetti, and P. Mustarelli, "Energy harvesting from human motion: materials and techniques," *Chemical Society Reviews*, vol. 45, no. 20, pp. 5455–5473, oct 2016. [Online]. Available: http://xlink.rsc.org/?DOI=C5CS00812C

[73] R. J. Vullers, R. Van Schaijk, H. J. Visser, J. Penders, and C. Van Hoof, "Energy harvesting for autonomous wireless sensor networks," *IEEE Solid-State Circuits Magazine*, vol. 2, no. 2, pp. 29–38, 2010.

[74] L. Xie and M. Cai, "Human motion: Sustainable power for wearable electronics," *IEEE Pervasive Computing*, vol. 13, no. 4, pp. 42–49, 2014.

[75] A. Harb, "Energy harvesting: State-of-the-art," *Renewable Energy*, vol. 36, no. 10, pp. 2641–2654, 2011.

[76] K. A. Cook-Chennault, N. Thambi, and A. M. Sastry, "Powering mems portable devicesa review of non-regenerative and regenerative power supply systems with special emphasis on piezoelectric energy harvesting systems," *Smart materials and structures*, vol. 17, no. 4, p. 043001, 2008.

[77] G. Poulin, E. Sarraute, and F. Costa, "Generation of electrical energy for portable devices Comparative study of an electromagnetic and a piezoelectric system," *Sensors and Actuators A*, vol. 116, pp. 461–471, 2004. [Online]. Available: https://ac.els-cdn.com/S0924424704003516/1-s2.0-S0924424704003516-main.pdf?{_}tid=f3b27511-0f13-4fb6-bec1-ef02167d8db1{&}acdnat=1550380703{_}5e720469491687995386c080f8562d62

[78] H. A. Sodano, D. J. Inman, and G. Park, "A review of power harvesting from vibration using piezoelectric materials," *Shock and Vibration Digest*, vol. 36, no. 3, pp. 197–206, 2004.

[79] S. R. Anton and H. A. Sodano, "A review of power harvesting using piezoelectric materials (2003–2006)," *Smart materials and Structures*, vol. 16, no. 3, p. R1, 2007.

[80] R. Harne and K. Wang, "A review of the recent research on vibration energy harvesting via bistable systems," *Smart materials and structures*, vol. 22, no. 2, p. 023001, 2013.

[81] G. Park, T. Rosing, M. D. Todd, C. R. Farrar, and W. Hodgkiss, "Energy harvesting for structural health monitoring sensor networks," *Journal of Infrastructure Systems*, vol. 14, no. 1, pp. 64–79, 2008.

[82] J. Matiko, N. Grabham, S. Beeby, and M. Tudor, "Review of the application of energy harvesting in buildings," *Measurement Science and Technology*, vol. 25, no. 1, p. 012002, 2013.

[83] N. Panwar, S. Kaushik, and S. Kothari, "Role of renewable energy sources in environmental protection: a review," *Renewable and Sustainable Energy Reviews*, vol. 15, no. 3, pp. 1513–1524, 2011.

[84] M. Ha, J. Park, Y. Lee, and H. Ko, "Triboelectric generators and sensors for self-powered wearable electronics," *Acs Nano*, vol. 9, no. 4, pp. 3421–3427, 2015.

[85] A. Hajati and S.-G. Kim, "Ultra-wide bandwidth piezoelectric energy harvesting," *Applied Physics Letters*, vol. 99, no. 8, p. 083105, 2011.

[86] M. F. Daqaq, "Transduction of a bistable inductive generator driven by white and exponentially correlated gaussian noise," *Journal of Sound and Vibration*, vol. 330, no. 11, pp. 2554–2564, 2011.

[87] J. Cao, S. Zhou, W. Wang, and J. Lin, "Influence of potential well depth on nonlinear tristable energy harvesting," *Applied Physics Letters*, vol. 106, no. 17, p. 173903, 2015.

[88] M. Gorlatova, J. Sarik, G. Grebla, M. Cong, I. Kymissis, and G. Zussman, "Movers and shakers: Kinetic energy harvesting for the internet of things," *IEEE Journal on Selected Areas in Communications*, vol. 33, no. 8, pp. 1624–1639, 2015.

[89] M. Zhou, M. S. H. Al-Furjan, J. Zou, and W. Liu, "A review on heat and mechanical energy harvesting from human–principles, prototypes and perspectives," *Renewable and Sustainable Energy Reviews*, vol. 82, pp. 3582–3609, 2018.

[90] P. Niu, P. Chapman, R. Riemer, and X. Zhang, "Evaluation of motions and actuation methods for biomechanical energy harvesting," in *Power Electronics Specialists Conference, 2004. PESC 04. 2004 IEEE 35th Annual*, vol. 3. IEEE, 2004, pp. 2100–2106.

[91] T. Starner, "Human-powered wearable computing," *IBM systems Journal*, vol. 35, no. 3/4, pp. 618–629, 1996.

[92] L. C. Rome, L. Flynn, E. M. Goldman, and T. D. Yoo, "Generating electricity while walking with loads," *Science*, vol. 309, no. 5741, pp. 1725–1728, 2005.

[93] J. M. Donelan, Q. Li, V. Naing, J. Hoffer, D. Weber, and A. D. Kuo, "Biomechanical energy harvesting: generating electricity during walking with minimal user effort," *Science*, vol. 319, no. 5864, pp. 807–810, 2008.

[94] P. Vasandani, B. Gattu, J. Wu, Z.-H. Mao, W. Jia, and M. Sun, "Triboelectric nanogenerator using microdome-patterned pdms as a wearable respiratory energy harvester," *Advanced Materials Technologies*, vol. 2, no. 6, p. 1700014, 2017.

[95] F. Qian, T.-B. Xu, and L. Zuo, "Design, optimization, modeling and testing of a piezoelectric footwear energy harvester," *Energy Conversion and Management*, vol. 171, pp. 1352–1364, 2018.

[96] S. Niu, X. Wang, F. Yi, Y. S. Zhou, and Z. L. Wang, "A universal self-charging system driven by random biomechanical energy for sustainable operation of mobile electronics," *Nature communications*, vol. 6, p. 8975, 2015.

[97] X. Pu, L. Li, H. Song, C. Du, Z. Zhao, C. Jiang, G. Cao, W. Hu, and Z. L. Wang, "A self-charging power unit by integration of a textile triboelectric nanogenerator and a flexible lithium-ion battery for wearable electronics," *Advanced Materials*, vol. 27, no. 15, pp. 2472–2478, 2015.

[98] X. Pu, M. Liu, X. Chen, J. Sun, C. Du, Y. Zhang, J. Zhai, W. Hu, and Z. L. Wang, "Ultrastretchable, transparent triboelectric nanogenerator as electronic skin for biomechanical energy harvesting and tactile sensing," *Science advances*, vol. 3, no. 5, p. e1700015, 2017.

[99] H. Ryu, J. H. Lee, U. Khan, S. S. Kwak, R. Hinchet, and S.-W. Kim, "Sustainable direct current powering a triboelectric nanogenerator via a novel asymmetrical design," *Energy & Environmental Science*, 2018.

[100] F. Chen, Y. Wu, Z. Ding, X. Xia, S. Li, H. Zheng, C. Diao, G. Yue, and Y. Zi, "A novel triboelectric nanogenerator based on electrospun polyvinylidene fluoride nanofibers for effective acoustic energy harvesting and self-powered multifunctional sensing," *Nano energy*, vol. 56, pp. 241–251, 2019.

[101] D. Bao, L. Luo, Z. Zhang, and T. Ren, "A power management circuit with 50% efficiency and large load capacity for triboelectric nanogenerator," *Journal of Semiconductors*, vol. 38, no. 9, p. 095001, 2017.

[102] F. Xi, Y. Pang, W. Li, T. Jiang, L. Zhang, T. Guo, G. Liu, C. Zhang, and Z. L. Wang, "Universal power management strategy for triboelectric nanogenerator," *Nano Energy*, vol. 37, pp. 168–176, 2017.

[103] X. Cheng, L. Miao, Y. Song, Z. Su, H. Chen, X. Chen, J. Zhang, and H. Zhang, "High efficiency power management and charge boosting strategy for a triboelectric nanogenerator," *Nano Energy*, vol. 38, pp. 438–446, 2017.

[104] I. Park, J. Maeng, D. Lim, M. Shim, J. Jeong, and C. Kim, "A 4.5-to-16μw integrated triboelectric energy-harvesting system based on high-voltage dual-input buck converter with mppt and 70v maximum input voltage," in *Solid-State Circuits Conference-(ISSCC), 2018 IEEE International*. IEEE, 2018, pp. 146–148.

[105] H. Qin, G. Cheng, Y. Zi, G. Gu, B. Zhang, W. Shang, F. Yang, J. Yang, Z. Du, and Z. L. Wang, "High energy storage efficiency triboelectric nanogenerators with unidirectional switches and passive power management circuits," *Advanced Functional Materials*, vol. 28, no. 51, p. 1805216, 2018.

[106] P. Vasandani, B. Gattu, Z.-H. Mao, W. Jia, and M. Sun, "Using a synchronous switch to enhance output performance of triboelectric nanogenerators," *Nano Energy*, vol. 43, pp. 210–218, 2018.

[107] R. Fensli, E. Gunnarson, and T. Gundersen, "A wearable ecg-recording system for continuous arrhythmia monitoring in a wireless tele-home-care situation," in *Computer-Based Medical Systems, 2005. Proceedings. 18th IEEE Symposium on.* IEEE, 2005, pp. 407–412.

[108] C. Park, P. H. Chou, Y. Bai, R. Matthews, and A. Hibbs, "An ultra-wearable, wireless, low power ecg monitoring system," in *Biomedical Circuits and Systems Conference, 2006. BioCAS 2006. IEEE.* IEEE, 2006, pp. 241–244.

[109] C.-T. Lin, K.-C. Chang, C.-L. Lin, C.-C. Chiang, S.-W. Lu, S.-S. Chang, B.-S. Lin, H.-Y. Liang, R.-J. Chen, Y.-T. Lee *et al.*, "An intelligent telecardiology system using a wearable and wireless ecg to detect atrial fibrillation," *IEEE Transactions on Information Technology in Biomedicine*, vol. 14, no. 3, pp. 726–733, 2010.

[110] J. Penders, J. van de Molengraft, M. Altini, F. Yazicioglu, and C. Van Hoof, "A low-power wireless ecg necklace for reliable cardiac activity monitoring on-the-move," in *Proceedings of the International Conference of the IEEE Engineering in Medicine and Biology Society*, 2011.

[111] F. Massé, M. V. Bussel, A. Serteyn, J. Arends, and J. Penders, "Miniaturized wireless ecg monitor for real-time detection of epileptic seizures," *ACM Transactions on Embedded Computing Systems (TECS)*, vol. 12, no. 4, p. 102, 2013.

[112] Ž. Lučev, I. Krois, M. Cifrek, and P. Girao, "A multichannel wireless emg measurement system based on intrabody communication," in *XIX IMEKO World Congress, Fundamental and Applied Metrology*, 2009, pp. 1711–1715.

[113] H. Kobayashi, "Intelligent wireless emg/ecg electrode employing zigbee technology," in *SICE Annual Conference (SICE), 2011 Proceedings of.* IEEE, 2011, pp. 2856–2861.

[114] J. Xu, S. Mitra, A. Matsumoto, S. Patki, C. Van Hoof, K. A. Makinwa, and R. F. Yazicioglu, "A wearable 8-channel active-electrode eeg/eti acquisition system for body area networks," *IEEE Journal of Solid-State Circuits*, vol. 49, no. 9, pp. 2005–2016, 2014.

[115] J. Xu, B. Büsze, C. Van Hoof, K. A. Makinwa, and R. F. Yazicioglu, "A 15-channel digital active electrode system for multi-parameter biopotential measurement," *IEEE Journal of Solid-State Circuits*, vol. 50, no. 9, pp. 2090–2100, 2015.

[116] G. Li, B.-L. Lee, and W.-Y. Chung, "Smartwatch-based wearable eeg system for driver drowsiness detection," *IEEE Sensors Journal*, vol. 15, no. 12, pp. 7169–7180, 2015.

[117] S. Imani, A. J. Bandodkar, A. V. Mohan, R. Kumar, S. Yu, J. Wang, and P. P. Mercier, "A wearable chemical–electrophysiological hybrid biosensing system for real-time health and fitness monitoring," *Nature communications*, vol. 7, p. 11650, 2016.

[118] V. P. Rachim and W.-Y. Chung, "Wearable noncontact armband for mobile ecg monitoring system," *IEEE transactions on biomedical circuits and systems*, vol. 10, no. 6, pp. 1112–1118, 2016.

[119] F. Sun, C. Yi, W. Li, and Y. Li, "A wearable h-shirt for exercise ecg monitoring and individual lactate threshold computing," *Computers in Industry*, vol. 92, pp. 1–11, 2017.

[120] M. S. Mahmud, H. Wang, A. Esfar-E-Alam, and H. Fang, "A wireless health monitoring system using mobile phone accessories," *IEEE Internet of Things Journal*, vol. 4, no. 6, pp. 2009–2018, 2017.

[121] S. Liu, X. Liu, Y. Jiang, X. Wang, P. Huang, H. Wang, M. Zhu, J. Tan, P. Li, C. Lin *et al.*, "Flexible non-contact electrodes for bioelectrical signal monitoring," in *2018 40th Annual International Conference of the IEEE Engineering in Medicine and Biology Society (EMBC)*. IEEE, 2018, pp. 4305–4308.

[122] K. C. Tseng, B.-S. Lin, L.-D. Liao, Y.-T. Wang, Y.-L. Wang *et al.*, "Development of a wearable mobile electrocardiogram monitoring system by using novel dry foam electrodes." *IEEE systems Journal*, vol. 8, no. 3, pp. 900–906, 2014.

[123] J. Wang, T. Fujiwara, T. Kato, D. Anzai *et al.*, "Wearable ecg based on impulse-radio-type human body communication." *IEEE Trans. Biomed. Engineering*, vol. 63, no. 9, pp. 1887–1894, 2016.

[124] E. Spanò, S. Di Pascoli, and G. Iannaccone, "Low-power wearable ecg monitoring system for multiple-patient remote monitoring," *IEEE Sensors Journal*, vol. 16, no. 13, pp. 5452–5462, 2016.

[125] Y. Ye-Lin, J. M. Bueno-Barrachina, G. Prats-Boluda, R. R. de Sanabria, and J. Garcia-Casado, "Wireless sensor node for non-invasive high precision electrocardiographic signal acquisition based on a multi-ring electrode," *Measurement*, vol. 97, pp. 195–202, 2017.

[126] H. Li, X. Chen, L. Cao, C. Zhang, C. Tang, E. Li, X. Feng, and H. Liang, "Textile-based ecg acquisition system with capacitively coupled electrodes," *Transactions of the Institute of Measurement and Control*, vol. 39, no. 2, pp. 141–148, 2017.

[127] K. Lin, X. Wang, X. Zhang, B. Wang, J. Huang, and F. Huang, "An fpc based flexible dry electrode with stacked double-micro-domes array for wearable biopotential recording system," *Microsystem Technologies*, vol. 23, no. 5, pp. 1443–1451, 2017.

[128] M. Marouf, G. Vukomanovic, L. Saranovac, and M. Bozic, "Multi-purpose ecg telemetry system," *Biomedical engineering online*, vol. 16, no. 1, p. 80, 2017.

[129] F. N. Guerrero and E. M. Spinelli, "A two-wired ultra-high input impedance active electrode," *IEEE transactions on biomedical circuits and systems*, vol. 12, no. 2, pp. 437–445, 2018.

[130] K.-p. Gao, H.-j. Yang, X.-l. Wang, B. Yang, and J.-q. Liu, "Sensors and Actuators A : Physical Soft pin-shaped dry electrode with bristles for EEG signal measurements," *Sensors & Actuators: A. Physical*, vol. 283, pp. 348–361, 2018. [Online]. Available: https://doi.org/10.1016/j.sna.2018.09.045

[131] S. He, X. Li, I. Batkin, H. R. Dajani, S. Member, and M. Bolic, "Detecting Cardiac Activity by Capacitive Electrodes from a Single Point on the Wrist," pp. 3809–3812, 2018.

[132] A. A. Uvarov, I. A. Lezhnina, K. V. Overchuk, A. S. Starchak, S. D. Akhmedov, and I. A. Larioshina, "Study of the Properties of Plessey's Electrocardiographic Capacitive Electrodes for Portable Systems," *Journal of Physics: Conference Series*, vol. 671, no. 1, p. 012032, jan 2016. [Online]. Available: http://stacks.iop.org/1742-6596/671/i=1/a=012032?key=crossref.97603ebabc69aa6a15166f4deaef39c0

[133] X. Li, H. Huang, and Y. Sun, "TriboWalk: Triboelectric dual functional wireless system for gait monitoring and energy harvesting," *Proceedings of the Annual International Conference of the IEEE Engineering in Medicine and Biology Society, EMBS*, vol. 2016-October, pp. 4796–4799, 2016.

[134] Simiao Niu, Ying Liu, Yu Sheng Zhou, Sihong Wang, Long Lin, and Zhong Lin Wang, "Optimization of Triboelectric Nanogenerator Charging Systems for Efficient Energy Harvesting and Storage," *IEEE Transactions on Electron Devices*, vol. 62, no. 2, pp. 641–647, feb 2015. [Online]. Available: http://ieeexplore.ieee.org/document/6994827/

[135] G. Zhu, Y. S. Zhou, P. Bai, X. S. Meng, Q. Jing, J. Chen, and Z. L. Wang, "A Shape-Adaptive Thin-Film-Based Approach for 50% High-Efficiency Energy Generation Through Micro-Grating Sliding Electrification," *Advanced Materials*, vol. 26, no. 23, pp. 3788–3796, jun 2014. [Online]. Available: http://doi.wiley.com/10.1002/adma.201400021

[136] Y. Zi, L. Lin, J. Wang, S. Wang, J. Chen, X. Fan, P.-K. Yang, F. Yi, and Z. L. Wang, "Triboelectric-Pyroelectric-Piezoelectric Hybrid Cell for High-Efficiency Energy-Harvesting and Self-Powered Sensing," *Advanced Materials*, vol. 27, no. 14, pp. 2340–2347, apr 2015. [Online]. Available: http://doi.wiley.com/10.1002/adma.201500121

[137] Y. Zi, S. Niu, J. Wang, Z. Wen, W. Tang, and Z. L. Wang, "Standards and figure-of-merits for quantifying the performance of triboelectric nanogenerators," *Nature Communications*, vol. 6, no. 1, p. 8376, dec 2015. [Online]. Available: http://www.nature.com/articles/ncomms9376

[138] S. P. Beeby, M. J. Tudor, and N. White, "Energy harvesting vibration sources for microsystems applications," *Measurement science and technology*, vol. 17, no. 12, p. R175, 2006.

[139] L. Mateu and F. Moll, "Appropriate charge control of the storage capacitor in a piezoelectric energy harvesting device for discontinuous load operation," *Sensors and Actuators A: Physical*, vol. 132, no. 1, pp. 302–310, nov 2006. [Online]. Available: https://www.sciencedirect.com/science/article/pii/S0924424706004596

[140] H. Wang, J.-D. Park, and Z. J. Ren, "Practical Energy Harvesting for Microbial Fuel Cells: A Review," *Environmental Science & Technology*, vol. 49, no. 6, pp. 3267–3277, mar 2015. [Online]. Available: http://pubs.acs.org/doi/10.1021/es5047765

[141] P. Pillatsch, E. M. Yeatman, and A. S. Holmes, "Real World Testing Of A Piezoelectric Rotational Energy Harvester For Human Motion," *Journal of Physics: Conference Series*, vol. 476, no. 1, p. 012010, dec 2013. [Online]. Available: http://stacks.iop.org/1742-6596/476/i=1/a=012010?key=crossref.323d8af74744f84a3238a3749bdba6b5

[142] X. Pu, L. Li, H. Song, C. Du, Z. Zhao, C. Jiang, G. Cao, W. Hu, and Z. L. Wang, "A self-charging power unit by integration of a textile triboelectric nanogenerator and a flexible lithium-ion battery for wearable electronics," *Advanced Materials*, vol. 27, no. 15, pp. 2472–2478, 2015.

[143] X. Li and Y. Sun, "WearETE: A scalable wearable E-textile triboelectric energy harvesting system for human motion scavenging," *Sensors (Switzerland)*, vol. 17, no. 11, 2017.

[144] C. Dagdeviren, Z. Li, and Z. L. Wang, "Energy Harvesting from the Animal/Human Body for Self-Powered Electronics," *Annual Review of Biomedical Engineering*, vol. 19, no. 1, pp. 85–108, 2017. [Online]. Available: http://www.annualreviews.org/doi/10.1146/annurev-bioeng-071516-044517

[145] D. Guyomar, A. Badel, E. Lefeuvre, and C. Richard, "Materials and Conversion Improvement by Nonlinear Processing," *Energy*, vol. 52, no. 4, pp. 584–595, 2005.

[146] L. Garbuio, M. Lallart, D. Guyomar, C. Richard, and D. Audigier, "Mechanical energy harvester with ultralow threshold rectification based on SSHI nonlinear technique," *IEEE Transactions on Industrial Electronics*, vol. 56, no. 4, pp. 1048–1056, 2009.

[147] J. Liang and W. H. Liao, "Improved design and analysis of self-powered synchronized switch interface circuit for piezoelectric energy harvesting systems," *IEEE Transactions on Industrial Electronics*, vol. 59, no. 4, pp. 1950–1960, 2012.

[148] S. Niu, S. Wang, L. Lin, Y. Liu, Y. S. Zhou, Y. Hu, and Z. L. Wang, "Theoretical study of contact-mode triboelectric nanogenerators as an effective power source," *Energy and Environmental Science*, vol. 6, no. 12, pp. 3576–3583, 2013.

[149] S. Niu and Z. L. Wang, "Theoretical systems of triboelectric nanogenerators," *Nano Energy*, vol. 14, pp. 161–192, 2014. [Online]. Available: http://dx.doi.org/10.1016/j.nanoen.2014.11.034

[150] P. Vasandani, Z. H. Mao, W. Jia, and M. Sun, "Relationship between triboelectric charge and contact force for two triboelectric layers," *Journal of Electrostatics*, vol. 90, no. October, pp. 147–152, 2017. [Online]. Available: https://doi.org/10.1016/j.elstat.2017.11.001

[151] H. Huang, X. Li, S. Liu, S. Hu, and Y. Sun, "TriboMotion: A Self-Powered Triboelectric Motion Sensor in Wearable Internet of Things for Human Activity Recognition and Energy Harvesting," *IEEE Internet of Things Journal*, vol. 5, no. 6, pp. 4441–4453, 2018.

[152] J. R. Liang and W. H. Liao, "Piezoelectric energy harvesting and dissipation on structural damping," *Journal of Intelligent Material Systems and Structures*, vol. 20, no. 5, pp. 515–527, 2009.

[153] D. Guyomar and M. Lallart, "Recent progress in piezoelectric conversion and energy harvesting using nonlinear electronic interfaces and issues in small scale implementation," *Micromachines*, vol. 2, no. 2, pp. 274–294, 2011.

[154] T. Hehn, F. Hagedorn, D. Maurath, D. Marinkovic, I. Kuehne, A. Frey, and Y. Manoli, "A fully autonomous integrated interface circuit for piezoelectric harvesters," *IEEE Journal of Solid-State Circuits*, vol. 47, no. 9, pp. 2185–2198, 2012.

[155] E. E. Aktakka and K. Najafi, "A micro inertial energy harvesting platform with self-supplied power management circuit for autonomous wireless sensor nodes," *IEEE Journal of Solid-State Circuits*, vol. 49, no. 9, pp. 2017–2029, 2014.

[156] P. Gasnier, J. Willemin, S. Boisseau, G. Despesse, C. Condemine, G. Gouvernet, and J. J. Chaillout, "An autonomous piezoelectric energy harvesting IC based on a synchronous multi-shot technique," *IEEE Journal of Solid-State Circuits*, vol. 49, no. 7, pp. 1561–1570, 2014.

[157] S. Lu and F. Boussaid, "A highly efficient P-SSHI rectifier for piezoelectric energy harvesting," *IEEE Transactions on Power Electronics*, vol. 30, no. 10, pp. 5364–5369, 2015.

[158] M. Dini, A. Romani, M. Filippi, and M. Tartagni, "A Nanopower Synchronous Charge Extractor IC for Low-Voltage Piezoelectric Energy Harvesting with Residual Charge Inversion," *IEEE Transactions on Power Electronics*, vol. 31, no. 2, pp. 1263–1274, 2016.

[159] A. M. Eltamaly and K. E. Addoweesh, "A Novel Self-Power SSHI Circuit for Piezoelectric Energy Harvester," *IEEE Transactions on Power Electronics*, vol. 32, no. 10, pp. 7663–7673, 2017.

[160] L. Wu, X. D. Do, S. G. Lee, and D. S. Ha, "A Self-Powered and Optimal SSHI Circuit Integrated with an Active Rectifier for Piezoelectric Energy Harvesting," *IEEE Transactions on Circuits and Systems I: Regular Papers*, vol. 64, no. 3, pp. 537–549, 2017.

[161] I. Khemili and L. Romdhane, "Dynamic analysis of a flexible slider-crank mechanism with clearance," *European Journal of Mechanics, A/Solids*, vol. 27, no. 5, pp. 882–898, 2008.

[162] H. S. Kim, J.-H. Kim, and J. Kim, "A review of piezoelectric energy harvesting based on vibration," *International journal of precision engineering and manufacturing*, vol. 12, no. 6, pp. 1129–1141, 2011.

[163] V. Nguyen and R. Yang, "Effect of humidity and pressure on the triboelectric nanogenerator," *Nano Energy*, vol. 2, no. 5, pp. 604–608, 2013. [Online]. Available: http://dx.doi.org/10.1016/j.nanoen.2013.07.012

[164] H. Huang, S. Hu, and Y. Sun, "Energy-efficient ecg compression in wearable body sensor network by leveraging empirical mode decomposition," in *Biomedical & Health Informatics (BHI), 2018 IEEE EMBS International Conference on.* IEEE, 2018, pp. 149–152.

[165] G. Moody and R. Mark, "The impact of the MIT-BIH Arrhythmia Database," *IEEE Engineering in Medicine and Biology Magazine*, vol. 20, no. 3, pp. 45–50, 2001. [Online]. Available: http://ieeexplore.ieee.org/document/932724/

[166] M. Hooshmand, D. Zordan, D. Del Testa, E. Grisan, and M. Rossi, "Boosting the Battery Life of Wearables for Health Monitoring Through the Compression of Biosignals," *IEEE Internet of Things Journal*, vol. 4, no. 5, pp. 1647–1662, oct 2017. [Online]. Available: http://ieeexplore.ieee.org/document/7888991/

[167] J. Ma, T. ZHANG, and M. DONG, "A Novel ECG Data Compression Method Using Adaptive Fourier Decomposition with Security Guarantee in e-Health Applications," *IEEE Journal of Biomedical and Health Informatics*, pp. 1–1, 2014. [Online]. Available: http://ieeexplore.ieee.org/document/6897915/

[168] European Alliance for Innovation, Ethniko Metsovio Polytechneio (Greece), IEEE Antennas and Propagation Society, IEEE Engineering in Medicine and Biology Society, S.-I. Institute for Computer Sciences, and Institute of Electrical and Electronics Engineers., *Proceedings of the 2014 4th International Conference on Wireless Mobile Communication and Healthcare - "Transforming healthcare through innovations in mobile and wireless technologies" (MOBIHEALTH) : MOBIHEALTH 2014 : Athens, Greece, November 03-05, 2014.* [Online]. Available: https://ieeexplore.ieee.org/abstract/document/7015915

[169] M. Collotta, G. Pau, T. Talty, and O. K. Tonguz, "Bluetooth 5: A Concrete Step Forward toward the IoT," *IEEE Communications Magazine*, vol. 56, no. 7, pp. 125–131, 2018.

[170] S. Bitzer and P. Van Der Smagt, "Learning emg control of a robotic hand: towards active prostheses," in *Robotics and Automation, 2006. ICRA 2006. Proceedings 2006 IEEE International Conference on.* IEEE, 2006, pp. 2819–2823.

[171] M. A. Lebedev and M. A. Nicolelis, "Brain–machine interfaces: past, present and future," *TRENDS in Neurosciences*, vol. 29, no. 9, pp. 536–546, 2006.

[172] A. Aleksandrowicz and S. Leonhardt, "Wireless and non-contact ecg measurement system–the aachen smartchair," *Acta Polytechnica*, vol. 47, no. 4-5, 2007.

[173] M. J. Adams, B. J. Briscoe, and S. A. Johnson, "Friction and lubrication of human skin," *Tribology letters*, vol. 26, no. 3, pp. 239–253, 2007.

[174] J. P. Abenstein and W. J. Tompkins, "A New Data-Reduction Algorithm for Real-Time ECG Analysis," *IEEE Transactions on Biomedical Engineering*, vol. BME-29, no. 1, pp. 43–48, jan 1982. [Online]. Available: http://ieeexplore.ieee.org/document/4121312/